FEMTOSECOND LASER MICROMACHINING OF ADVANCED MATERIALS

by

QIUMEI BIAN

B.S., North China Institute of Technology, 1993
M.S. , North University of China, 1997

AN ABSTRACT OF A DISSERTATION

submitted in partial fulfillment of the requirements for the degree

DOCTOR OF PHILOSOPHY

Department of Industrial and Manufacturing Systems Engineering
College of Engineering

KANSAS STATE UNIVERSITY
Manhattan, Kansas

2013

Abstract

Femtosecond (fs) laser ablation possesses unique characteristics for micromachining, notably non-thermal interaction with materials, high peak intensity, precision and flexibility. In this dissertation, the potential of fs laser ablation for machining polyurea aerogel and scribing thin film solar cell interconnection grooves is studied. In a preliminary background discussion, some key literature regarding the basic physics and mechanisms that govern ultrafast laser pulse interaction with materials and laser micromachining are summarized.

First, the fs laser pulses are used to micromachine polyurea aerogel. The experimental results demonstrate that high quality machining surface can be obtained by tuning the laser fluence and beam scanning speed, which provides insights for micromachining polymers with porous structures. Second, a new fs laser micro-drilling technique is developed to drill micro-holes in stainless steel, in which a hollow core fiber is employed to transmit laser pulses to the target position. The coupling efficiency between the laser and the fiber is investigated and found to be strongly related to pulse energy and pulse duration. Third, the fs laser with various energy, pulse durations, and scanning speeds has been utilized to pattern Indium Tin Oxide (ITO) glass for thin film solar cells. The groove width decreases with increasing pulse duration due to the shorter the pulse duration the more effective of the energy used to material removal. In order to fully remove ITO without damaging the glass, the beam scanning speed need to precisely be controlled. Fourth, fs laser has been utilized to scribe Molybdenum thin film on Polyimide (PI) flexible substrate for Copper Indium Gallium Selenide (CIGS) thin film solar cells. The experimental parameters and results including ablation threshold, single- and multiple-pulse ablation shapes and ablation efficiency were discussed in details.

In order to utilize the advantages of the fs lasers, the fabrication process has to be optimized for thin film patterning and structuring applications concerning both efficiency and quality. A predictive 3 dimensional (3D) Two Temperature Model (TTM) was proposed to predict ablation characteristics and help to understand the fs laser metal ablation mechanisms. 3D temperature field evolution for both electrons and lattice were demonstrated. The ablation model provides an insight to the physical processes occurring during fs laser excitation of metals. Desired processing fluence and process speed regime can be predicted by calculating the ablation threshold, ablation rate and ablation crater geometry using the developed model.

FEMTOSECOND LASER MICROMACHINING OF ADVANCED MATERIALS

by

QIUMEI BIAN

B.S., North China Institute of Technology, 1993
M.S., North University of China, 1997

A DISSERTATION

submitted in partial fulfillment of the requirements for the degree

DOCTOR OF PHILOSOPHY

Department of Industrial and Manufacturing Systems Engineering
College of Engineering

KANSAS STATE UNIVERSITY
Manhattan, Kansas

2013

Approved by:

Major Professor
Dr. Shuting Lei

Copyright

QIUMEI BIAN

2013

Abstract

Femtosecond (fs) laser ablation possesses unique characteristics for micromachining, notably non-thermal interaction with materials, high peak intensity, precision and flexibility. In this dissertation, the potential of fs laser ablation for machining polyurea aerogel and scribing thin film solar cell interconnection grooves is studied. In a preliminary background discussion, some key literature regarding the basic physics and mechanisms that govern ultrafast laser pulse interaction with materials and laser micromachining are summarized.

First, the fs laser pulses are used to micromachine polyurea aerogel. The experimental results demonstrate that high quality machining surface can be obtained by tuning the laser fluence and beam scanning speed, which provides insights for micromachining polymers with porous structures. Second, a new fs laser micro-drilling technique is developed to drill micro-holes in stainless steel, in which a hollow core fiber is employed to transmit laser pulses to the target position. The coupling efficiency between the laser and the fiber is investigated and found to be strongly related to pulse energy and pulse duration. Third, the fs laser with various energy, pulse durations, and scanning speeds has been utilized to pattern Indium Tin Oxide (ITO) glass for thin film solar cells. The groove width decreases with increasing pulse duration due to the shorter the pulse duration the more effective of the energy used to material removal. In order to fully remove ITO without damaging the glass, the beam scanning speed need to precisely be controlled. Fourth, fs laser has been utilized to scribe Mo thin film on Polyimide (PI) flexible substrate for Copper Indium Gallium Selenide (CIGS) thin film solar cells. The experimental parameters and results including ablation threshold, single- and multiple-pulse ablation shapes and ablation efficiency were discussed in details.

In order to utilize the advantages of the fs lasers, the fabrication process has to be optimized for thin film patterning and structuring applications concerning both efficiency and quality. A predictive 3 dimensional (3D) Two Temperature Model (TTM) was proposed to predict ablation characteristics and help to understand the fs laser metal ablation mechanisms. 3D temperature field evolution for both electrons and lattice were demonstrated. The ablation model provides an insight to the physical processes occurring during fs laser excitation of metals. Desired processing fluence and process speed regime can be predicted by calculating the ablation threshold, ablation rate and ablation crater geometry using the developed model. It also can be applied to fs laser ablation of other metals and semiconductors.

Table of Contents

List of Figures

List of Tables

Acknowledgements

First of all, I would like to sincerely thank my advisor Professor Shuting Lei for giving me the opportunity to be his student. I'm grateful for his supporting and guidance during my graduate studies at K-state. He taught and encouraged me to how to question thought and express ideas through research process. His brilliant ideas, patience and expertise help me overcome setbacks and stay focused on my graduate study.

Special thanks also go to Professor Zenghu Chang for giving me the opportunity to do research in his group and for his constant support and guidance. He provided lots of valuable suggestions on my research. His expertise and knowledge in optical and laser field were paramount in providing a well-rounded experience consistent my long-term career goals.

I would like to thank to Professor Shing I. Chang and Professor Jun Li for their useful suggestions and kind advices on my research. Their advices about research approaches will definitely benefit my academic career. I also thank Professor Williams Hageman for serving as a chair of my committee and conducting the final defense exam.

And, I would like to thank the strong support from our department head Professor Bradley A. Kramer. I would also like to acknowledge the faculty and staff of our department for offering me with a tremendous graduate education. They have taught me how to think about industrial engineering and scientific problems and provided me with the foundation for becoming a well-training engineer or scientist. I appreciated Professor Zhijian Pei for the guidance and assistance of the written exam of Ph.D preliminary.

I would also like to express my thanks and appreciation to everyone who has helped and encouraged me with this research effort. In particular, I am very grateful to the following people for their collaboration and advice while doing my research: Mr. Xiaoming Yu, Dr. Shouyuan

Chen, Dr. Baozhen Zhao, Dr. Xinwei Shen, Dr. Pengfei Zhang, Dr. Sabih Khan, Dr. Ximao Feng, Mr. Yan Chen and Qi Zhang.

I thank my parents and all other family members for supporting me in all my decisions, continuously motivating, and believing that I can do it. Thanks for all your love, and support.

Finally, I would like to thank my husband, Jianwei Liu, for giving me confidence and many advices on my study and research; as well as my daughter, Liying Liu, for their love, patience, support, happiness during all these years for keeping me motivated.

Chapter 1 - Introduction

1.1 Motivation

Femtosecond (fs) laser has opened a new era of micromachining since it was first demonstrated in 1994 [1]. Its precision, high peak power, flexibility, non-thermal interaction, and wide range of materials (e.g. fragile, ultra-thin and highly reflective surfaces) provide many advantages in micromachining for material processing applications. The fs lasers with pulse duration of ~100 fs have been widely used for micromachining because damage to the surrounding is mostly eliminated in dielectric materials [2] and heat affected zones in metal can be minimized [3, 4]. The main characteristics of fs laser pulses are very high peak intensity up to 10^{14}W/cm^2 and rapid deposition of photon energy into the materials. At this high intensity, the onset of optical breakdown that initiates ablation can be more deterministic [5] and a wide range of materials can be machined due to the nonlinear process taking place at this intensity. The benefits of ultra-short laser pulses arise because the pulse duration $\tau \sim 100$ fs is less than the equilibrium time of electron and lattice-ions subsystems $\tau_{ei} \sim 1–10$ ps [6].

In addition, the time needed for the electron thermal energy diffusion to reach the optical penetration depth is several orders of magnitude longer than τ_{ei} [5]. The short pulse duration can eliminate the effects of hydrodynamic motion of the matter during laser irradiation [6]. The short pulse also can prevent the shielding of incoming laser beam by plasma from the ablated surface, which can maximize absorption efficiency [7].

Fs lasers have been employed in processing a wide variety of materials by previous researchers. However, the foregoing research in fs laser micromachining is still not far from the

concept-proving stage and the fs laser matter interaction mechanisms remain unclear. There is a significant amount of innovative work that remains to be done to realize the potential of fs laser micromachining as an alternative machining process for different types of materials. For example, while the soft polyuria aerogel material has the special property and hard to process using traditional machining techniques, there is a need to explore fs laser processing of such material. Also, laser deep micro-hole drilling is always a hard research topic in laser micromachining, it is necessary to study fs laser drilling of high aspect holes. Moreover, if fs laser can be used for thin film solar cell fabrication, the production cost will be reduced and the performance of the solar cell will be improved. Therefore, high precision solar cell scribing using fs laser ablation is investigated and presented in this thesis.

1.2 Literature review

In this section, a wide range of micromachining techniques for micro-drilling, cutting and thin film scribing are reviewed. Fs laser micromachining process is compared to other processes and its advantages are discussed based on the review of previous work. The basic configuration of fs laser system and experiment setups used for this thesis are presented.

1.2.1 Micromachining technologies

There are many products associated with micromachining such as engine blades, irrigation needles, fuel injectors, high resolution circuitry, flow control devices, medical devices and so on. Various techniques have been used for the manufacture of micro-products including mechanical, micromachining, electrical discharge machining (EDM), chemical etching, photolithography, and laser ablation. The mechanical techniques such as micro-drilling and micro-cutting have low efficiency due to chip generation, friction heating at the cutter/sample

interface, and potential burr formation in the micromachining process [8, 9][10]. Electrical discharge machining (EDM) and electrochemical micro-drilling (ECM) [11, 12] also have low efficiency and high machining cost. Some other types of micromachining techniques such as chemical etching [13] and lithography are widely used micromachining tools. However, Chemical etching is not precise for micromachining as we can see from Table 1. Lithography is an alternative method to silicon-based micromachining and it provides a convenient, effective, and low-cost method for patterning [14-17]. However, it still requires multiple steps from the development of appropriate masters to a working device and residual chemicals remaining after the process that can be toxic to the environment.

Table 1-1 Comparison of micromachining processes [65]

Process	Resolution (μm)	Surface Roughness (μm)	Side Effects
Mechanical Micromachining	100	6.3-1.6	Burring, requires polishing
EDM	100	4.75-1.6	Electrode wear, rough finish, slow and unclean process
Chemical Etch	250	6.3-1.6	Undercutting
LIGA	5	1-2	Synchrotron source: very expensive
Nd: YAG Laser	50	1	Re-deposition
Excimer Laser	5	> 1 μm	Recast Layer, aspect ratios
Ti:sapphire Ultrafast Laser	< 1	nm range	Higher power ranges may require vacuum environment

1.2.2 Laser micromachining

Table 1 shows the comparison of different micromachining processes. As we can see from the comparison, from the precision point of view, there is no doubt that laser ablation can provide high quality finishing results.

In recent years, micromachining by nanosecond (ns), picoseconds (ps) and femtosecond (fs) lasers has been intensively studied and achieved various degrees of success [13-15]. Compared with ns and ps lasers, fs lasers are regarded as the potentially ideal tool for precision micromachining. Fs lasers deposit the energy into the material in a very short time, thus causing a very small heat affected zone (HAZ) and minimizing energy loss into the bulk material [16]. In contrast, in ns and ps machining, the thermal relaxation wave propagates into the bulk creating a relatively large layer of melted material, some of which is not removed but re-solidifies and thus forming recast layer, craters, debris, spatters or burrs [5, 18-20]. An example of the holes drilled by ns and fs laser is shown in Figure 1.1. The thermal effect and recast layer can be clearly seen from the hole on the left in Figure 1.1 which is drilled by ns laser. The fs laser drilled hole as shown on the right is clean and without collateral damage. Gebhardt *et al*. found that the ps and fs lasers only slightly damaged the substrate [21] compared to the trials with ns lasers as shown in Figure 1.2.

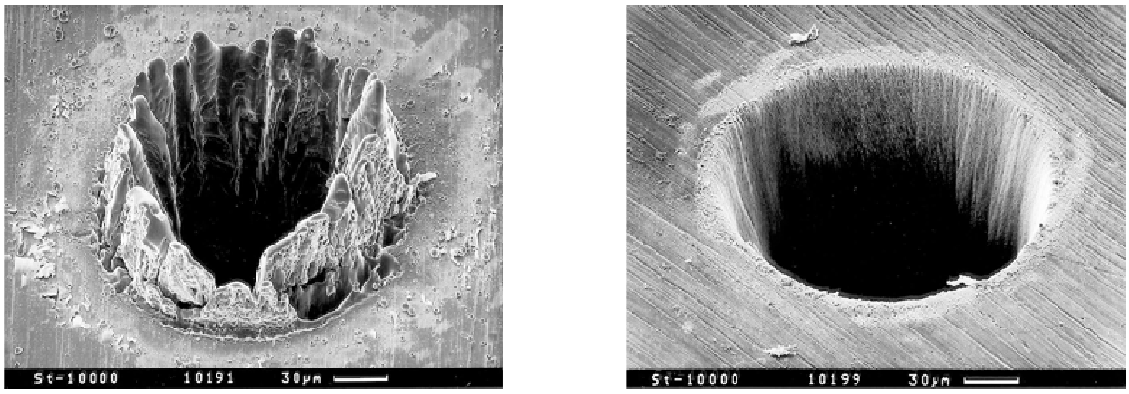

Figure 1-1 Comparison of holes drilled in a 100 µm-thick stainless steel foil using 3.3 ns (left) and 200 fs (right) pulses. In both cases fluences just above the ablation threshold and 10,000 pulses have been used [22]

Fs lasers have been used for material processing with less collateral damage in dielectric materials [23] and reduced heat affected zone in metal [24]. The major benefits of an ultra-short laser pulse include its ability to produce very high peak intensity and rapid deposition of energy into the material. It is a well-known fact that the principal characteristic of fs pulses, which makes process advantageous for micromachining, is that the pulse duration is shorter than the time (~1 ps) for equilibrium between electron and lattice-ions subsystems. In addition, the time needed for the electron heat diffusion to reach the optical penetration depth is several orders of magnitude longer than the duration of fs pulse [25]. A short duration can eliminate the hydrodynamic motion of the matter during laser irradiation and no fluid dynamics is involved during the laser and matter interaction [26, 27].

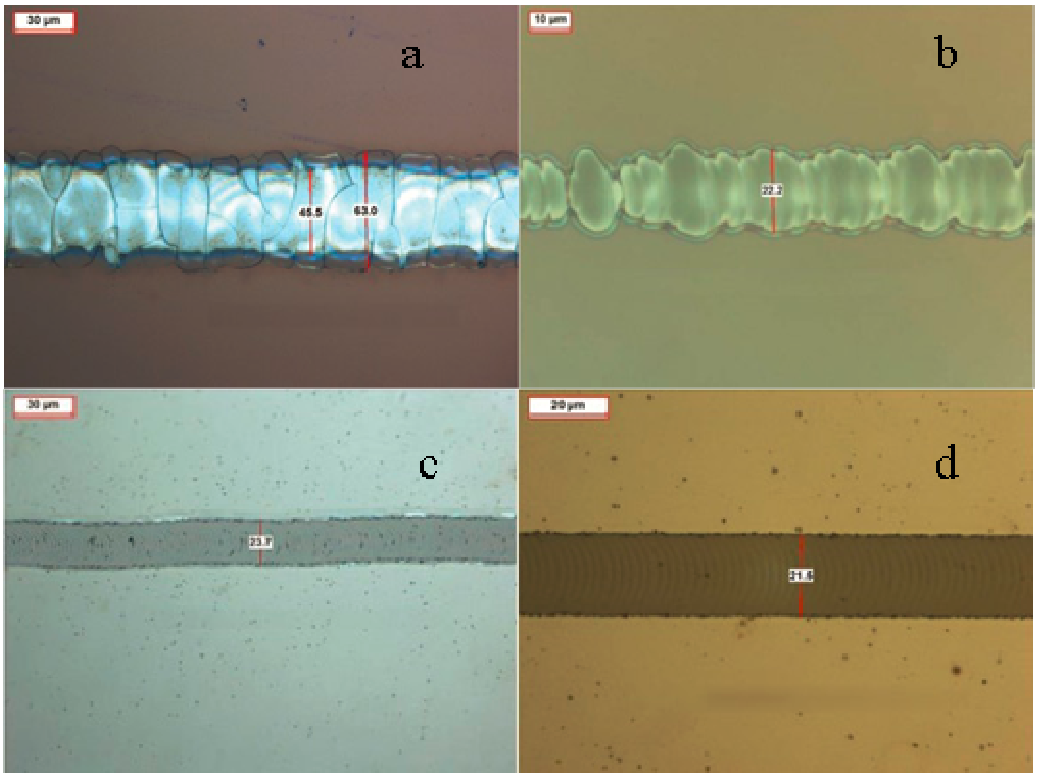

Figure 1-2 (a) ITO on glass substrates by nanosecond laser at 1064 nm;(b) ITO on glass substrates by nanosecond laser at 355 nm ;(c) ITO on PET polymer substrates by picosecond laser at 1064 nm (d) ITO on PET foil substrates by femtosecond laser at 1024 nm [21]

1.2.3 Laser thin film scribing for thin film solar cells

Laser processing offers a non-contact, clean scribing process with repeatable properties which is ideal for the segmentation and interconnection of thin-film modules. However, the area that the scribes occupy on the modules is not active and cannot contribute to electricity generation in the module. Therefore, it is imperative that the laser tool used has a high accuracy for the scribe positioning to allow good alignment between laser scribes to minimize the 'dead zone' and to maximize the active area of the module and hence the module power. At the same time, the scribing quality is directly related to the module efficiency. For example, if the

residuals were left at the patterning of the back conductor (P1) groove bottom, the adjunct cells could not be effectively separated and the module efficiency will drop. Therefore, the interconnect groove quality plays an important role for the module efficiency. The ideal case is that the P1, P2 (patterning of the absorption layer), and P3 (patterning of the front conductor layer) grooves are precise and narrow in width without any defects such as micro-cracks.

1.2.3.1 Thin film solar cells

The thin film solar cell has attracted much attention for years due to greatly reduced semiconductor material consumption and the ability to (a) fabricate the solar cells on inexpensive large area flexible substrates and (b) to monolithically series interconnect the fabricated solar cells, and hence thin-film PV has the potential of achieving lower module costs [28, 29].

There are three major thin film solar cell technologies according to the absorption material including amorphous silicon (α-Si), cadmium telluride (CdTe) and Cu $(In_{1-x}Ga_x)Se_2$ (CIGS). Amorphous Si has its place in consumer applications as well as mature manufacturing technology mainly for indoor use. The highest demonstrated cell efficiencies can reach 15.6 %. Module efficiencies are in the 6–8% range. Comparing with the other two technologies, it has lower efficiency. CdTe technology has several advantageous properties such as ideal material, and low cost manufacturing. Therefore, many efforts were made towards the large scale fabrication of modules. Laboratory cells can reach efficiencies above 16.7%. A non-technical problem associated with CdTe is the acceptance in the market place because Cd and to a lesser extent Te are toxic materials. CIGS is a technology based on the multinary compound semiconductors CIGS [28, 30]. CIGS has very high efficiencies approaching 20.3% reported for

laboratory scale devices[30]. More improvements can be expected in the near future by improving the fabrication processes and material property [28, 31-33].

1.2.3.2 Laser patterning of thin film solar cells

Thin film solar cells can be produced by an alternating sequence of layer deposition and layer patterning steps, which leads to series-connected solar modules as shown in Figure 1.3. Besides the deposition processes and the absorption material property, the scribing process for the interconnection grooves is another key aspect for thin film solar cell technology to reach low unit cost and high efficiency. The P1 scribe must penetrate completely through the full thickness of the back contact Mo layer on the substrate. This scribe isolates the individual cells with an effective resistance of tens of mega ohms. The P2 scribe through the absorber layer is important for formation of the series interconnects between two cells. By cutting through both the front-contact and semiconductor absorption layers, the P3 scribe isolates adjacent cells. The integrity and continuity of the P3 scribe are as critical as that of P1 scribe. The area of the module is divided into series connected cell stripes by the scribe patterns. This series connection leads to a reduction in the current density, and a decrease of the ohmic losses in the conducting layers. However the active module area is also reduced, since the patterned regions (dead area) no longer generate solar energy [34-36].

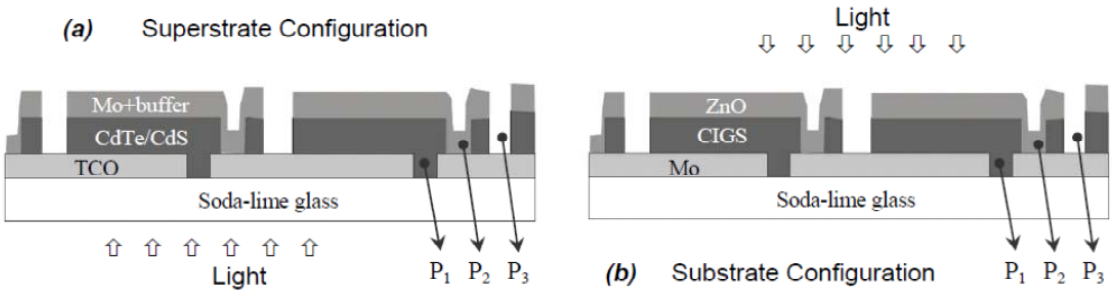

Figure 1-3 Typical interconnect scheme for: (a) CdTe/CdS, (b) CIGS solar cells[37]

High efficiency combined with the low cost roll-to-roll fabrication process makes CdTe and CIGS the most promising candidates for competition with crystalline Si technologies in terms of production cost and device performance. Further developments are directed towards improving understanding the materials, especially the surface and junction properties, as well as the reduction of film thickness and development of novel fabrication processes [38].

On the fabrication process side, monolithic integration of cells into large-scale panels is widely employed in order to improve cell efficiency, yield and overall manufacturability of the cells which all lead to lower cost. To lower the unit cost, the requirements for the laser scribing is listed as below:

- Narrower scribe widths enabling higher efficiency by increasing the active area. For example less than 40 micrometers
- Faster process time to improve throughput
- Improved scribe quality meaning less defects and micro-cracks.
- Laser scribing of challenging materials such as those used in CIGS and CdTe devices
- Improved scribe positional accuracy

As we can see from Figure 1.4, an example from Oerlikon Solar, by narrowing the dead area from 500 μm down to 200 μm, the dead area percentage can be reduce by 4% [39].

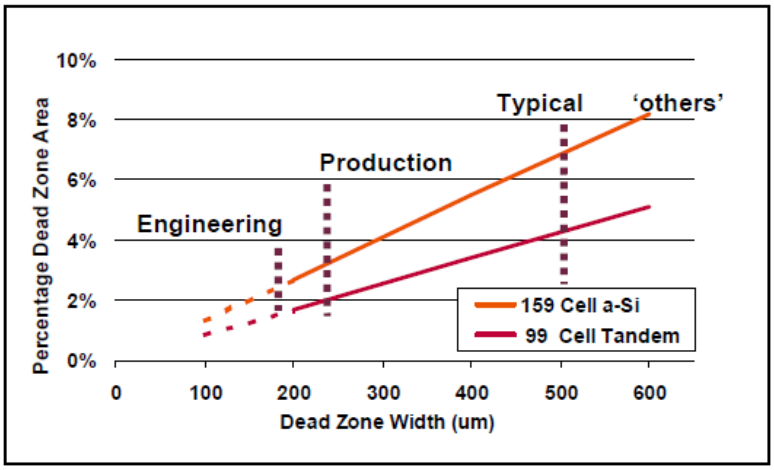

Figure 1-4 Effect of laser dead zone on active area for a Oerlikon Solar amorphous and micromorph tandem modules[39]

The CIGS and CdTe modules share common characteristics and device structural elements. The ongoing need for improvements in these areas is promoting both growth and research in the laser processes for both CIGS and CdTe thin film solar cells.

Several approaches for scribing CIGS modules on flexible substrate foils were tested and evaluated during the last decade. Various types of lasers are employed for P1 scribing. DPSS Q-switched lasers with 1064 nm and 532 nm wavelengths are the most common choice in industry. Laser pulse in the range of 10s of nanoseconds combined with 10s of mJ pulse energy levels provides sufficient intensity for most film removal tasks. However, Mo can be projected onto the walls of the ablation channel due to the thermal effect of ns laser scribe, which results in reduced module conversion efficiency [34, 36, 40]. According to the theoretical analyses, damage free thin film solar cell scribing requires shorter laser pulse durations [41, 42]. Lasers with ps pulse duration were applied for P1 scribe to reduce the thermal effect of laser ablation. Gecys and Raciukaitis claimed that the ps laser with wavelength 355 nm can be used for P1 scribe without a significant damage to the underneath layers [43, 44]. They also found that the ps pulse duration

can prevent extensive formation of the melt and no mixing of Mo with CIGS was found. Although the ps laser P1 scribe has shown better results on glass substrate comparing to the ns laser scribe, it could not produce the desired results on polymer and metal flexible substrates.

P2 and P3 scribe in CIGS thin film solar cells are usually accomplished by mechanical and photolithographic methods. Commonly in industry, the P2 and P3 process are done by the mechanical methods using needle structuring, with which the dead area determined by the chip effect for a cell is up to 400~450 mm [45]. In this method, the needles have to be replaced every day and all needles have to be controlled individually. All of these factors make the fabrication costly. Photolithographic methods were investigated which in principle allow chemical and selective scribing of all layers. First attempts were made with photomasks and a spin-coated photoresist. This approach works for P1 and on small areas but is unsuitable for large areas and for P2 and P3. The adjustment of the photomasks for P2 and P3 (with regard to P1), however, is both time-consuming and unsatisfying as the flexible foil substrates are less planar and dimensionally less stable than glass substrates [38]. Using laser P2 and P3 scribing, the dead area for one cell can be reduced to within 200 mm and the active area can be increased by 4%, which combined with the easy adjustment and stable process makes laser a high efficiency scribing tool for the CIGS P2 and P3 scribes. As we discussed previously in the introduction section, the ns and ps lasers all have the limitations of melting the absorption layer for P2 and P3 scribes.

The ns, ps and fs lasers have been tested for scribing a CIS film at wide ranges of experimental conditions. Ns laser irradiation on CIS has been characterized by (1) a large lateral heat affected zone (HAZ), (2) an inter-diffusion of molten and resolidified CIS and Mo layers, and (3) extended cracks and rims presumably caused by thermal effects, while in ps laser scribing features, these thermal effects appeared to be less pronounced. However, a close-up

inspection of a few other processing conditions indicates some issues concerning the quality of the process, namely, (1) large droplets or debris (on the order of 1 μm or larger) as evident in Figure 1.5(a), (2), micro-cracks as shown in Figure1.5 (c,d), and (3) microscopic ripple and/or droplet patterns on the bottom ("valley") of the scribe (Figure 1.5(c)). Micro-cracks are of concern, since they can create an unwanted electrical isolation within back contacts and contribute to device failure, decrease of efficiency and crack to next deposited layer. FIB (focused ion beam) cross-sectioning shows that the crack propagated through the entire Mo thickness (500 nm), as shown in Figure1.5(d) [46]. Therefore, ps laser is not the ideal tool for P2 and P3 scribing.

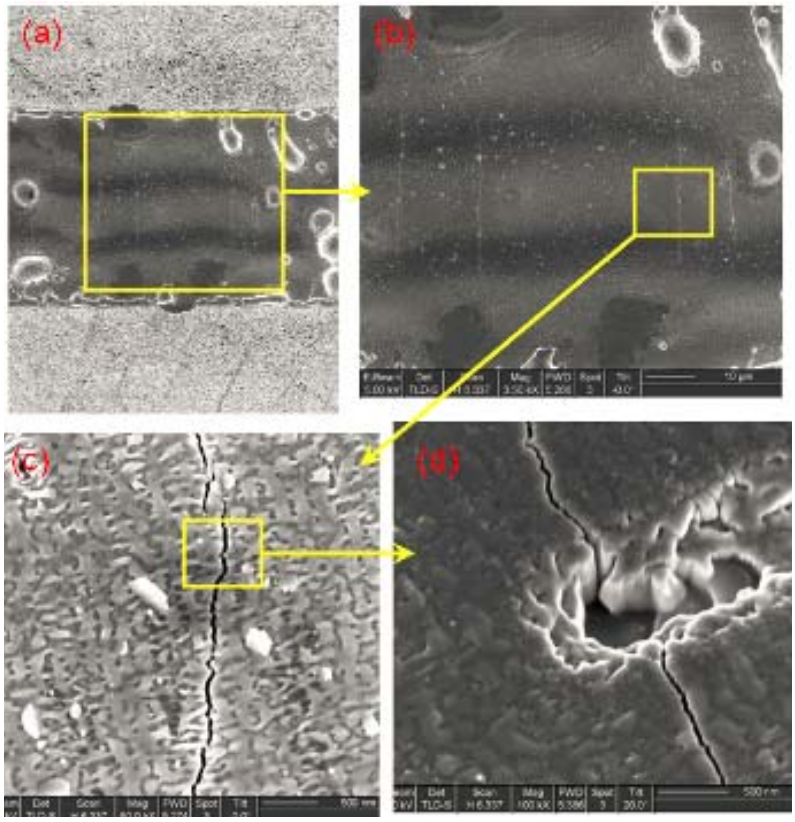

Figure 1-5 SEM image of CIS film scribed by a picosecond laser (λ = 532 nm, laser power = 3.5W, PRF = 250 kHz, scanning speed = 1 m/s) at different magnifications. FIB cross-sectioning in (d) shows the crack depth [46].

On the other hand, fs laser has shown advantages in thin film structuring such as free of cracks and little heat affected zone (HAZ). Hermann *et al.* demonstrated that fs laser was an effective tool to do the P1 scribing for CIS-based solar cell without relevant change in their photo-electrical properties theoretically and experimentally [41]. Zimmer *et al.* study concluded that fs laser can produce high quality laser scribing for photovoltaic applications [47]. Zoppel *et al.* demonstrated the potential of ultrafast lasers for structuring TCO and metallic layers for thin film solar cells [48]. With the high frequency fs fiber laser development, fs laser will be a promising tool for CIGS solar cell thin film P1, P2 and P3 scribe. Roll-to-roll machines for the chalcopyrite deposition on polyimide (PI) or metal foil flexible substrate are being optimized at various laboratories or companies such as Global Solar Energy. The fabrication of monolithically integrated modules on flexible metal foil substrates is still a big challenge and ongoing research [49].

As we discussed previously in this section, ns and ps lasers all have the limitations of melting the absorption materials for P2 and P3 scribes. For speed and simplicity, it is highly desirable to achieve all three scribing steps with one laser using a single wavelength for both rigid and flexible CIGS modules. Therefore, to establish such all-laser scribing capability, fs laser sribing for all P1, P2 and P3 should be explored.

1.3 Two temperature modeling and simulation of femtosecond laser ablation of Mo thin film

Up till now fs laser materials processing is still in the stage of laboratory research and not applied in industry. The fundamental machining mechanism which governs fs laser micromachining is not well understood so far, and as a result there is no effective guidance for parameter selection, especially how to optimize the thin film processing regime. Therefore, a

deep understanding of the material ablation mechanisms in fs laser processing of metal thin films is needed.

1.3.1 Proposed laser ablation mechanism

During the laser pulse irradiation time, laser energy is first absorbed by the electrons in the material. The electrons strike with each other and reach a thermal equilibrium in a few fs. The high temperature electrons exchange energy with the lattice, and the electrons and the lattice reach a thermal equilibrium on the time scale of picoseconds. The lattice within a shallow region from the surface heats up in a very short amount of time, nearly without a volume change. Materials can be removed at different states (density, volume, and temperature), depending on the laser parameters such as laser fluence.

For fs lase ablation, laser fluence is one of the most important parameters except laser pulse duration. If the applied laser fluence is a little higher than the ablation threshold, photomechanical spallation occurs with a dramatic phase change [52]. The driving force of the spallation is the compressive stresses and the hot-electron blast force generated by non-equilibrium hot electron gas [52]. Phase explosion dominates if the laser fluence is even higher [53]. During phase explosion, the peak temperature reached is a little below the critical temperature, and bubble nucleation occurs. The contribution of the tensile stress to phase explosion was also recognized. If the laser fluence is as high as a few times the threshold fluence, critical point phase separation is most likely to occur in this moderate fluence regime[54]. Vidal *et al.* described that fs laser induced local heating generates a local hydrodynamic pressure, which causes the ejection of hot material away from the material surface and the formation of a shock wave into the solid [54]. If the lase fluence is much higher than the ablation threshold fluence, the material is overheated above the critical point and the overheated

region is deeper than the skin depth due to electron heat diffusion [55, 56]. Nedialkov and Nolte proposed that the material is quickly transformed into gas (not a combination of gas and liquid as in phase explosion or critical point phase separation) with a steep rise in the pressure, which results in a much higher ablation rate at high laser fluence ablation [55, 56].

The fs laser induced material ablation involves very complicated physical processes that can be affected by little change of laser parameters or material properties. Even under the same given conditions, a conclusive explanation on the ablation mechanism has not been achieved.

1.3.2 Simulation of fs laser ablation

There are three typical models used in fs laser ablation modeling: two-temperature model (TTM), hydrodynamic model (HD), and molecular dynamics method (MD). TTM is used to describe the heat conduction processing in the solid region of the metal under ultra-short laser irradiation. The electrons and the lattice are treated as two sub-systems with energy coupling between them. TTM is based on the fact that laser energy is first absorbed by free electrons in the metal and then the electrons are relaxed by coupling with phonons. Parabolic TTM was proposed by Anisimov *et al.* [57].It is not accurate for pulse duration comparable with the electron relaxing time since the thermal equilibrium in the electron system is assumed for all time . The hyperbolic two temperature model was derived by Qiu and Tien [58]. It gives better results than the parabolic TTM for laser pulse durations comparable with the electron relaxing time for metals. Chen and Beraun proposed a dual-hyperbolic two-temperature model, which extended the Qiu and Tien's model by adding the relaxation behavior of and the heat conduction in lattice [59]. TTM is widely used because of its simplicity and acceptable accuracy in describing the energy transport mechanisms inside the solid target. Heat-affected zone and ablation rate of copper ablated by fs laser pulse was investigated using the parabolic TTM [60,

61]. An analytical solution of the TTM describing ablation of metals with Gaussian laser source was obtained with the assumptions that the lattice heat capacities and the thermal conductivity of the electron and lattice subsystems remain approximately constant during the process [62]. A very good agreement between the experimental data and simulation results was found by using the parabolic one dimensional TTM [63, 64].

However, many existing TTM models are based on some assumptions such as that the heat capacity of the thermal electrons and the thermal conductivity remain constant during the process of ablation, which may be invalid and have limitations. It is necessary to develop an efficient TTM model to understand the underlying physical processes during fs laser ablation and guide the Mo thin film ablation process.

1.4 Objectives and scope of this research

In summary, investigating fs laser micromachining for deep micro-hole drilling, cutting of difficult-to-machine materials and scribing for thin film solar cells is a worthy undertaking. The objectives of this research are as follows:

(1) To study the feasibility of fs laser ablation of polyurea aerogel.

(2) To study fs laser micro drilling of high aspect holes through a hollow core fiber

(3) To study fs laser scribing of thin film solar cells to achieve narrow groove width and high quality P1, P2 and P3 scribes.

(4) To investigate the mechanisms of fs laser interaction with Mo thin film material and to predict the single pulse ablation rate and crater geometry using TTM modeling and simulation.

This thesis is organized as follows. Chapter 1 is an introduction providing the motivation and the objectives of this work. A review of reported investigations on fs laser micromachining and laser applications in thin film solar cells is also included in Chapter 1. Chapter 2 is a feasibility investigation of fs laser ablation of polyurea areogel. Chapter 3 is an experimental study of fs laser drilling of micro holes through a hollow core fiber. Chapter 4 and 5 are experimental investigations on the effects of input variables of fs laser on monolithic interconnect groove quality for P1 patterning. Chapter 6 describes TTM model to predict the single laser pulse ablation rate and simulate the single pulse ablation crater geometry. The conclusions and future research are discussed in Chapter 7.

1.5 Reference

[1] D. Du, X. Liu, G. Korn, J. Squier, G. Mourou, Applied Physics Letters 64 (1994) 3071-3073.

[2] R.R. Gattass, E. Mazur, Nature Photonics 2 (2008) 219-225.

[3] S. Anisimov, N. Inogamov, Y.V. Petrov, V. Khokhlov, V. Zhakhovskii, K. Nishihara, M. Agranat, S. Ashitkov, P. Komarov, Applied Physics A: Materials Science & Processing 92 (2008) 939-943.

[4] N. Nedialkov, P. Atanasov, S. Amoruso, R. Bruzzese, X. Wang, Applied surface science 253 (2007) 7761-7766.

[5] X. Liu, D. Du, G. Mourou, Ieee Journal of Quantum Electronics 33 (1997) 1706-1716.

[6] R. Le Harzic, D. Breitling, M. Weikert, S. Sommer, C. Föhl, S. Valette, C. Donnet, E. Audouard, F. Dausinger, Applied surface science 249 (2005) 322-331.

[7] B. Salle, O. Gobert, P. Meynadier, M. Perdrix, G. Petite, A. Semerok, Applied Physics A: Materials Science & Processing 69 (1999) 381-383.

[8] T. Masuzawa, CIRP Annals-Manufacturing Technology 49 (2000) 473-488.

[9] D. Dornfeld, S. Min, Y. Takeuchi, CIRP Annals-Manufacturing Technology 55 (2006) 745-768.

[10] J. Liow, Journal of Cleaner Production 17 (2009) 662-667.

[11] K. Ho, S. Newman, International Journal of Machine Tools and Manufacture 43 (2003) 1287-1300.

[12] B. Bhattacharyya, J. Munda, M. Malapati, International Journal of Machine Tools and Manufacture 44 (2004) 1577-1589.

[13] Z. Huang, N. Geyer, P. Werner, J. De Boor, U. Gösele, Advanced Materials 23 (2011) 285-308.

[14] L. Stockman, G. Neuttiens, C. Van Haesendonck, Y. Bruynseraede, Applied physics letters 62 (1993) 2935-2937.

[15] M.A. Unger, H.P. Chou, T. Thorsen, A. Scherer, S.R. Quake, Science 288 (2000) 113-116.

[16] W.R. Childs, R.G. Nuzzo, Journal of the American Chemical Society 124 (2002) 13583-13596.

[17] Y. Xia, G.M. Whitesides, Annual review of materials science 28 (1998) 153-184.

[18] A.K. Dubey, V. Yadava, International Journal of Machine Tools & Manufacture 48 (2008) 609-628.

[19] R. Bogue, Assembly Automation 31 (2011) 6-11.

[20] Y. Iwai, T. Arai, T. Honda, R. Tanaka, T. Takaoka, Effect of pulse duration on scribing of ceramics and Si wafer with ultra-short pulsed laser, in: vol 5063, 2003, p. 362.

[21] M. Gebhardt, J. Hänel, Laser Technik Journal 8 (2011) 29-32.

[22] http://www.afs-jena.de/applications

[23] B. Stuart, M. Feit, A. Rubenchik, B. Shore, M. Perry, Physical Review Letters 74 (1995) 2248-2251.

[24] C.S. Montross, T. Wei, L. Ye, G. Clark, Y.W. Mai, International Journal of Fatigue 24 (2002) 1021-1036.

[25] E. Gamaly, A. Rode, B. Luther-Davies, V. Tikhonchuk, Physics of Plasmas 9 (2002) 949.

[26] E. Gamaly, A. Rode, B. Luther-Davies, Journal of applied physics 85 (1999) 4213.

[27] D. von der Linde, K. Sokolowski-Tinten, Applied Surface Science 154 (2000) 1-10.

[28] B. Rethfeld, A. Kaiser, M. Vicanek, G. Simon, Physical Review B 65 (2002) 214303.

[29] S.I. Anisimov, B.S. Luk'yanchuk, Physics-Uspekhi 45 (2002) 293-324.

[30] A. Goetzberger, C. Hebling, H.W. Schock, Materials Science & Engineering R-Reports 40 (2003) 1-46.

[31] K.L. Chopra, P.D. Paulson, V. Dutta, Progress in Photovoltaics: Research and Applications 12 (2004) 69-92.

[32] M.A. Green, K. Emery, Y. Hishikawa, W. Warta, Progress in Photovoltaics: Research and Applications 19 (2011) 84-92.

[33] F. Kessler, D. Herrmann, M. Powalla, Thin Solid Films 480 (2005) 491-498.

[34] K. Zajac, S. Brunner, R. John, C.A. Kaufmann, K. Otte, A. Rahm, F. Kessler, The German joint project "flexible CIGSe thin film solar cells for space flight", in: European Space Agency, Constance, Germany, 2008.

[35] P.O. Westin, U. Zimmermann, M. Ruth, M. Edoff, Solar Energy Materials and Solar Cells 95 (2011) 1062-1068.

[36] R. Bartlome, B. Strahm, Y. Sinquin, A. Feltrin, C. Ballif, Applied Physics B-Lasers and Optics 100 (2009) 427-436.

[37] S. Haas, G. Schope, C. Zahren, H. Stiebig, Applied Physics a-Materials Science & Processing 92 (2008) 755-759.

[38] A.D. Compaan, I. Matulionis, S. Nakade, Optics and Lasers in Engineering 34 (2000) 15-45.

[39] S. Selleri, A. Cucinotta, F. Poli, D. Passaro, High brilliance fiber lasers for the scribing of photovoltaic modules, in: IEEE, 2009, pp. 1-4.

[40] F. Kessler, D. Rudmann, Solar Energy 77 (2004) 685-695.

[41] H. Booth, Journal of Laser MicroNanoengineering 5 (2010) 183-191.

[42] M. Powalla, M. Cemernjak, J. Eberhardt, F. Kessler, R. Kniese, H.D. Mohring, B. Dimmler, Solar Energy Materials and Solar Cells 90 (2006) 3158-3164.

[43] J. Hermann, M. Benfarah, S. Bruneau, E. Axente, G. Coustillier, T. Itina, J.F. Guillemoles, P. Alloncle, Journal of Physics D-Applied Physics 39 (2006) 453-460.

[44] I. Matulionis, S. Nakade, A.D. Compaan, Wavelength and pulse duration effects in laser scribing of thin films, in: IEEE, Anaheim, CA, USA, 1997, pp. 491-494.

[45] G. Raciukaitis, P. Gecys, R. Trusovas, R. Kondrotas, Picosecond laser scribing for thin-film solar cell manufacturing, in: Laser Institute of America, Wuhan, China, 2010.

[46] P. Gecys, G. Raciukaitis, M. Gedvilas, A. Braun, S. Ragnow, Scribing of thin films with picosecond laser pulses for CIGS solar cells, in: vol 103, Laser Institute of America, Anaheim, CA, United states, 2010, pp. 1210-1219.

[47] G. Eberhardt, H. Banse, U. Wagner, T. Peschel, Structuring of thin film solar cells, in: vol 7585, SPIE, San Francisco, CA, United states, 2010, pp. The Society of Photo-Optical Instrumentation Engineers(SPIE).

[48] T.W. Kim, H.J. Pahk, H.K. Park, D.J. Hwang, C.P. Grigoropoulos, Comparison of multilayer laser scribing of thin film solar cells with femto, pico, and nanosecond pulse durations, in: vol 7409, 2009, p. 74090A.

[49] D. Ruthe, K. Zimmer, T. Hoche, Applied Surface Science 247 (2005) 447-452.

[50] S. Zoppel, H. Huber, G.A. Reider, Applied Physics A: Materials Science and Processing 89 (2007) 161-163.

[51] Udai P. Singh and Surya P. Patra, International Journal of Photoenergy 2010 (2010) 19.

[52] E. Leveugle, D. Ivanov, L. Zhigilei, Applied Physics A: Materials Science & Processing 79 (2004) 1643-1655.

[53] C. Cheng, X. Xu, Physical Review B 72 (2005) 165415.

[54] F. Vidal, T. Johnston, S. Laville, O. Barthélemy, M. Chaker, B. Le Drogoff, J. Margot, M. Sabsabi, Physical Review Letters 86 (2001) 2573-2576.

[55] S. Nolte, C. Momma, H. Jacobs, A. Tünnermann, B. Chichkov, B. Wellegehausen, H. Welling, JOSA B 14 (1997) 2716-2722.

[56] N.N. Nedialkov, S. Imamova, P. Atanasov, Journal of Physics D: Applied Physics 37 (2004) 638.

[57] S. Anisimov, B. Kapeliovich, T.L. PERELMAN, Zhurnal Eksperimental'noi i Teoreticheskoi Fiziki 66 (1974) 776-781.

[58] T. Qiu, C. Tien, Journal of Heat Transfer (Transactions of the ASME (American Society of Mechanical Engineers), Series C);(United States) 115 (1993).

[59] J. Chen, J. Beraun, D. Tzou, Journal of Electronic Packaging 123 (2001) 52.

[60] Y. Hirayama, M. Obara, Journal of applied physics 97 (2005) 064903-064903-064906.

[61] B.H. Christensen, K. Vestentoft, P. Balling, Applied Surface Science 253 (2007) 6347-6352.

[62] S. Vatsya, K.S. Virk, Journal of Laser Applications 15 (2003) 273.

[63] J. Byskov-Nielsen, J.M. Savolainen, M.S. Christensen, P. Balling, Applied Physics A: Materials Science & Processing 103 (2011) 447-453.

[64] J. Byskov-Nielsen, J.M. Savolainen, M.S. Christensen, P. Balling, Applied Physics A: Materials Science & Processing 101 (2010) 97-101.

[65] A Bulusu, SP Joshi, PS Shiakolas, ASME Conference Proceedings 2003(2003) 83-87

Chapter 2 - Micromachining of Polyurea Aerogel Using Femtosecond Laser Pulses

Published in: Journal of Non-Crystalline Solids, v 357, n 1, p 186-193, January 1, 2011

Author's Names: Qiumei Bian[a], Shouyuan Chen[a], Byung-Tai Kim[b],Nicholas Leventis[c], Hongbing Lu[d], Zenghu Chang[a], Shuting Lei[a]

Author's Affiliation:

[a] Kansas State University, USA

[b] Cheongju University, Republic of Korea

[c] Missouri University of Science and Technology, USA

[d] The University of Texas at Dallas, USA

2.1 Abstract

We successfully sliced cylindrical polyurea aerogel samples of 10~15 mm in diameter into 1~3 mm disks using femtosecond laser. The experiments are performed using a Ti:sapphire laser with 800 nm wavelength in ambient air with a pulse duration ~40 fs. We found that the laser fluence to breakdown this material is 1.3 J/cm^2. The ablation rate at different energy levels is evaluated. The factors influencing the ablation surface quality are investigated. The proper fluence to slice the porous polyurea is 6.4~8.9 J/cm^2 with the beam linearly scanning the sample at a speed of 0.1 mm/s, or 5.1~7.6 J/cm^2 with the beam circularly scanning the sample at a speed of 3.5~4 deg/s, and high quality machining surface is obtained with these conditions. The material removal mechanisms are proposed. Structural details of the machined area are characterized using a number of techniques such as optical microscopy and scanning electron

microscopy. This work provides insights for micromachining polymers with porous structures using femtosecond lasers.

Keywords: polyurea aerogel; femtosecond laser; SEM; micromachining

2.2 Introduction

The excellent mechanical and thermal properties, together with their unique porous structure, have made polyurea aerogels very attractive materials for many potential applications including lightweight, thermal and acoustic insulation, radiation shielding, and vibration damping [1,2]. Consequently, considerable effort has been made to fabricate the materials to various applications. But it is difficult to cut these materials using traditional machining operations such as cutting, milling, and grinding due to their soft and porous structure [2,3]. The recommended tool for cutting the aerogels is a diamond saw [2]. In particular, how to process the material and obtain good surface quality remains a challenge.

Ultra high intensity femtosecond laser has been extensively explored as a potentially fast and economical tool for micro/nano machining of various materials. The advantages of femtosecond laser machining include high precision with negligible collateral damage, no restriction to material type, and machining in the bulk [4]. Hence, femtosecond laser micromachining provides an alternative method to cut polymer materials due to its non-contact nature of material removal. In recent years, femtosecond laser micromachining has been developed to ablate micro-scale features in many materials including polymers [4, 5, 11, 12, and 18]. For example, femtosecond laser micromachining has been used to fabricate miniature devices using polymer materials including polyethylene [6] and silicone-based hydrogel polymers [7]. Also, ultrafast laser micromachining of silica aerogel has been reported [8].

Several operating factors that affect the micromachining process have been explored in the investigation, such as the linear transmission of laser light and the material breakdown threshold fluence of the silica aerogel material [8]. Meanwhile, femtosecond laser ablation of polytetrafluoroethylene has been investigated [9], and the experimental results indicate that a sufficiently large pulse number and the control of laser intensity are two key factors in obtaining a high quality microstructure.

In addition, the mechanism of light-matter interaction especially the ultrafast laser pulse-matter interaction is fundamentally important [13]. Femtosecond laser ablation mechanism of polymer material has been reported by Reyna and coworkers. And a photothermal model was presented in their paper [10]. However, there are few studies in laser processing of polyurea aerogels based on our knowledge. Therefore, the interaction that occurs between the laser pulse and the porous polymers needs to be investigated. Also, it is vital to obtain the right combination of laser ablation parameters in order to obtain the desired shape with good surface quality. To achieve this, an appropriate setting of laser intensity, pulse number and pulse duration as well as their ratio are of prime importance [12].

In this paper, we report femtosecond laser micromachining of polyurea aerogels in ambient air using a Ti:sapphire laser with 800 nm wavelength and 40 fs pulse duration. Furthermore, the material removal mechanisms are proposed.

2.3. Experimental Details

2.3.1 Experimental Setup

The experimental setup of the femtosecond laser micromachining system is schematically shown in Fig. 2-1. The femtosecond laser pulses are generated using a Ti:sapphire laser system, which can produce pulses with ~40 fs duration and at 800 nm center wavelength. The repetition rate is 1 kHz and the maximum pulse energy is 6 mJ. The laser beam diameter is 10 mm and the M^2 of the laser beam is 1.35. After a 50-50 beam splitter, a neutral density filter is used to adjust the laser pulse energy. A quarter-wave plate is used to generate a circularly polarized laser beam. The laser beam is focused by a lens with 500 mm focal length. It is focused at the sample center. The sample is mounted on a computer controlled micropositioning stage so that the sample can be rotated or translated in 3D. All the experiments are carried out in ambient air at atmospheric pressure and room temperature. After machining, the samples are analyzed using an optical microscope and a scanning electronic microscope (SEM).

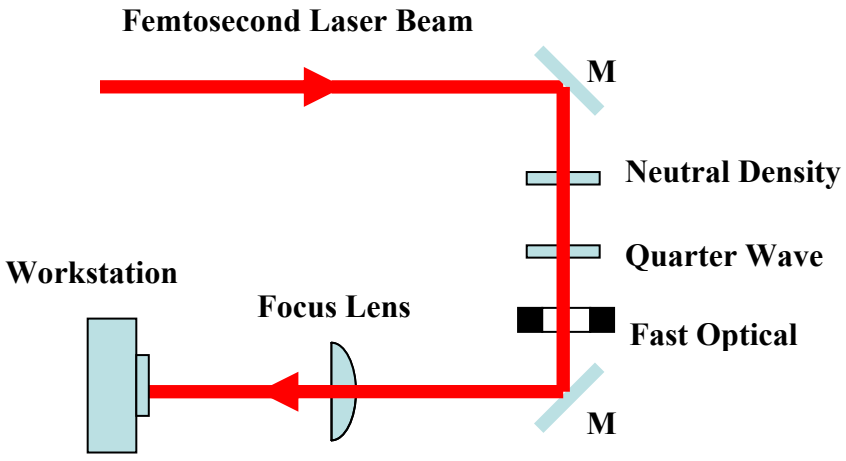

Figure 2-1 Schematic of the experimental setup

2.3.2 Sample Preparation

Polyurea aerogels of different densities were prepared by varying the concentration of Desmodur N3300A (courtesy of Bayer Corp) in the sol according to a modification of a process developed by Leventis [19]. Typically, low-density polyurea aerogels were prepared by mixing 5.5 g (0.0109 moles) of N3300A in 94 ml of dry acetone, 1.5 equivalents of water (0.2945 ml, 0.01635 mol) relative to the mol of N3300A in the sol and 0.327 ml triethylamine (ACROS, 99% pure, distilled, 0.3 % w/w relative to the total weight of Desmodur N3300A plus solvent used in the sol). The resulting sol was shaken vigorously and it was poured into polyethylene syringe molds and its gelation time was found to be 8 h. Higher-density polyurea aerogels were prepared by increasing the concentration of N3300A in the sol. Two types of high-density polyurea aerogels were prepared, one with 11 g (0.02108 moles) of N3300 A in 94 ml of dry acetone and another with 16.5 g (0.0327 moles) of N3300A in 94 ml of distilled acetone, by adding 1.5 equivalents of water relative to the mol of N3300A and 0.351 ml of TEA for 11 g of N3300 A and 0.375 ml of TEA for 16.5 g of N3300 A, and the gelation time was found to be 4 h and 2 h, respectively. After aging for a day both the low-density and high-density polyurea wet gels were washed with acetone, approximately 4 times the volume of the gel. The solvent was exchanged 2 times once every 24 h. Finally the wet gels were dried supercritically. The gelation time was found to vary with respect to the amount of catalyst and the amount of water added to the sol. Fig. 2-2 shows a high-density polyurea aerogel sample and its microstructure. The material looks like an assembly of nanoparticles at the microscale. It is highly porous with a porosity of ~85% and a density of ~0.2 g/cm^3. .

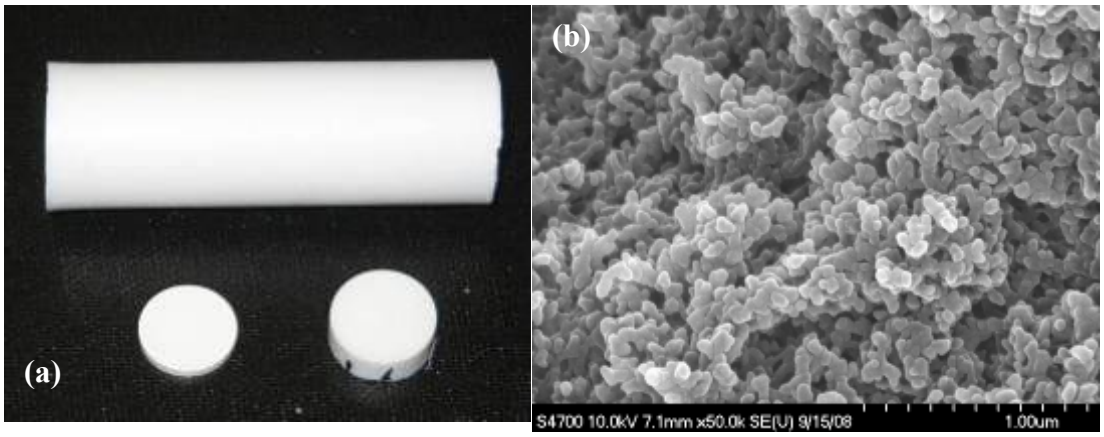

Figure 2-2 High-density polyurea aerogel sample (a) optical image of a cylindrical sample of 13 mm in diameter (b) SEM image of the porous polyurea particulate microstructure

In this study, at first laser ablation experiments are conducted to find the material breakdown threshold and ablation rate. Laser pulse number is controlled using a fast electronic fast shutter when we investigate the material breakdown threshold and ablation rate. The shutter has a 6 mm aperture and 150 Hz frenquency at continual running state. Also, the surface quality is investigated, together with the effect of the pulse energy and the sample scanning speed. The influence of the incident pulse energy and the sample scanning speed on the surface quality is studied separately. The average laser pulse power was measured by the portable laser power meter with ±1% accuracy and 3 mW to 10W measurement range. It was measured before the focusing lens. In order to offset random measurement errors, we averaged out of five measurements of the same simple quantity for laser pulse power as well as other parameters. The experiments to find the cutting parametric regime are studied in other two sets of experiment: a) the sample is mounted on the linear translation stage and the beam cuts through the whole sample and slices it off, as shown in Fig. 2-3(a); b) the sample is mounted onto the rotating stage

and the sample rotates around its own axis while the laser beam points towards the center of the sample at normal incidence, as shown in Fig.2- 3(b).

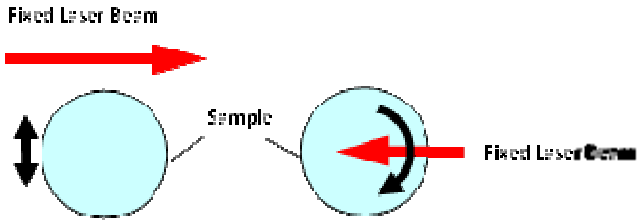

(a) Sample is translated (b) Sample is rotated

Figure 2-3 Schematic illustration of the cutting methods (a) sample mounted on 3D translation stage (b) sample mounted on rotary stage.

2.4. Results

2.4.1 Material Breakdown Threshold and Ablation Rate

Material breakdown threshold is a characteristic depending on the laser wavelength, pulse duration, repetition rate and number of laser shots. It is ideally defined as the energy fluence at which irreversible damage occurs in the material by removing a monolayer of material. It is actually determined by visual examination, ablation depth measurement, plasma radiation monitoring etc. In this study, the material breakdown threshold is estimated by measuring the diameter D of the ablated crater after ten shots using optical microscope and then using the following linear relationship between the square of the crater diameter and the logarithm of the laser fluence or energy [15, 20]:

$$D^2 = 2\, w_0^2 \ln(F_0/F_{th}) \text{ or } D^2 = 2w_0^2 \ln(E_0/E_{th}) \quad (1)$$

where F_{th} is ablation threshold fluence, F_0 is applied laser fluence, E_{th} is ablation threshold energy, E_0 is applied laser energy, and $2w_0$ is focal spot size. A plot of the square of damage diameter, D^2, against the logarithm of laser fluence is shown in Fig. 2-4. A linear fit is made to the experimental data. The slope of the line is two times the square of the spot size and the intercept of the extrapolated line with the horizontal axis is the ablation threshold. The spot size is found to be 115 μm and the ablation threshold is 1.3 J/cm^2 for the 40 fs pulse duration and 800 nm center wavelength. The spot size is slightly different from the CCD camera measured value of 105 μm because the pulse number in our experiment is ten instead of one. With the pulse number increasing, the ablated craters become greater resulting in the focal spot size slightly larger than the CCD camera measurement results. For comparison, the ablation thresholds of two other polymers PMMA and PC at 800 nm, 150 fs duration and 10 pulses are 1.5 J/cm^2 and 1.1 J/cm^2, respectively [20]. The slightly higher threshold for polyurea aerogel compared to these two polymers is because femtosecond laser ablation strongly depends on the type, dimensions and distribution of the filling material within the polymer matrix according to Moreno and coworkers [17].

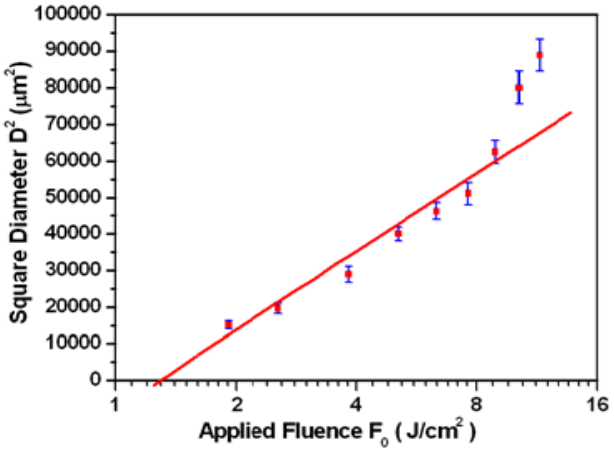

Figure 2-4 D^2 of the modified area versus pulse fluence

The average ablation rate is determined by measuring the depth of the ablated hole at 1000 and 5000 shots, as shown in Fig. 2-5. Compared to PMMA and PC the ablation rate is higher at the same energy level because of the high porosity of the material, i.e., 85% of the material in volume is air [20]. Most of the time, the beam propagates in air instead of interacting with the material. It can be seen from Fig. 2-5 that the average ablation rate at 1000 pulses is much larger than at 5000 shots for the same energy level. The difference could be attributed mainly to the following two factors. One is that the beam becomes more diverged after the depth is beyond the Rayleigh range according to the Gaussian beam property [9]. The other reason is because of the energy loss due to light scattering and dispersion, which becomes serious with the depth increasing due to the porous material. Beam scattering and dispersion were noticeable by making the surrounding materials glow during the ablation process. Both factors can cause the beam intensity to drop rapidly, resulting in the decrease of the average ablation rate because the subsequent pulses lose the ability to efficiently remove the material.

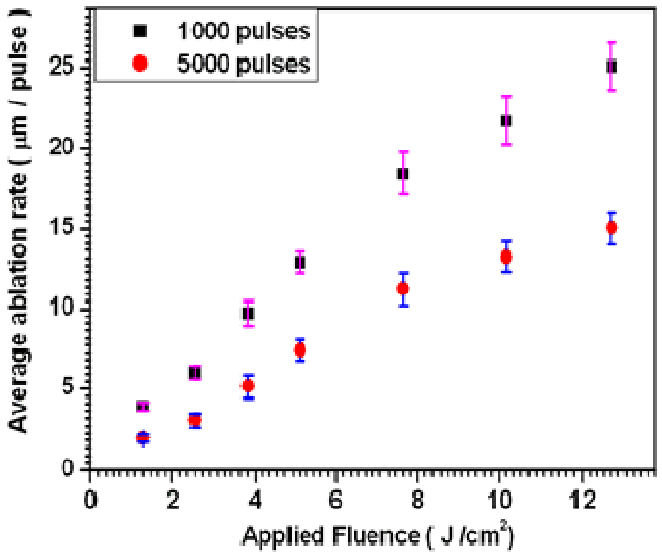

Figure 2-5 Average ablation rate versus pulse fluence

2.4.2 Surface Morphology and Quality

The periodic groove structure is observed on the ablated surfaces as shown in Fig. 2-6. Fig. 2-6 (a) shows the cutting surface with the sample linearly translating through the beam (the laser beam propagates from left to right and the sample moves orthogonal to the beam). The scanning speed is 0.1 mm/s and the laser fluence is 6.36 J/cm^2. It can be seen that the surface quality varies from the beam incident side to the beam exit side. The surface quality at the beam incident side (left side of Fig. 2-6 (a)) is much better than at the beam exit side (right side of Fig.2-6 (a)). SEM examination reveals that the incident side of the sample has small groove width, which is clearly seen in Fig. 2-6 (a) (b) (c). The images indicate that the incident side groove width and depth are about 80 μm and 30 μm, respectively, which is smaller than at the exit side, which are about 280 μm and 140 μm, respectively as shown in Fig. 2-6 (a) (d) (e).

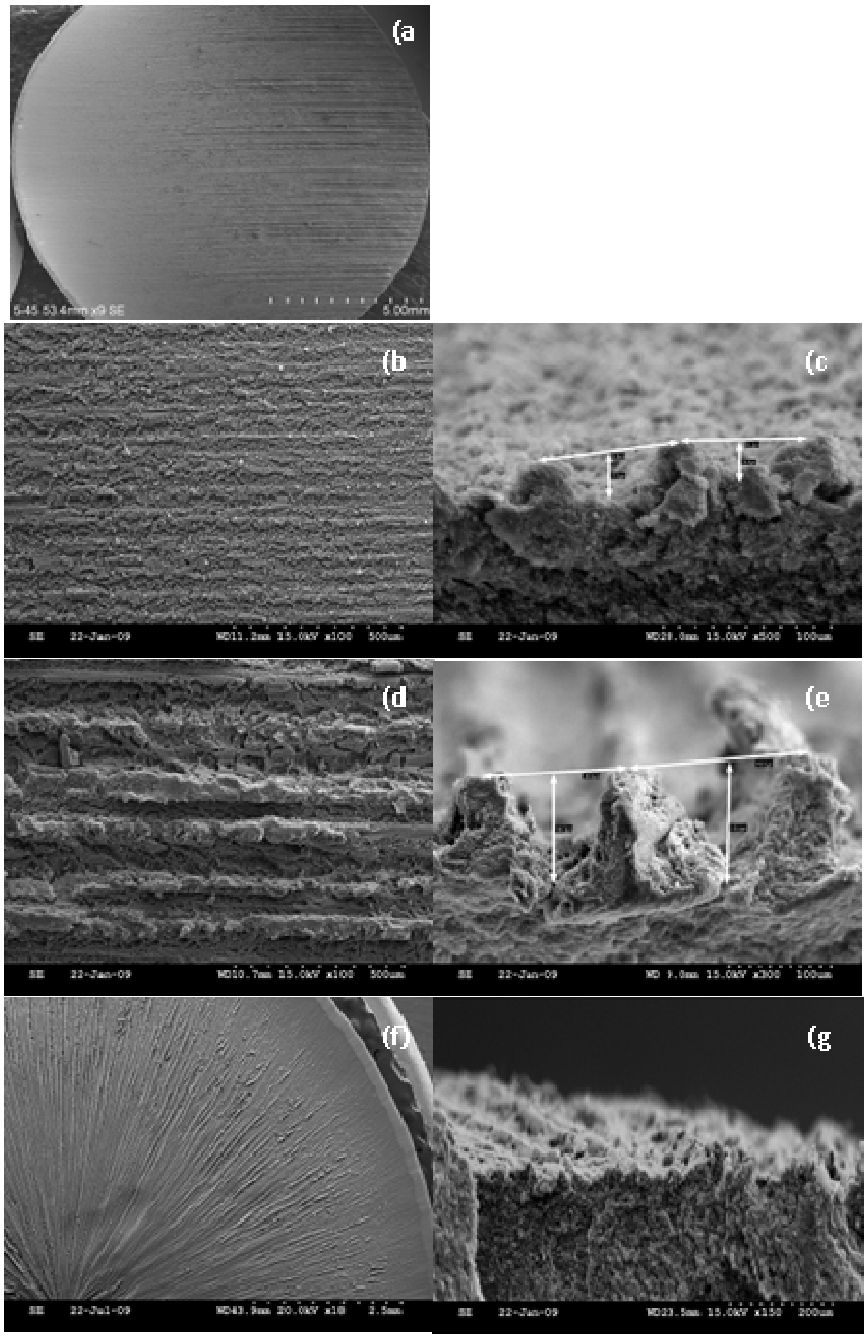

Figure 2-6 SEM images of typical cutting surfaces of polyurea aerogel (a) linear scanning speed of 0.1 mm/s and laser fluence of 6.36 J/cm2 (b) beam incident side of (a) (c) cross-section of incident side (d) beam exit side of (a) (e) cross-section of exit side (f) circular scanning speed of 4 degree/s and fluence of 5.1 J/cm2 (g) cross section of (f) at 2mm from the edge.

In order to improve the cutting surface quality we reduce the distance of beam propagating in the material by mounting the sample on the rotating stage with the beam circularly scanning the samples and thus the path of the beam interaction with the material is reduced to half comparing with the linear scan. Laser beam points to the center of the sample. The scanning speed is 4 degree/s and the laser fluence is 5.1 J/cm^2. This way a smaller surface roughness is achieved, as shown in Fig. 2-6 (f) (g). We can see that the groove width and depth are improved to less than the focal spot size at the center of the sample, which is much better than the results when the beam linearly scans the sample. However, now the grooves are distributed radially toward the sample center instead of parallel to each other.

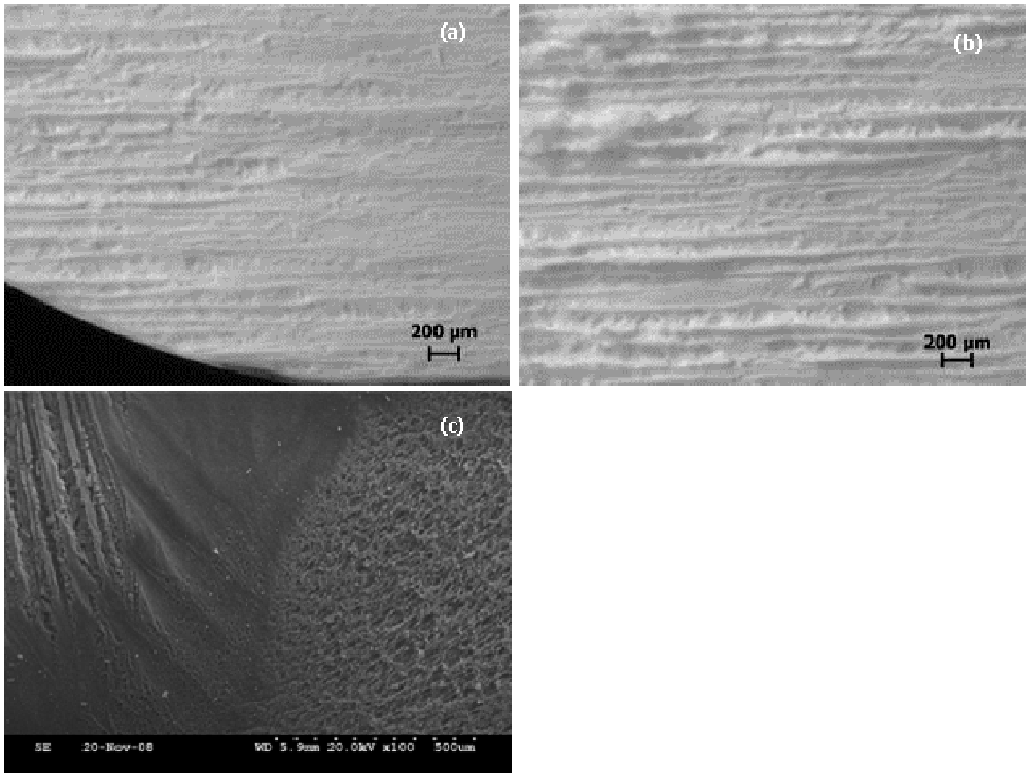

Figure 2-7 Images of cut surfaces showing the dependence of groove width and depth on the scanning speed at fluence of 6.3 J/cm2 (a) scanning speed at 0.05 mm/s (b) scanning speed at 0.2 mm/s (c) scanning speed at 0.02 mm/s

Besides the beam propagation distance in the material, the other key factors affecting the quality of the cutting surface are the sample scanning speed and the laser fluence. We studied the influence of them on the ablated surface quality in two separated sets of experiments. The beam spot size on the sample surface was 107 μm, measured using CCD camera. It was fixed because a long Rayleigh range is required in order to slice a cylindrical sample of more than 13 mm in diameter. A long Rayleigh range means a large focal spot size; therefore, the final focus lens and focal spot size of 107 μm are the results for the desired Rayleigh range. In the process of surface cutting, the sample is exposed to multiple pulses while being continuously translated at the scanning speed V. It is convenient to relate the scanning speed to an effective pulse number delivered in order to compare the results to the stationary process. The approximate relation that accounts for the effective pulse number incident over the distance of the beam spot size is given by

$$N=RS/V \tag{2}$$

where N is the pulse number, R is the pulse repetition rate, S is the beam diameter and V is the sample scanning speed [9]. The expression can be used to calculate the accumulated fluence of a series of pulses with a Gaussian intensity profile, peak fluence of φ_o and separated by V/ R, the distance traveled between pulses. It is important to point out that this is an approximate relation and is not expected to be completely equivalent to stationary processing with N pulses. Nevertheless it is instructive in a first analysis of the surface cutting results. In the subsequent discussions, all the references to the number of pulses are based on the conversion of the scanning speed V to the number of pulses N in Equation (2).

In the first set of experiments, the pulse energy (fluence) was held constant at E_0 = 0.5mJ (φ_0=6.3 J/cm^2) and the dependence of the surface quality on the scanning speed was investigated in the range of V=0.02mm/s-0.2mm/s (N=5000-500).

The results of this set of experiments indicate that the surface quality is inversely proportional to the scanning speed as shown in Fig. 2-7, with the scanning speed decreasing and the pulse number increasing the cutting surface becomes smoother. However, when the sample scanning speed decreases to 0.02 mm/s, the total amount of absorbed energy is very high, which results in the burned surface as shown in Fig. 2-7(c). In contrary, when the sample scanning speed is very fast, the material cannot be totally melted and removed due to the less amount of energy absorbed, therefore the surface is rougher as shown in Fig. 2-7(b). We found out that the suitable sample scanning speed is 0.1~0.12 mm/s when the pulse energy is 6.3 J /cm^2.

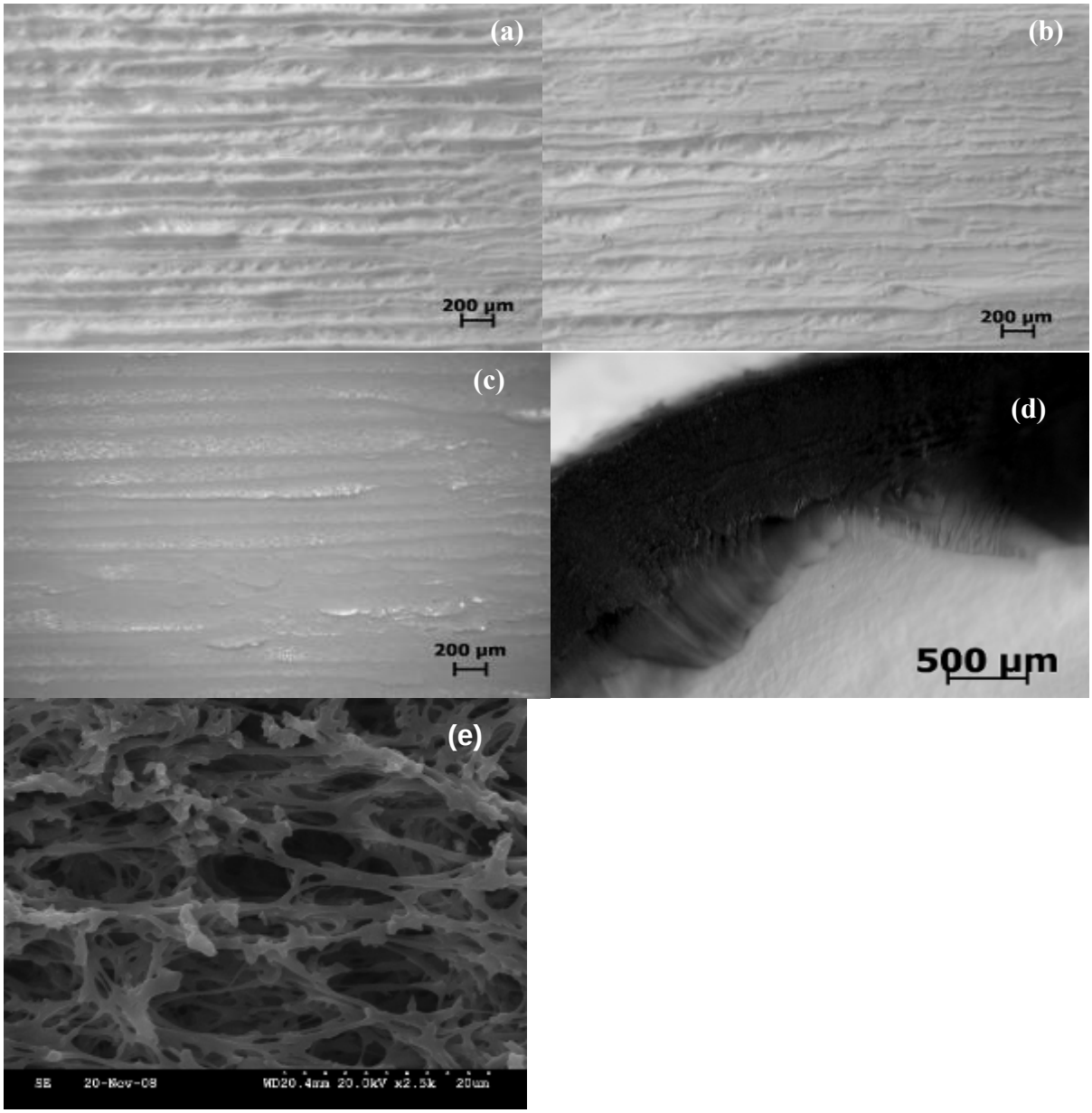

Figure 2-8 Optical microscope images showing the dependence of groove size on the laser fluence at the sample scanning speed of 0.1 mm/s (a) fluence= 5.7 J/cm2 (b) fluence= 8.9 J/cm2 (c) fluence= 11.5 J/cm2 (d) fluence= 14 J/cm2 (e) microstructure of the burned surface(SEM image).

In the next set of cutting experiments, the cutting surface was investigated as a function of pulse energy (fluence) in the range of E_0 =0.4-1.2 mJ/pulse (φ_0=5.1–15 J/cm^2), at the sample scanning speed of 0.1mm/s. The results are shown in Fig. 2-8 (a) (b) (c). The surface quality improves with the increasing beam fluence. However, if the fluence is increased to a critical value at certain scanning speed, e.g., 15 J/cm^2 at the scanning speed of 0.1mm/s in our experiments, the heat is accumulated so much that the ablation surface is severely melted and burned as shown in Fig. 2-8 (d). The material is melted and recasted into the weblike microstructure, as shown in Fig. 2-8 (e). The suitable energy (fluence) is found to be 0.5~0.7 mJ (6.3~8.9 J/cm$^{2)}$ at the scanning speed of 0.1 mm/s for the linear scan and about 0.4~0.6 mJ (5.1~7.6 J/cm$^{2)}$ at the scanning speed of 4 degree/s for the circular scan.

2.5. Discussions

Two main polymer ablation mechanisms have been proposed and discussed for more than two decades: photochemical model and thermal/photothermal model. Both ablation models are based on the fact that the energy from laser pulse is initially transformed into electronic excitations [21]. Therefore, the ablation of polymers usually is a combination of photochemical and photothermal phenomenon. The role of each can be varying for different polymer materials and laser irradiation wavelengths [22]. Although the polyurea aerogel in our experiments has the unique porous structure, it is still a polymeric material. Therefore the material removal is realized through a combination of photothermal and photochemical mechanism. On the other hand, for the high laser intensity used in our experiments, it is believed that the polyurea aerogel ablation process is fundamentally initiated through multiphoton ionization.

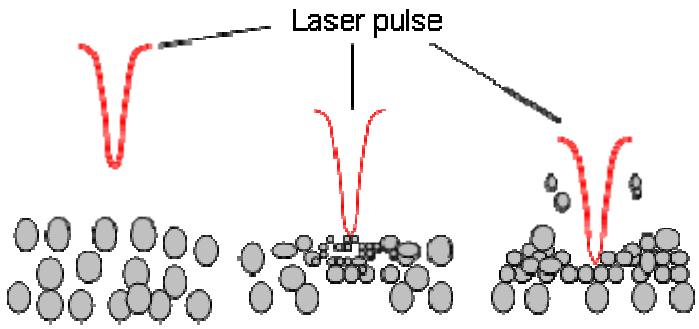

Figure 2-9 Schematic illustration of material removal mechanism

Fig. 2-9 illustrates the proposed laser ablation mechanism for polyurea aerogel. When laser pulse irradiates the porous material, the photon energy is converted into heat because of the photo-thermal process. The material under the laser beam may be broken into smaller particles that become softened or even melted. The fluidic polymer fragments then flow away towards the two sides due to Gaussian beam energy distribution and surface tension. Some material fragments may be vaporized and ejected from the surface. In the end the material is redistributed due to the Gaussian beam energy distribution and the groove structure is formed as shown in Fig. 2-10 (a) (b). With the sample movement, a series of grooves are created by the complex interplay of overlapping beam paths. The amount of the beam path overlap determines the energy deposited on a certain area. The more overlap, the more pulses and the more energy are deposited, and thus the smoother the formed surface. During the ablation process, the vaporized material may fall back on the newly formed surface as loose particles as shown in Fig. 2-10 (b).

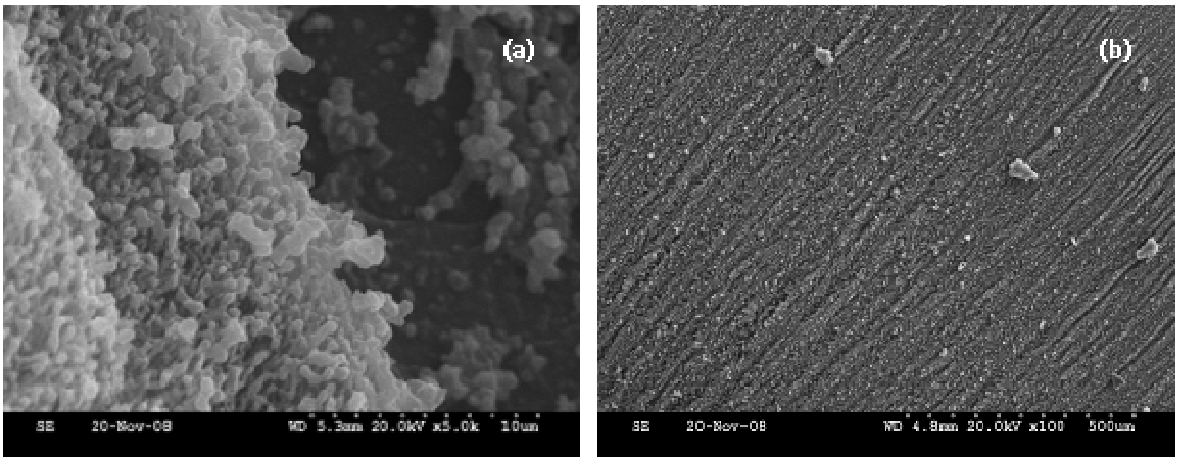

Figure 2-10 (a) SEM images of ablated surface (a) a groove peak and valley microstructure (b) surface showing ablation marks and particles

The deposit energy density is the key factor to material removal as shown in our previous results. We can see that the cutting surface quality improves with the beam fluence as shown in Fig.8. The groove width on the cutting surface increases with the beam fluence since more energy deposition causes more material to be melted. The result coincides with $\phi = \phi_0 \sqrt{\ln(I / I_0)}$ [23], where ϕ_0 and I_0 are ablated groove width and laser intensity at ablation threshold and I and ϕ are applied laser intensity and the corresponding groove width. With the intensity increasing more energy is absorbed by the material and the material removal ability of the beam increases and surface quality is enhanced. In addition, the energy density on the material is determined by the sample scanning speed. As we discussed, the scanning speed can be converted to the pulse number due to the fixed beam diameter and the pulse repetition rate based on Equation (2). The pulse number increases with decreasing scanning speed. Both the pulse number and the pulse energy can affect the energy density deposited on the material. We can adjust the energy density deposited on the material by tuning the sample scanning speed (pulse number) and the laser pulse intensity. However, the energy density decreases with the beam propagation distance in the

material because the laser light diffusely scatters in the porous material. When the pulse propagates to the exit side from the incident side, it gradually loses the material removal ability. Therefore, the surface roughness at the beam incident side is much better than at the beam exit side and this is reasonable since the pulse loses its ability to remove material after it propagates about 13mm when the sample is linearly translated.

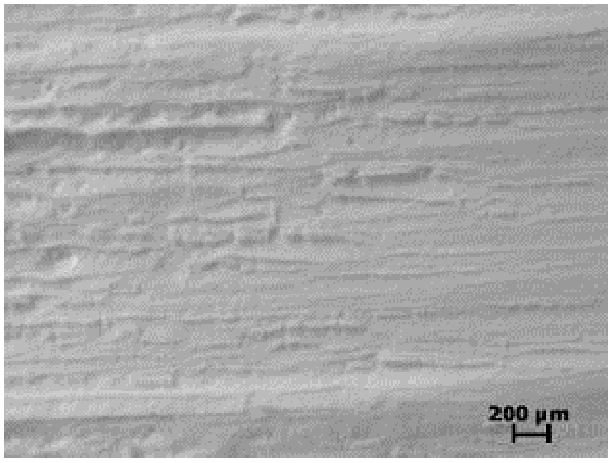

Figure 2-11 Optical microscope image of the ablated surface at fluence of 8.9 J/cm2 and scanning speed of 0.12 mm/s

A similar surface quality may be achieved by different combinations of scanning speed and beam fluence to obtain the same energy density and thus the same surface quality. For example, we increased the pulse energy from 0.5mJ (6.36 J/cm^2) to 0.7mJ (8.9 J/cm^2) while raising the sample scanning speed from 0.05mm/s to 0.12 mm/s to find that the surface morphology of the latter one is similar to the previous one, when comparing Fig 2-7 (a) and Fig. 2-11. For both cases, the total energy density deposited on the material is about the same. Therefore, higher pulse energy means that the ablation time can be shorter for the same amount of material removed, that is, the cutting efficiency is increased at the cost of the increased beam energy.

The formation of the rounded particulate microstructure, shown in Fig. 2-10 (a), also indicates that after the sample material absorbs enough energy from the laser pulse due to multiphoton absorption, it could decompose into small fragments and then melt into the rounded shape due to surface tension. The weak polymerization bond like C-O (3.6 ev), C=N (3.2 ev) and N-H (4.0 ev) are decomposed after multiphotoabsorbtion, which is consistent with the previously reported model and mechanism [10,14,16,17].

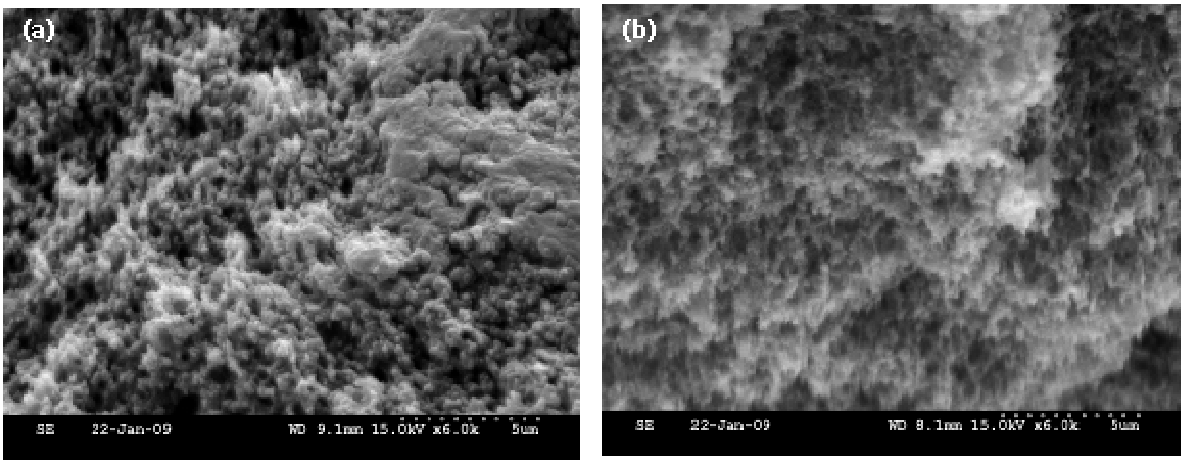

Figure 2-12 SEM image of (a) the cross section 10 um under the ablated surface (b) raw material.

Moreover, the porous microstructures are not destroyed by the laser pulse 10 μm beneath the ablation surface, as shown in Fig. 2-12(a). From Fig. 2-12, we can see that the porous particulate structure after laser ablation is similar to the intact material. This is attributed to the ultra-short laser-material coupling time and the low thermal conductivity of the material [3]. However, the particle size appears to be larger after laser ablation.

2.5. Conclusions

Polyurea aerogel is successfully machined using femtosecond laser pulses. The material breakdown threshold is found to be 1.7 J/cm^2 at 800 nm center wavelength and 40 fs pulse width. The material ablation rate at different energy levels is found to be on the order of tens of microns per pulse. The periodic groovy surface structure after laser cutting is explained by a proposed material removal mechanism that includes material melting and vaporization. An important factor of this study is to determine the optimum regime of laser micromachining to create the high quality cutting surface by investigating the influence of the key factors such as laser beam energy and sample scanning speed. The following parametric regime produces a high quality surface: the suitable beam fluence is 6.36~8.9 J/cm^2 while the sample is translated at the speed of 0.1~0.12 mm/s and 5.1~7.3 J/ cm^2 while the sample is rotated at the speed of 3.5~4deg/s. However, the surface quality is better with the beam circularly scanning the sample due to the reduced beam propagation distance. Based on the SEM image of the raw material and the ablated material we find that the porous microstructure remains the same at 10 um under the ablation surface. Owing to femtosecond laser's high precision with negligible collateral damage, femtosecond laser pulses can be used to successfully cut highly porous polymer materials.

2.6 Acknowledgments

Financial support of this work by the DoD Army Research Office under the Agreement Number W911NF-07-1-0475 is gratefully acknowledged. Leventis and Lu also acknowledge the support from a NSF collaborative project under CMMI-0653970 and CMMI-0653919**.**

2.7 References

[1] USPTO Application #: 20060211840.

[2] K.E. Parmeter, F. Milstein, J. Non-Crst. Solids 223 (1998) 179.

[3] J. Lee, G.L. Gould, W. Rhine, J Sol-Gel Sci. Technol. 49 (2009) 209.

[4] M. Ali, T. Wagner, M. Shakoor, P.A. Molian, Journal of laser applications 20 (2008) 169.

[5] J. Küger, W. Kautek, Adv. Polym. Sci. 168 (2004) 247.

[6] A.J. Lee, J.M. Dawes, M.J. Withford, Journal of laser applications 20 (2008) 154.

[7] L. Ding, R.I. Blavkwell, J.F. Kunzler, W.H. Knox, Applied optics 47 (2008) 3100.

[8] J. Sun, J.P. Longtin, P.M. Norr, J. Non-Crst. Solids 281 (2001) 39.

[9] Z.B. Wang, M.H. Honga, J. Appl. Phys. 93 (2003) 6375.

[10] L.G. Reyna, Z J. Watson, J. Appl. Phys. 78 (1995) 3423.

[11] J. Kru¨ger, S. Martin, H. Ma¨debach, L. Urech, T. Lippert, A. Wokaun, W. Kautek, Appl. Surf. Sci. 247 (2005) 406.

[12] C.R. Mendonca, S. Orlando , G. Cosendey, M. Winkler, E. Mazur, Appl. Surf. Sci. 254 (2007) 1135.

[13] S. Juodkaz, V. Mizeik, S. Matsuo, K. Ueno, H. Mawa, Bull. Chem. Soc. Jpn. 81 (2008) 411

[14] T. Lippert, J.T. Dickinson, Appl. Surf. Sci. 127 (1998) 117.

[15] J.M. Liu, Optics Letters 7 (1982) 196

[16] Y.S. Lee, X. Wen, W.A. Tolbert, D.D. Dlotta, M. Doxtader, D.R. Arnold, J. Appl. Phys. 72 (1992) 2440.

[17] P. Moreno, C. Me´ndez, A. Garcı´a, I. Arias, L. Roso, Appl. Surf. Sci. 252 (2006) 4110.

[18] R. Gattass, E. Mazur, Nat. Phot 2 (2008) 219.

[19] S. Mulik, C Sotiriou-Leventis, N. Leventis, Chem Mater 20 (2008), 6985.

[20] S. Baudach, J. Bonse, J. Kruger, W. Kautek, Appl. Surf. Sci. 154 (2000) 555.

[21] T. Lipper, J. Dickinson, Chem. Rev. 103 (2003), 453.

[22] L. Urech, T. Lippert, C.R. Phipps, A. Wokaun,. Appl. Surf. Sci. 253 (2007) 6409.

[23] S. Guizard, A. Semerok, J. Gaudin, M. Hashida, P. Martin, F. Que˜re˜, Appl. Surf. Sci. 186 (2002) 364.

Chapter 3 - A Study on Laser-Fiber Coupling Efficiency and Ablation Rate in Femtosecond Laser Deep Microdrilling

Published in: Int. Journal of Mechatronics and Manufacturing Systems, 5, No. 3/4, 2012

Author's names: Xinwei Shen[a], Qiumei Bian[a], Zenghu Chang[b], Shuting Lei[a], Benxin Wu[c]

Author's Affiliation:

[a] Kansas State University, USA

[b] University of Central Florida Orlando

[c] Illinois Institute of Technology

3.1 Abstract

Laser micro-drilling is a common micromachining operation in many industrial applications. This paper presents a new laser micro-drilling technique in which a hollow core fiber is employed to transmit femtosecond laser pulses to the target position. The coupling efficiency between the laser and the fiber is investigated and found to be strongly related to pulse energy and pulse duration. A parametric study on the average ablation rate indicates that in micro-drilling of a stainless steel (type 303), all the parameters including pulse energy, pulse duration, sample thickness, focal length and sample-fiber distance affect the ablation rate. The experimental results show that the new technique developed in this study is feasible to conduct micro-drilling of high aspect ratio micro-holes.

Keywords: Femtosecond laser, micro-drilling, ablation rate, hollow core fiber, stainless steel

3.2. Introduction

There are many products associated with micro-drilling such as engine blades, fuel injectors, high resolution circuitry, flow control devices, medical devices and so on. A conventional technique to produce micro-holes is by mechanical micro-drilling [1, 2]; however, this technique has low efficiency due to chip generation, friction heating at the cutter/sample interface, and potential burr formation in the micromachining process [3]. Nonconventional techniques like electrical discharge machining (EDM) and electrochemical micro-drilling (ECM) [4, 5] also have low efficiency and high machining cost. Other nonconventional techniques such as chemical milling [6], electro-forming and plating [7, 8], electron beam drilling [9], ion beam milling [10], mechanical punching/broaching [11], and glass fiber forming [12] have limitations in terms of the requirements for equipment or sample materials. However, laser micro-drilling, especially with ultra-short pulsed lasers, does not have such limitations and can produce micro-holes with high quality and high aspect ratio.

Existing techniques for laser micro-drilling (single-pulse, percussion, trepanning and helical drilling) [13] are only suitable for the types of target that a laser beam can directly strike. For target samples with complex geometries that laser beam cannot directly reach, an alternative technique must be used. In this study, the laser beam is directed to propagate through a hollow core fiber and then reach the target surface.

Due to the flexibility in the design of the machining system, laser beams delivered through a fiber have been used in laser machining [14-17] and laser assisted machining [18]. The requirement for the beam quality in these applications is generally less stringent. However, for micromachining applications, high beam quality is particularly needed due to the small feature size. Currently, single mode hollow core fibers are commonly adopted to transmit a high-quality

laser beam. Dekel *et al.* [19] coupled the CO_2 laser pulses into a single mode hollow core glass fiber for marking a polyvinyl chloride (PVC) plate. Konorov et al. [20] used a single mode hollow core photonic-crystal fiber to transmit picosecond pulses from a Nd:YAG laser to ablate dental tissues. Shephard *et al.* [21] delivered the laser beam from a Q-switched Nd:YAG laser through a single mode hollow core photonic band gap (PBG) fiber to conduct micromachining of metal sheets. However, so far no studies have been reported on deep micro-drilling via a single mode hollow core fiber transmitted femtosecond pulses.

As one type of ultra-short pulsed lasers, femtosecond laser has been intensively studied recently and achieved various degrees of success in micromachining applications [22-24]. Compared with nanosecond and picosecond lasers, femtosecond laser is regarded as a potentially ideal tool for precision micromachining. It deposits energy into the material in a very short time, thus resulting in a very small heat affected zone (HAZ) and minimal energy loss into the bulk material [25]. In contrast, nanosecond and picosecond lasers create a relatively large layer of melted material, some of which is not removed but resolidifies around the hole to form a recast layer, spatters or burrs [26-29].

In this study, percussion micro-drilling using fs laser pulses delivered through a single mode hollow core glass fiber is conducted. The sample material is stainless steel (type 303). The main objective of this study is to determine how the operating parameters affect the laser-fiber coupling efficiency and the ablation rate in micro-drilling of the stainless steel. In the following, the fs laser micro-drilling experimental setup is first introduced in Section 3.3. Then, the laser-fiber coupling efficiency (Section 3.4) and ablation rate (Section 3.5) are investigated. Finally, the main conclusions from this study are drawn in Section 3.6.

3.3. Experimental Setup

The femtosecond laser system consists of a Ti:Sapphire Coherent Legend Elite Duo chirped pulse amplifier (CPA) that operates at 1 kHz, seeded by a Rainbow oscillator. The laser beam delivered from this system has a center wavelength of 800 nm, repetition rate of 1 kHz, maximum pulse energy of 6 mJ, beam diameter of 10 mm, and beam M^2 factor of 1.33. The delivered laser beam is focused by a focusing lens and then coupled into the hollow core borosilicate glass fiber mounted on two independent alignment stages. The sample is fixed on a micropositioning stage which is controlled by a computer to move in the *x*, *y* and *z* directions. A fast shutter is used to select the number of pulses. A neutral density filter is used to adjust the pulse energy into the fiber. The pulse energy and the pulse duration are measured using a power meter and an autocorrelator, respectively. The focus spot is measured with a CCD camera. A quarter-wave plate is used to generate a circularly polarized beam. The laser pulses passing through the drilled hole are detected with a photodiode and the corresponding ablation time is recorded by the computer. In addition, a nitrogen gas jet is used to blow away the generated debris from micro-drilling, thus protecting the fiber end.

3.4. Investigation on Laser-Fiber Coupling Efficiency

One function of the hollow core fiber in micro-drilling is to transmit the laser pulses to the target surface, and the fiber can also act as a spatial filter to improve the laser beam quality. It is found that coupling between the laser beam and the hollow core fiber is extremely important in micro-drilling and to some extent determines the quality of micro-holes. It should be mentioned that in this study, all the experiments are conducted in air. The pulse repetition rate and the fiber length are fixed at 1 kHz and 20 mm, respectively.

For laser-fiber coupling, the coupling efficiency is found to vary at different coupling positions. Furthermore, the coupling position for the maximum coupling efficiency is strongly related to air breakdown. Without air breakdown, the best coupling position is at the laser focus point. Once air breakdown occurs, the best position moves away due to beam defocusing.

Fig. 3-1 shows the variations of coupling efficiency and output pulse energy from the fiber when the input pulse energy changes from 0.17 to 3.65 mJ. The following parameters are fixed: pulse duration τ=400 fs, focal length L=700 mm and fiber inner diameter r=150 μm. Initially, as the input pulse energy increases from 0.1 to 1.32 mJ (Zone A), the output pulse energy increase proportionally and the coupling efficiency is almost constant at around 70%. From 1.32 to 2.56 mJ (Zone B), however, the coupling efficiency starts to drop gradually. This is because the peak intensities at these pulse energies have reached the air breakdown threshold ($\sim 10^{14}$ W/cm^2) [30], which results in air ionization and the loss of pulse energy. Once the fiber is filled with the maximum pulse energy after 2.56 mJ (Zone C), the output energy from the fiber end no longer increases and the coupling efficiency thereby continues to decrease.

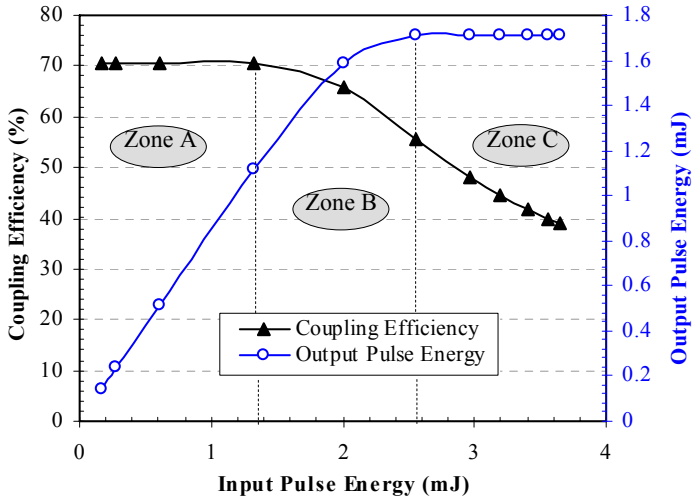

Figure 3-1 Effect of pulse energy on coupling efficiency

Fig. 3-2 shows the variations of coupling efficiency with pulse energy for different pulse durations: 50, 200, 400 and 600 fs. The input pulse energy varies from 0.17 to 3.65 mJ and all the other parameters are fixed: fiber inner diameter r=150 μm and focal length L=700 mm. It can be seen that the coupling efficiencies for all four durations are almost the same before air breakdown happens, and a shorter duration leads to smaller pulse energy. In this situation, no energy is lost except the coupling loss. Once air breakdown happens, it can be seen that the coupling becomes less efficient for shorter pulses.

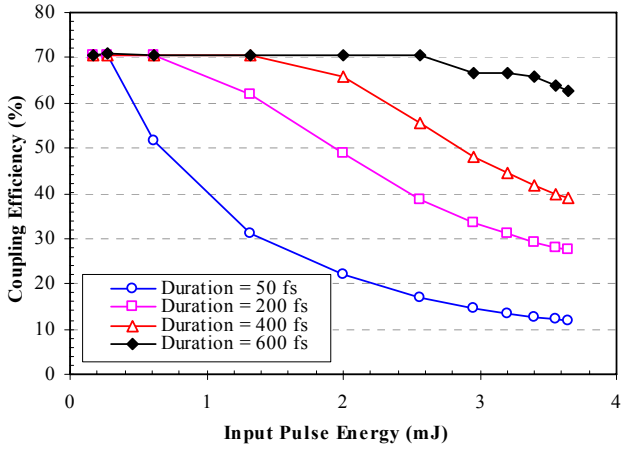

Figure 3-2 Effect of pulse duration on coupling efficiency

Fig. 3-3 shows the variations of the coupling efficiency with pulse energy for different focal lengths: 500, 700 and 1000 mm. The fixed parameters are: pulse energy E=0.3 mJ, pulse duration τ=400 fs and fiber inner diameter r=150 μm. The laser spot sizes for the three focal lengths (500, 700 and 1000 mm) measured with the CCD camera are 66, 91 and 131 μm, respectively, and the corresponding divergence angles are 0.8, 0.65 and 0.58 deg.

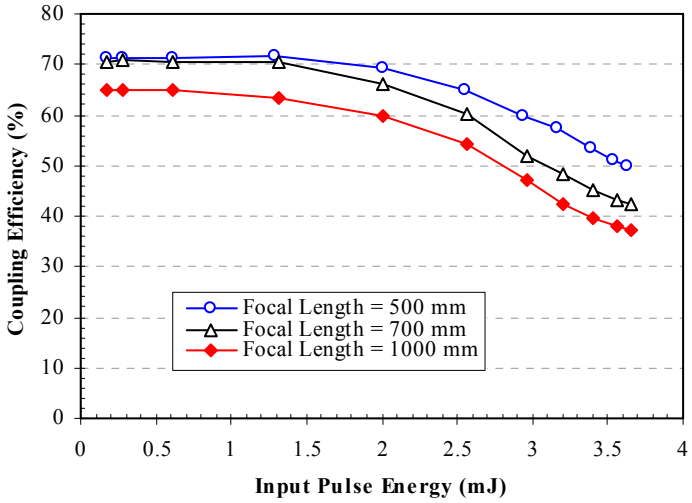

Figure 3-3 Effect of focal length on coupling efficiency

For the focal lengths of 500, 700 and 1000 mm, the ratio between the laser spot size and the fiber inner diameter is 0.44, 0.61 and 0.87, respectively. Abrams [31] pointed out that the ratio for the maximum coupling efficiency is 0.64 from the theoretical calculation. As shown in Fig. 3.3, however, the maximum coupling efficiency does not occur for the focal length of 700 mm, although the ratio is very close to the theoretical value of 0.64. One probable reason is that the theoretical value is calculated based on some assumptions like perfect Gaussian beam, infinitely long fiber, exactly circular beam spot and inner hole of the fiber, etc. These assumptions, however, cannot be realized in the actual laser-fiber coupling setup. Another reason

is that a small coupling ratio is prone to induce high-order beam modes that may enhance energy transmission.

3.5. Parametric Study on Ablation Rate

From the viewpoint of micromachining, high ablation rate means that the laser pulse energy is efficiently applied to material removal. In order to better understand the effects of the operating parameters on the ablation rate, a parametric study is conducted. Table 1 lists the key operating parameters considered in this study: pulse energy, pulse duration, sample thickness, focal length of the focusing lens, and sample-fiber distance (distance between the sample surface and the fiber end). The pulse number engaged in micro-drilling is counted from the opening of the shutter to the first pulse piercing the sample detected by the photodiode. In the parametric study, when one parameter is varied, the others are all fixed at the reference values indicated in bold italic style in Table 3-1.

Table 3-1 Key parameters considered in micro-drilling

Output Pulse Energy (E, mJ)	Pulse Duration (τ, fs)	Sample Thickness (t, mm)	Focal Length (L, mm)	Sample-Fiber Distance (d, mm)
0.5	200			***2***
0.8	300	0.6	500	7
1.1	***400***	***0.9***	***700***	12
1.4	500	1.2	1000	17
1.7	600			22

3.5.1 Pulse Energy

Fig. 3-4 shows the variations of the average ablation rate with the output pulse energy from 0.5 to 1.7 mJ. The fixed parameters are: pulse duration τ=400 fs, sample thickness t=0.9 mm, focal length L=700 mm, and sample-fiber distance d=2 mm.

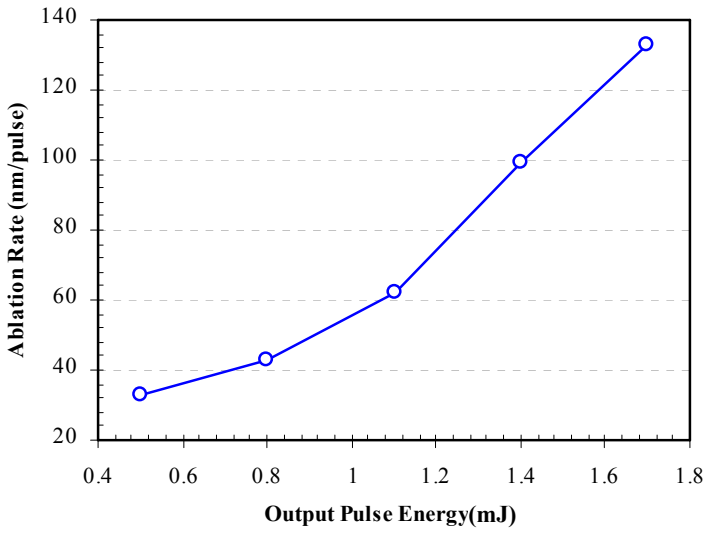

Figure 3-4 Effect of output pulse energy on ablation rate

It can be seen that higher pulse energy can cause a higher average ablation rate. Moreover, higher pulse energy can lead to a larger micro-hole size. As shown in Fig. 3-5, two microholes of 140 and 155 μm in diameter were produced with pulse energies of 0.5 and 1.7 mJ, respectively. It is also noted that the heat affected zone around the micro-holes (indicated by the arrows in Fig. 3-5) is small. Actually, for the laser beam with a Gaussian profile, most of the energy is concentrated in the central area of the micro-hole. With the pulse energy increasing, the energy at the edge also increases, which causes the micro-hole size to enlarge and more material to be removed around the edge of the micro-hole. The roundness of the holes is very good, which is attributed to the spatial filtering effect of the hollow core fiber.

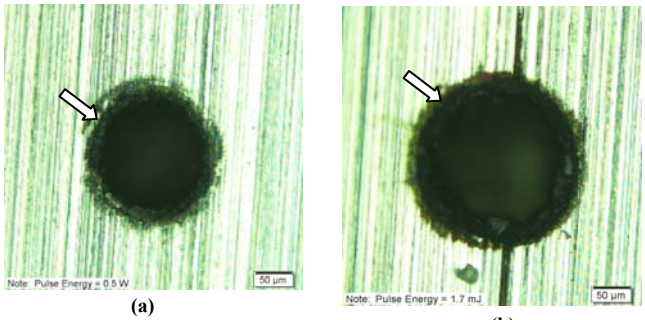

Figure 3-5 Comparison of the microholes for (a) pulse energy E=0.5 mJ and (b) pulse energy E=1.7 mJ

3.5.2 Pulse Duration

Fig. 3-6 shows the variations of the average ablation rate with the pulse duration from 200 to 600 fs. The following parameters are fixed at the reference values: pulse energy E=0.8 mJ, sample thickness t=0.9 mm, focal length L=700 mm, and sample-fiber distance d=2 mm.

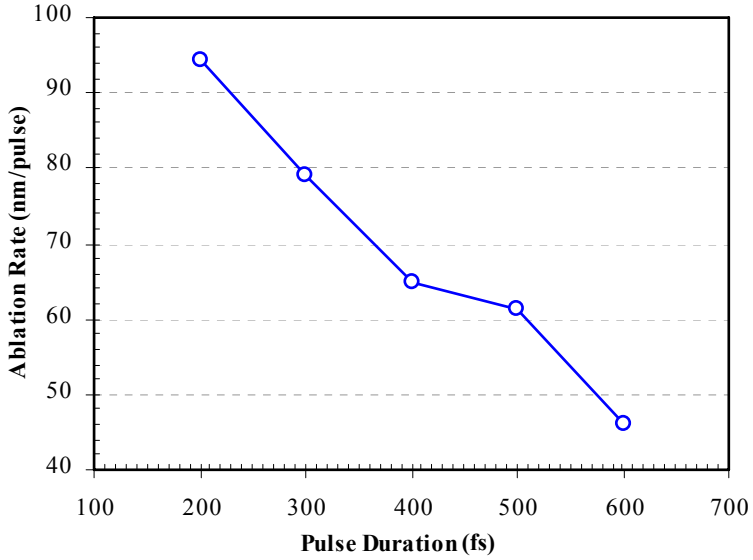

Figure 3-6 Effect of pulse duration on ablation rate

It can be seen that with the pulse duration increasing from 200 to 600 fs, the average ablation rate decreases. Actually, the pulse duration indicates the time during which optical

energy is delivered to the target and absorbed by the sample. For fixed pulse energy, a shorter pulse duration means a higher laser intensity. A higher intensity laser pulse could bring high temperature deeper into the material after thermalization, thus inducing a higher ablation rate. In addition, a long pulse may also suffer from energy loss due to reflections of the laser irradiation by the dense plasma produced by the leading edge of the pulse.

3.5.3 Sample Thickness

Fig. 3-7 depicts the variations of the average ablation rate with different sample thicknesses: 0.6, 0.9 and 1.2 mm. The other parameters are fixed at the reference values: pulse energy E=0.8 mJ, pulse duration τ=400 fs, focal length L=700 mm, and sample-fiber distance d=2 mm.

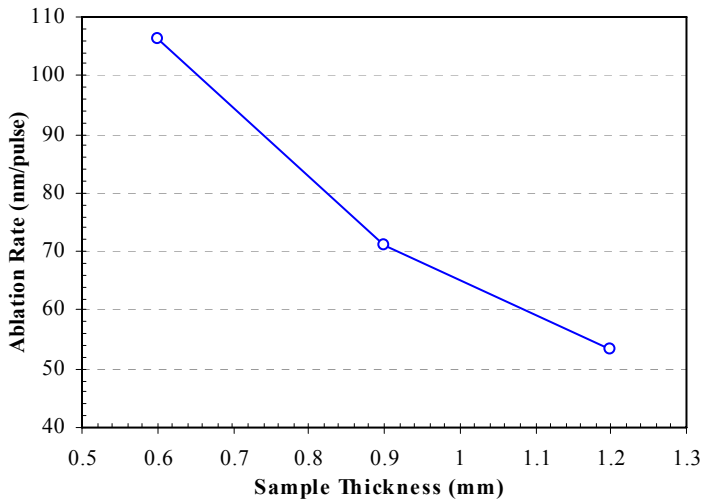

Figure 3-7 Effect of sample thickness on ablation rate

As shown in Fig. 3-7, the average ablation rate decreases with the sample thickness. For a series of laser pulses used in percussion micro-drilling, it is generally true that more material can be ablated by the beginning pulses than the trailing ones. The reason is that, as the micro-hole goes deeper, more ablated particles will stay inside the micro-hole which partially scatter the

laser radiation from the following pulses and thus attenuate the laser radiation engaged in material removal, although there is little effect of plasma shielding for femtosecond pulses. Note that the divergence of the laser beam can also reduce the ablation rate because of a decrease of the beam intensity as the beam propagates deeper into the hole.

3.5.4 Focal Length of the Focusing Lens

Fig. 3-8 shows the variations of the average ablation rate with the focal length of 500, 700 and 1000 mm. The other parameters are fixed at the reference values: pulse energy E=0.8 mJ, pulse duration τ=400 fs, sample thickness t=0.9 mm, and sample-fiber distance d=2 mm.

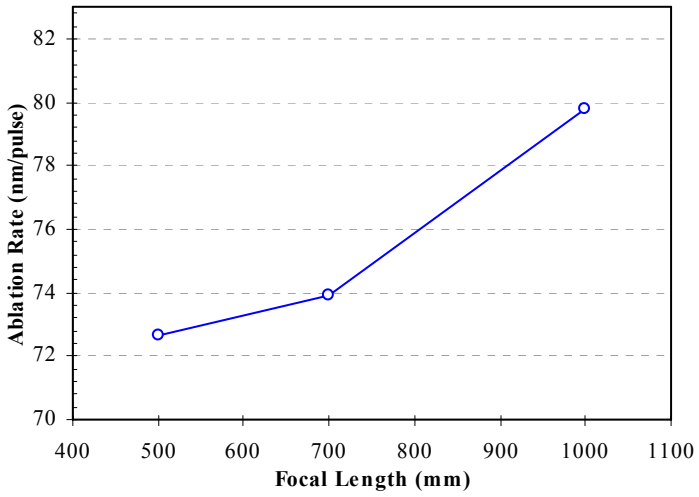

Figure 3-8 Effect of focal length of the focusing lens on ablation rate

Fig. 3-8 indicates that the average ablation rate increases as the focal length changes from 500 to 1000 mm. This is attributed to the improvement in the beam quality as the focal length increases. It is found from our experiments that the laser beam for the focal length of 1000 mm has the best beam mode. In general, the laser intensity distribution after the hollow core fiber takes the shape of a strong central core surrounded by a few weak rings. It is very likely that the

central beam for the 1000 mm focal length has the strongest intensity, thus resulting in the highest ablation rate.

3.5.5 Sample-Fiber Distance

Fig. 3-9 shows the variations of the average ablation rate with the sample-fiber distance from 2 to 22 mm. the other parameters are fixed at the reference values: pulse energy E=0.8 mJ, pulse duration τ=400 fs, sample thickness t=0.9 mm, and focal length L=700 mm.

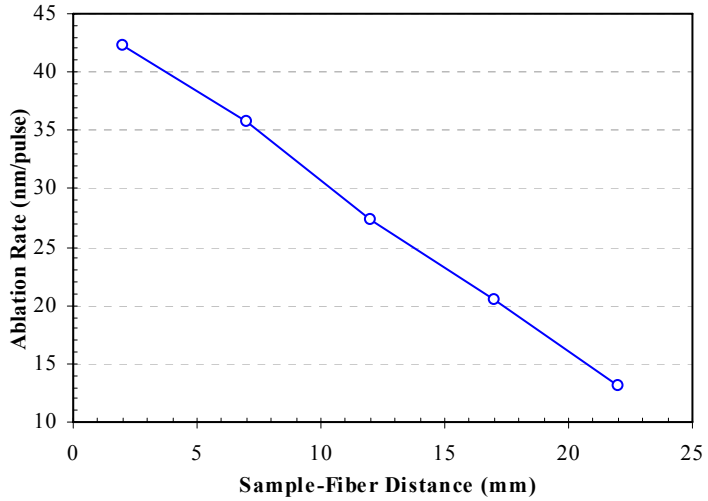

Figure 3-9 Effect of sample-fiber distance on ablation rate

It can be seen that the average ablation rate decreases linearly as the sample-fiber distance increases. It is also noted that the micro-hole enlarges with the distance increasing. Fig. 3-10 illustrates two micro-holes produced with the current operating parameters. The sample-fiber distances are 2 and 22 mm, and the corresponding micro-hole sizes are 152 and 215 μm, respectively. This is attributed to the divergence of the laser beam. It is suggested that the size of the micro-hole can be adjusted through the sample-fiber distance.

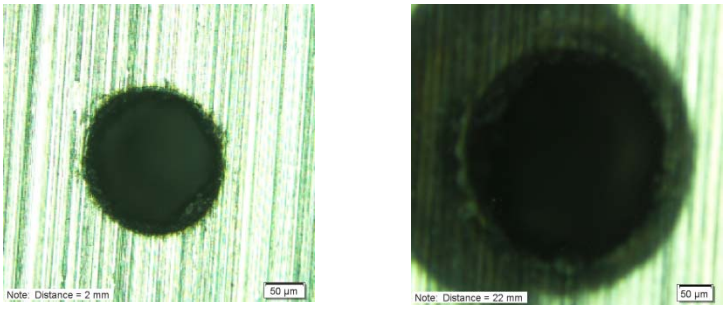

(a) **(b)**

Figure 3-10 Comparison of the microholes for (a) sample-fiber distance = 2mm and (b) sample-fiber distance = 22 mm

The above parametric study reveals that the operating parameters strongly affect the average ablation rate in micro-drilling. They also influence the geometric quality of the micro-hole. Fig. 3-11 shows a typical micro-hole achievable in this study. The micro-hole was produced in air with the following operating parameters: pulse energy E=1.35 mJ, pulse duration τ=400 fs, focal length L=700 mm, fiber inner diameter r=150 µm, and sample-fiber distance d=2 mm. The sizes of the entry and exit holes are 152 and 120 µm, respectively, and the ratio is 1:0.8. It is also observed that both the entry and exit hole have a good roundness, there are no recast layer around the micro-hole and no severe damage on the top surface induced by laser heating.

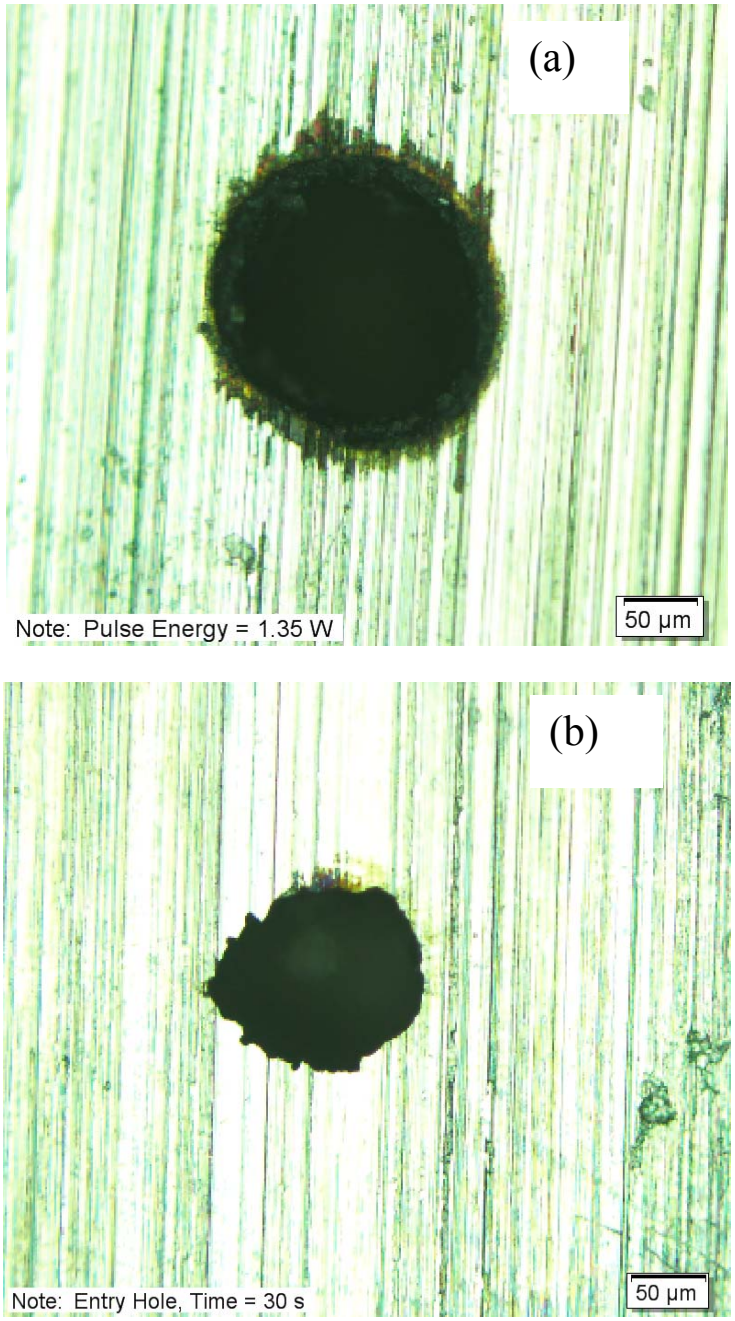

Figure 3-11 A microhole (~1 mm deep) created in the stainless steel (a) entry side and (b) exit side.

3.6. Conclusions

The laser-fiber coupling efficiency is found to be strongly associated with air breakdown. Outside the breakdown zone, the coupling efficiency almost remains constant and then gradually decreases within the breakdown zone. Pulse duration does not change the coupling efficiency, but can extend the range of pulse energy without the occurrence of air breakdown. Although a very small ratio between the beam spot size and the fiber inner diameter may cause a high coupling efficiency, a poor beam mode is usually obtained. In contrast, a very large coupling ratio will lead to a low coupling efficiency.

It is feasible to drill deep micro-holes using fs laser pulses delivered through a hollow core fiber. The fiber acts as a spatial filter to improve the laser beam profile. The parametric study on the ablation rate indicates that with a given micro-hole size and the sample thickness, a high ablation rate can be obtained with high pulse energy, short pulse duration, and a long focal length. However, optimization of the operating conditions is needed to obtain a maximum ablation rate while meeting the quality requirements for the micro-holes such as size, roundness and cylindricity.

3.7 Acknowledgments

Financial support of this work by the National Science Foundation (under Grant No. CMMI-0826184 and CMMI-0826015) and the DoD Army Research Office (under the Agreement Number W911NF-07-1-0475) is gratefully acknowledged.

3.8 References

[1] Foy, Kevin, Wei, Zhi, Matsumura, Takashi, Huang, Yong, 2009. Effect of tilt angle on cutting regime transition in glass micromilling. International Journal of Machine Tools and Manufacture. 49(3-4), 315-324.

[2] Jun, Martin B.G., Bourne, Keith, DeVor, Richard E., Kapoor, Shiv G., 2007. Estimation of effective error parameters in high-speed micro-endmilling. International Journal of Machine Tools and Manufacture. 47(9), 1449-1454.

[3] Richter, A., 2007. Hole-down: options for and considerations for micro-holemaking. Cutting Tool Engineering. 59(2), S2-7.

[4] Kao, Chen-Chun, Shih, Albert J., Miller, Scott F., 2008. Fuzzy logic control of microhole electrical discharge machining. Journal of Manufacturing Science and Engineering, Transactions of the ASME. 130(6), 0645021-0645026.

[5] Ahn, Y., Dae-Jin Kim, Seoung-Hwan Lee, and Yong-Kweon Kim, 2006. voltage pulse frequency and duty ratio effects in an electrochemical discharge microdrilling process of pyrex glass. International Journal of Machine Tools & Manufacture. 46(10), 1064-7.

[6] Torng, Chau-Chen, Huang, Chikong, Chang, Hsien-Ming, 2009. Process control for aerospace chemical milling process. International Journal of Manufacturing Technology and Management. 18(3), 308-318

[7] Hayes, Donald J., Wallace, David B., 1989. Overview of small holes. Technical Paper - Society of Manufacturing Engineers. MS89-814-1-11.

[8] Ready, John F. (Editor), 2001. LIA Handbook of Laser Materials Processing, Laser Institute of America, magnolia Publishing, Inc.

[9] Howitt, D.G., Chen, S.J., Gierhart, B.C., Smith, R.L., Collins, S.D., 2008. The electron beam hole drilling of silicon nitride thin films. Journal of Applied Physics, 103(2).

[10] Martelli, Cicero, Olivero, Paolo, Canning, John, Groothoff, Nathaniel, Gibson, Brant, Huntington, Shane, 2007. Micromachining structured optical fibers using focused ion beam milling. Optics Letters. 32(11), 1575-1577.

[11] Joo, Byung-Yun, Rhim, Sung-Han, Oh, Soo-Ik, 2005. Micro-hole fabrication by mechanical punching process. Journal of Materials Processing Technology. 170(3), 593-601.

[12] Durante, Massimo, Langella, Antonio, 2009. Bearing behavior of drilled and molded-in holes. Applied Composite Materials. 16(5), 297-306.

[13] Abeln, T., Radtke, J., and Dausinger, F., 1999. High precision drilling with short-pulsed solid-state lasers. Proc. Laser Microfabrication Conf. ICALEO '99, San Diego, USA, 195-203.

[14] Jones, Marshall G., and Georgalas, Gregory, 1984. Flexible beam delivery for material processing laser power through a fiber optic cable. LIA (Laser Institute of America). 38, 149-153.

[15] De Snaijer, Ad, Verdaasdonk, Rudolf M., Grimbergen, Matthijs C., Van Swol, and Christiaan F.P., 1998. Design and realization of a fiber delivery system for the continuous wave and pulsed CO2 laser. Proceedings of SPIE - The International Society for Optical Engineering. 3262, 108-118.

[16] Watanabe, Takehiro, Kobayashi, Hiroyuki, Suzuki, Keiji, and Beppu, Seiji, 2000. Cutting of thick steel with fiber-delivered high power Nd:YAG laser beam. Proceedings of SPIE - The International Society for Optical Engineering. 3888, 635-642.

[17] Quintero, F., Pou, J., Lusquinos, F., Larosi, M., Soto, R., and Perez-Amor, M., 2001. Cutting of ceramic plates by optical fiber guided Nd:YAG laser. Journal of Laser Applications. 13(2), 84-8.

[18] Shen, Xinwei and Lei, Shuting, 2009. Thermal modeling and experimental investigation for laser assisted milling of silicon nitride ceramics. Journal of Manufacturing Science and Engineering, Transactions of the ASME. 131, 051007-1-10.

[19] Dekel, B., Inberg, A., Croitoru, N., Shalem, S., and Katzir, A., 2000. Hollow glass waveguides and silver halide fibers as scanning elements for CO2 laser marking systems. Optical Engineering. 39(5), 1384-1390.

[20] Konorov, S.O., Mitrokhin, V.P., Fedotov, A.B., Sidorov-Biryukov, D.A., Beloglazov, V.I., Skibina, N.B., Shcherbakov, A.V., Wintner, E., Scalora, M., Zheltikov, A.M., 2004. Laser ablation of dental tissues with picosecond pulses of 1.06-μm radiation transmitted through a hollow-core photonic-crystal fiber. Applied Optics. 43(11), 2251-6.

[21] Shephard, J.D., Couny, F., Russell, P.St.J., Jones, J.D.C., Knight, J.C., and Hand, D.P., 2005. Improved hollow-core photonic crystal fiber design for delivery of nanosecond pulses in laser micromachining applications. 44(21), 4582-8.

[22] Witte, Reiner, Moser, Tobias, Liebers, Rene, and Holtz, Ronald, 2008. Laser micro-drilling with nanoseconds: parametrical influences and results. Proceedings of SPIE - The International Society for Optical Engineering, 7022.

[23] Raciukaitis, Gediminas, Brikas, Marijus, 2004. Micro-machining of silicon and glass with picosecond lasers. Proceedings of SPIE - The International Society for Optical Engineering. 5662, 717-721.

[24] Chichkov, B.N., Momma, C., Nolte, S., von Alvensleben, F., Tuennermann, A., 1996. Femtosecond, picosecond and nanosecond laser ablation of solids. Applied Physics A: Materials Science and Processing. 63(2), 109-115.

[25] Craig, Bruce, 1998. Ultrafast pulses promise better processing of fine structures. Laser Focus World. 34(9), 79.

[26] Chien, Wen-Tung, Hou, Shiann-Chin, 2007. Investigating the recast layer formed during the laser trepan drilling of inconel 718 using the taguchi method. International Journal of Advanced Manufacturing Technology. 33(3-4), 308-316.

[27] Hoyle, R., 2007. Picosecond laser machining. Medical Device Technology, May/June, www.devicelink.com/mdt/archive/07/05/002.html.

[28] Knowles, M., Kearsley, A., Karnakis, D., 2007. Laser micromachining expands as technology develops. Laser Focus World. 43(6), 127-32.

[29] Quintana, I., Dobrev, T., Aranzabe, A., Lalev, G., Dimov, S., 2009. Investigation of amorphous and crystalline Ni alloys response to machining with micro-second and pico-second lasers. Applied Surface Science. 255(13-14), 6641-6.

[30] Shah, L., Tawney, J., Richardson, M., and Richardson, K., 2004. Self-focusing during femtosecond micromachining of silicate glasses. IEEE Journal of Quantum Electronics. 40(1), 57-67.

[31] Abrams, R.L., 1972. Coupling losses in hollow waveguide laser resonators. IEEE Journal of Quantum Electronics. QE-8(11), 838-43.

Chapter 4 - Femtosecond laser ablation of indium tin-oxide narrow grooves for thin film solar cells

Published: Optics & Laser Technology 45 (2013) 395–401

Author's Names: Qiumei Bian,[1] Xiaoming Yu,[1] Baozhen Zhao,[2] Zenghu Chang,[2,3] Shuting Lei[1]

Author's Affiliation:

1 Department of Industrial and Manufacturing Systems Engineering, Kansas State University, KS 665062

2. Department of Physics, Kansas State University, 66502

3. The College of Optics & Photonics, University of Central Florida Orlando, FL 32816

4.1 Abstract

Finding ways to scribe indium-tin oxide (ITO) coating plays an important role in the fabrication and assembly of thin film solar cells. Using femtosecond (fs) laser, we selectively removed the ITO thin films with the thickness of 120 ~160 nm on glass substrates. In particular, we studied the effect of laser pulse duration, laser fluence and laser scanning speed on the ablation of ITO. The single pulse ablation thresholds at various pulse durations were determined to ablate ITO thin films. Clean removal of the ITO layer was observed when the laser fluence was above the threshold of 0.30 J/cm^2. Furthermore, the morphologies and microstructure of fabricated grooves were characterized using scanning electron microscope and KLA Tencor P-16 Profiler. The groove width down to 3 micrometers with 10 nm groove ridge can be achieved by the ablation of femtosecond laser pulses with 220 nJ of energy. The femtosecond laser therefore provides a unique scheme to ablate indium tin oxide layer for the fabrication of thin film solar cells.

Keywords*:* ablation; femtosecond laser; indium tin oxide; thin film

4.2. Introduction

Currently indium tin oxide (ITO) is widely employed as a transparent conductor for the fabrication of thin film solar cells [1, 2]. The ITO layer in thin film solar cell modules has a significant impact on the power conversion efficiency[3, 4]. In order to reduce the resistive losses and lost active area of solar cell, high resolution-patterning of ITO thin films is required in the formation of interconnect line and assembly of thin film solar cells[5]. Various techniques have been developed to pattern ITO electrodes with well-defined edges and electrically insulated grooves between the conductor lines for thin film solar cells. Examples include photolithography with wet etching in acidic solutions[6]. However, this method requires multiple process steps and expensive equipment as well as toxic chemicals. Also, the grooves with diffusion edges can be observed due to under or over etching. Therefore, it is necessary to develop a nonlithographic or direct patterning strategy to fabricate fine structures with well-defined edges on ITO electrodes.

Laser ablation is the removal of materials from a substrate by direct absorption of laser energy, which can produce the desired combination of narrow and clean patterning because of their advantage in localized heating and material removal [7-9]. In general, ultra-short pulsed laser ablation offers small thermally induced defects in the remaining material, which are often difficult to avoid with longer laser pulses [10]. Therefore, femtosecond (fs) and picosecond (ps) lasers have been utilized to scribe ITO for the fabrication of solar cells [11-13]. Recent investigations on ps laser scribing of ITO demonstrated that the material damage threshold depends on laser repetition rate and wavelength, as well as other system parameters. It was also found that the groove edges were thermally affected by use of the 532 nm radiation, and the lowest ridge height of 20 nm was achieved[14]. Compared with ps laser pulses, fs laser can induce nonthermal structural changes driven by electronic excitation [7]. Femtosecond laser has

been used as the precision material remove tool in solar cell fabrication research due to small thermally induced defects in the remaining material [15-17]. Ashkenasi *et al.* reported a theoretical and experimental investigation on fs laser ablation and concluded that a further improvement in quality can be obtained by using fs pulses in the IR spectrum[18]. Choi *et al.*[16], demonstrated fs laser ablation of ITO films with various pulse repetition rates and laser fluence. It was shown that the groove ridge is as high as 20 nm with the groove depth of 150 nm and the width of 20 mm. However, there are no reports attempting to cut narrow grooves with width of only a few microns. Also, the effect of fs laser pulse duration on the ablation of ITO thin films has not been studied.

In this paper, the roles of laser pulse duration, laser fluence and laser scanning speed are investigated in fs laser patterning of ITO thin films in the regime of narrow grooves of a few microns wide. The potential improvement that such high quality narrow grooves could bring in the electrical conversion efficiency is estimated.

4.3. Experimental procedure

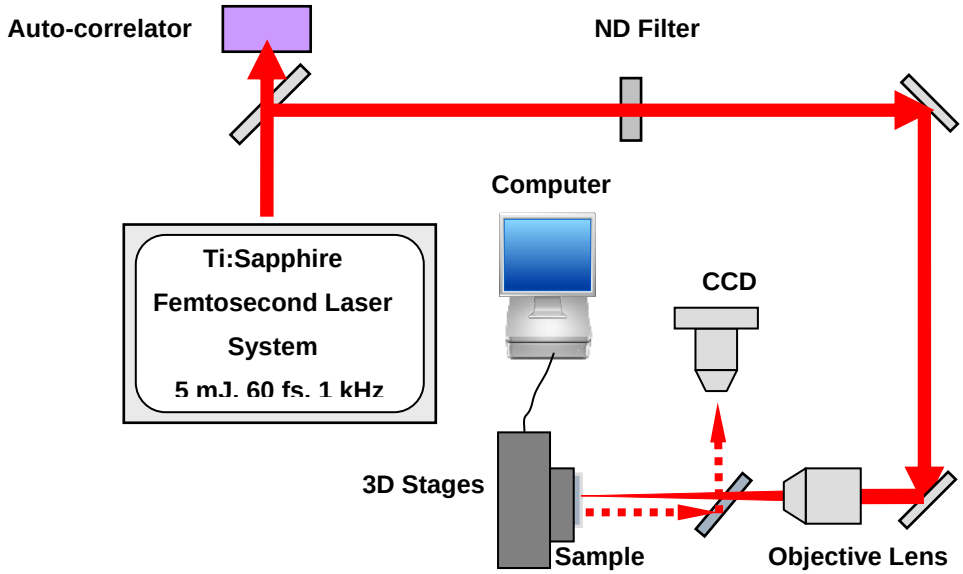

Figure 4-1 Schematic of experimental setup

Fig. 4-1 shows the experimental setup schematically. The fs laser system is used in this study, which consists of a commercially available Ti:Sapphire chirped pulse amplifier (CPA) that operates at 1 kHz, seeded by a Rainbow oscillator. The laser beam delivered from this system has center wavelength of 800 nm, repetition rate of 1 kHz, and maximum pulse energy of 5 mJ [19]. The pulse duration is ~60 fs right after the amplifier measured by the autocorrelator and can be adjusted by varying the gratings distance of the compressor. A neutral density filter is applied to adjust the pulse energy. The pulse energy is measured with a power meter. The laser beam is focused by a lens of 150 mm focal length for single shot damage threshold investigation. An objective lens with 0.3 NA is used for laser grooving experiments. The laser beam is focused on the sample surface. The sample is fixed on a micro-positioning stage controlled by a computer to move in the *x*, *y* and *z* directions.

Commercially available ITO coated glass (Delta Technologies, LTD) with sheet resistance of 5~15 ohms is used in the experiments. The soda lime float glass is coated with a primary smoothening layer of SiO_2, and the layer of indium-tin oxide is vacuum-deposited on it. The thickness of the ITO layer is 120~160 nm.

In this study, the following laser ablation experiments are conducted: (1) to find the material damage threshold and single shot ablation rate at different pulse durations; (2) to scribe the ITO thin film and investigate how the operating parameters such as pulse duration, pulse fluence and scanning speed affect the groove geometry and surface morphology. Grooves are cut in ITO samples under various conditions, namely variable pulse duration, pulse fluence and laser scanning speed.

To analyse the morphology of the grooves, a KLA Tencor P-16 Profiler and scanning electron microscope (SEM) are used to allow visual comparison in term of quality and structure in both 2D and 3D.The groove electrical insulation is examined by a multimeter.

4.4. Results and discussion

4.4.1 Single pulse ablation morphology and material damage threshold

In order to determine the damage threshold of ITO, we investigated and observed the morphology and depth of crater under single fs laser shot. A typical profile image and two-dimensional cross-section profile of a crater made at fluence of 2 J/cm^2 with 150 mm focal length lens and 60 fs pulse duration are shown in Fig. 4-2a and 2b, respectively. From the profile image, we can observe the crater ablated by the Gaussian beam, and the round shape of the crater confirms the good beam quality. The depth of the crater is around 60 nm and the diameter is about 65 mm at the fluence of 2 J/cm^2. Fig. 4-2c shows the ablation depth at 60 fs pulse duration

as a function of laser fluence based on single-shot experiments. The crater diameter and depth increases as the laser fluence increases. The nonlinear dependence of ablation depth with fluence is attributed to more efficient multi-photon ionization at higher peak intensities and plasma density increasing with the laser intensity rising [20]. Although the 800-nm single photons cannot meet ITO band gap energy requirements, the multiphoton absorption associated with the high intensity of fs pulse are responsible for bond breaking and subsequent emission of electrons and ions.

We studied the single pulse damage threshold of the ITO film by measuring the laser pulse energy which resulted in visible damage to the ITO film. Damage threshold is a characteristic dependent on the wavelength, pulse width and type of material. It is ideally defined as the laser fluence at which irreversible damage occurs in the material by removing a monolayer of material. It is actually determined by visual examination, ablation depth measurement, plasma radiation monitoring etc.

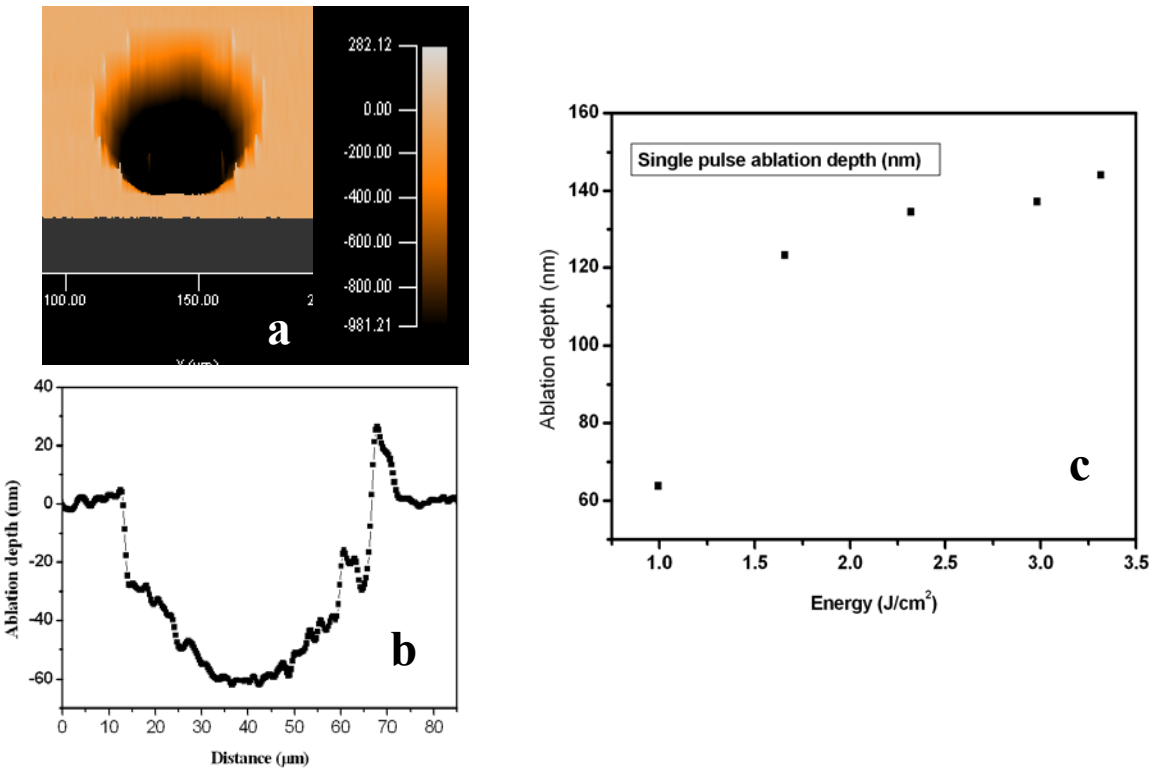

Figure 4-2 (a) Profile image of a crater; (b) cross-section profile of the crater; (c) the ablation depth as a function of laser fluence based on single-shot experiments

In this study the damage threshold was estimated by recording the diameter (D) and the depth of single-shot ablated craters using SEM and KLA Tencor P-16 Profiler and then using the following linear relationship between the square of the crater diameter and the logarithm of the laser pulse energy with the Gaussian profile laser beam[21]:

$$D^2 = 2w_0^{\,2} \ln\left(\frac{F_0}{F_{th}}\right) \tag{1}$$

where F_{th} = damage threshold, F_0 =applied laser fluence and $2w_o$ = Gaossian beam spot size. A plot of the square of damage diameter, D^2, against the logarithm of energy is made to obtain both the spot size (slope of line) and damage threshold (the extrapolation of D^2 to zero

value) (Fig. 4-3 a). The damage threshold at 60 fs is found to be 0.21 J/cm^2. The variations of the damage threshold with pulse duration are shown in Fig. 4-3 b. The damage threshold slightly increases with pulse duration in the sub-ps range, which agrees with the previous research on fs laser ablation of Cu and Al film and fs laser ablation of fused silica [22, 23]. It does not totally agree with the observation that the threshold fluence is independent of pulse duration based on the non-equilibrium mechanism of femtosecond laser ablation [20]. Any form of laser energy deposition related to nonlinear effects such as multi-photon ionization is more efficient at high peak intensities as a result of short pulse duration [18].

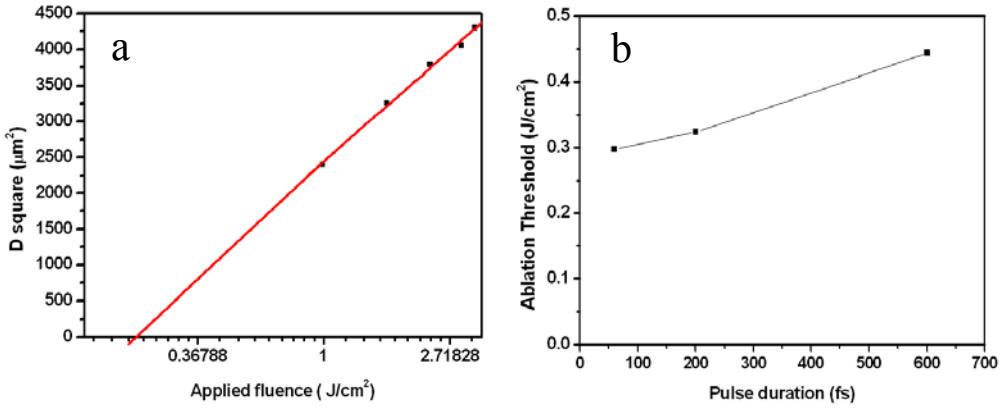

Figure 4-3 (a) Material damage threshold at 60 femtosecond (b) Material damage threshold varying with pulse duration

4.4.2 The influence of laser fluence on groove morphologies

The laser ablation conditions such as pulse energy and scanning speed should be well controlled in order to achieve required groove dimension and quality on the ITO thin film. In particular, the major processing parameter is laser fluence. The substrate can be damaged if the laser fluence is too high, while partial removal of ITO film may happen when the fluence is too low.

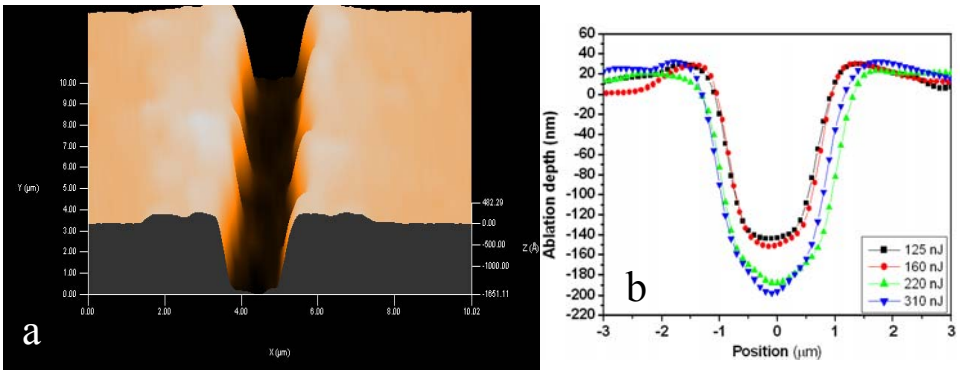

Figure 4-4 (a) A typical 3D profile of a groove ablated at the following conditions: pulse energy=160 nJ, scanning speed=0.4 mm/s, and pulse duration=60 fs; (b) 2D cross-section profiles of groove depth with laser energy from 125 to 310 nJ at the scanning speed of 0.4 mm/s.

Fig. 4-4a shows a 3D groove morphology, and Fig. 4-4b shows the cross-section profiles for different pulse energies. The laser beam was focused by a 30X microscope lens. From the Fig. 4-4b, we can observe that for the pulse energy from 125 to 310 nJ the groove depth ranges from 140 to 200 nm, the groove width varies from 2 to 3 μm and the ridge height on the edges lies in the range of 10 to 30 nm. With increasing pulse energy, the depth and width of grooves increase, as shown in Fig. 4-4b. The total amount of energy absorbed by the material increases with increasing pulse energy. The higher laser fluence intensifies the material removal process.

There are ridges on both sides of the grooves. Although heat affected zones have been found to be very small for fs laser pulses in comparison to nanosecond laser pulses in the low fluence regime [24], at high fluences (five times of damage threshold) thermal effects even occur in the femtosecond range and the groove ridges are the results of the thermal effect, which are formed by extruding the melted material by vapor pressure and also by spallation of the thin film layer from the substrate [20].

4.4.3 The influence of pulse duration on groove morphologies

The dependence of groove quality on pulse duration is also investigated. It is found that detailed structures of the ablated grooves depend strongly on the pulse duration. From the SEM images (Fig. 4-5a and 5b) and the 2D cross-section profiles, we find that the groove width decreases from 2.2 to 1.2 mm when tuning the pulse duration from 60 to 600 fs. Furthermore, the groove depth decreases from 130 nm to 80 nm when changing the pulse duration from 60 to 600 fs. When the pulse duration increases and the laser intensity decrease, both the groove width and depth decrease at the same fluence**.**

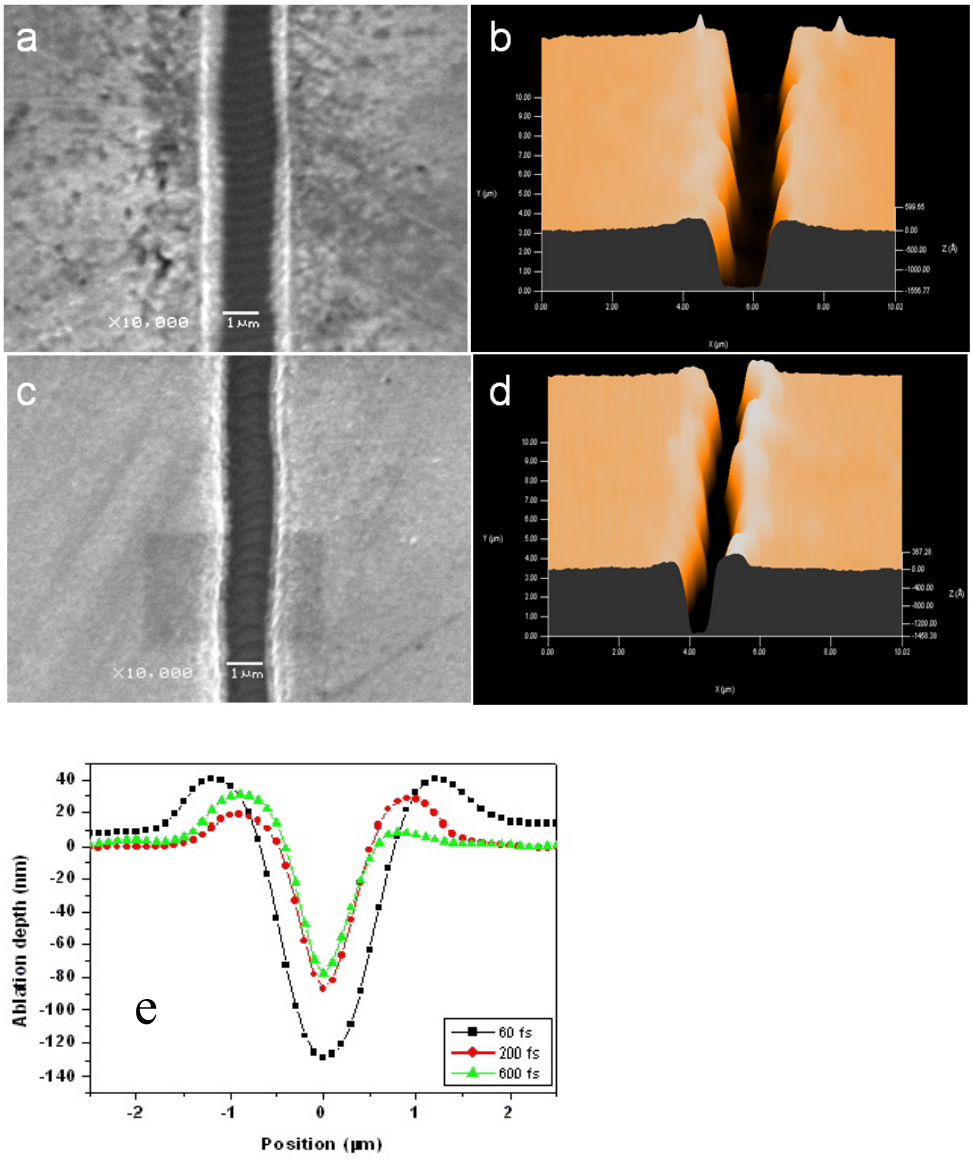

Figure 4-5 (a) SEM image of a groove at the pulse energy of 125 nJ, the scanning speed of 0.4 mm/s, and the pulse duration of 60 fs; (b) 3D profile of the corresponding groove; (c) SEM image of a groove at a longer pulse duration of 600 fs; (d) 3D profile of the corresponding groove;(e) 2D cross-section of the ablated grooves with pulse duration of 60, 200 and 600 fs.

The formation of these groove ridges is attributed to a surface tension gradient in the molten material near the rim of laser-irradiated spot, which might be resulted from the poor

thermal conductivity of the glass substrate. For fs laser pulses, thermal ablation process also occurs when laser ablation fall in the strong ablation regime with high laser fluence [18, 22]. The fs ablation of the ITO thin film in the high fluence mainly governed by thermal process should result in the formation of the ridges because of the high surface temperature of the thin film followed by laser irradiation. Some groove ridges with a height of 5 to 30 nm was formed at the groove rim as shown in Fig.4-5.

There also is a change in groove ridge height from 5 to 30 nm when the pulse duration varies from 600 to 60 fs. The threshold fluence at 60 fs is lower than that at 600 fs, therefore, at the same fluence level, the shorter the pulse duration, the less amount of energy deposited into the processed sample required to remove same amount of material. As a result, for laser pulse duration within the fs range, the groove ridge height, groove depth and groove width all increase with decreasing pulse duration at the same fluence level. Thus less pulse is required for the same groove width and depth with the pulse duration decreasing.

4.4.4 The influence of laser scanning speed on groove morphologies and microstructure

Laser scanning speed affects the groove morphologies and structure at the same energy density since the speed is related to the number of pulses absorbed by the material based on the equation N=RS/V, where N is the pulse number, R the pulse repetition rate, S the beam focal spot size and V the laser scanning speed[25].

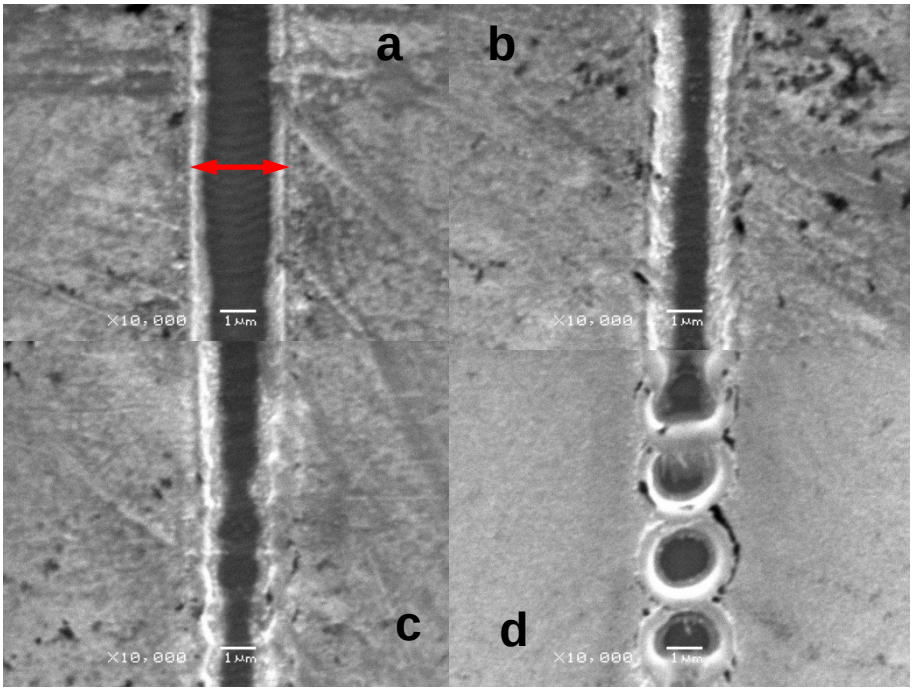

Figure 4-6 SEM images of the grooves ablated at the pulse duration of 60 fs, the pulse energy of 160 nJ, and the scanning speed of 0.4 mm/s (a), 0.8 mm/s (b), 1.2 mm/s (c), and 2 mm/s (d), respectively.

With fixed pulse energy, repetition rate and focal spot size, the scanning speed is the only parameter that can be varied in order to control the ablation depth. Ablation depth and width at various scanning speeds are shown in Figs. 4-6 and 4-7. At a low speed (0.4 mm/s), we can observe the groove with the width of 3 mm. At a higher speed (1.2 mm/s), the width decreases to 2 mm. In particular, at the speed of 2 mm/s, the ITO along the groove is only partially removed. Furthermore, with the speed decreasing at laser fluence well above the damage threshold, the groove depth increases as shown in Fig. 4-7 a,b,c,d,and e. In comparison with the groove at a high speed, the groove at a lower speed is wider and deeper due to the accumulation of the laser irradiation energy. The increase of the ablated depth with decreasing scanning speed is the result

of more beam overlap at lower speeds, causing more laser energy accumulation and deposition in the same spot in the ITO thin film[17]. Therefore, we can tune the scanning speed to control the groove depth within the ITO thickness.

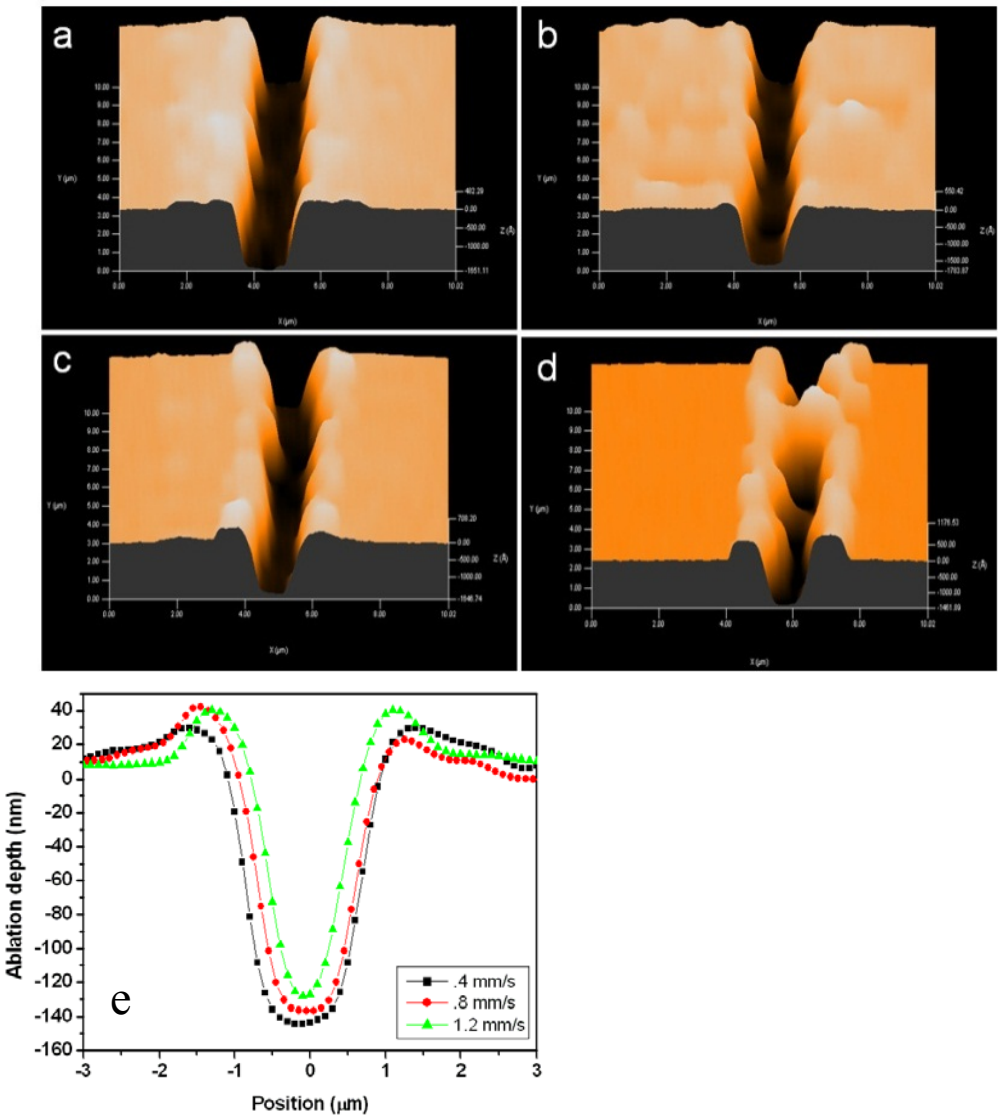

Figure 4-7 3D profile images of the grooves ablated at the pulse duration of 60 fs, the pulse energy of 160 nJ, and the scanning speed of 0.4 mm/s (a), 0.8 mm/s (b), 1.2 mm/s (c), and 2 mm/s (d), respectively; (e) groove cross-section profiles at various scanning speeds.

4.4.5 Elemental distribution and electrical resistance across a groove

The grooves are further investigated using the X-ray energy dispersive spectrometer because visual contrast does not reveal the chemical compositions. Fig. 4-8a shows the SEM image of an ablated groove with the width of 2.5 mm. The point-focused EDS profile from the surface of ITO shows intense In and Sn peaks with O from thin film and glass substrate and Si from glass substrate (Fig.4-8b). The line-scanning EDS profiles (Fig.4-8c) for In, Sn, O, and Si clearly show a dramatic decrease in the content of In and Sn and a corresponding increase in O and Si along the scanning path from ITO surface to the groove, indicating that the top ITO layer is evaporated and removed, and the glass substrate is exposed.

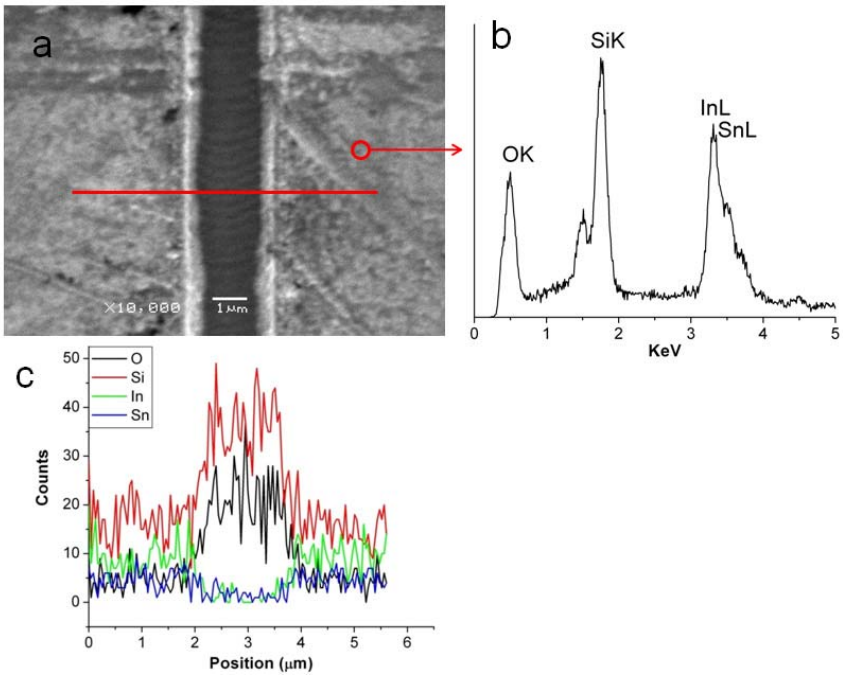

Figure 4-8 (a) SEM image of a typical groove ablated at the pulse energy of 160 nJ, the scanning speed of 0.4 mm/s, and the pulse duration of 60 fs; (b) A point-focused energy-dispersive X-ray spectroscopy (EDS) profile on ITO surface; (c) EDS line-scanning profile of a groove ablated in the ITO layer to expose the substrate.

The electrical resistance is measured to examine the groove quality in terms of electrical insulation. If the groove is not clean or with high ridges (comparable to the thickness of the absorber layer), local shunts and shortcuts may happen through the upper layers of the thin film solar cell, which can reduce the cell conversion efficiency. The groove is not totally electrically insulated as long as the In and Sn are left in the grooves such as shown in Fig. 4-7 d and we can measure the electrical resistance a few hundreds ohm. For the insulated grooves as shown in Fig. 4-7 a,b,c , the measured electrical resistance is infinity (out of the measurement range).

4.4.6 An example of high quality narrow grooves

By tuning the laser energy to 220 nJ and scanning speed to 1.2 mm/s, the high quality groove as shown in Fig. 4-9 is achieved. The groove width is 2 mm, the ridge height is small, and the ITO layer is totally removed with negligible damage to the glass substrate as shown in Fig. 4-9b, c. The elemental analysis in Fig.4-9d confirms that there are virtually no ITO residues left in the groove.

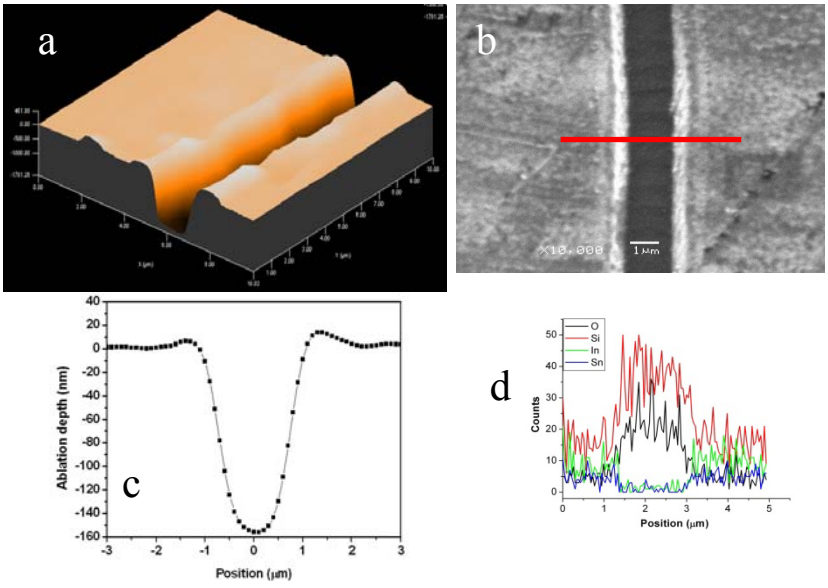

Figure 4-9 (a) 3D image of a high quality groove ablated at the pulse energy of 220 nJ, the scanning speed of 1.2 mm/s, and the pulse duration of 60 fs; (b) SEM image of the groove (c) 2D cross-section of the groove; (d) EDS line-scanning profile of the groove

The electrical resistance is examined using the multimeter and the result indicates that the groove is electrically insulated. High quality narrow grooves like the one shown in Fig. 4-9 could significantly increase the electrical conversion efficiency of thin film solar cells. For illustration purpose, if all three interconnection grooves can be made to a few microns in width using the commonly known three patterning processes (e.g. P1, P2, P3) in the monolithic solar modules, the dead area of the thin film solar cell can be decreased from 75~150 μm to 30~60 μm, which means that the cell active area will increase by 0.75~1.5% if the cell width is 6 mm [2].

Therefore, high quality narrow grooves are highly desirable in manufacturing thin film solar cells, and femtosecond laser is a promising tool for producing these grooves.

4.5. Conclusions

In summary, the femtosecond laser with various energy, pulse durations, and scanning speeds has been utilized to pattern ITO glass for thin film solar cells. The damage threshold of the ITO thin film is found to be 0.21~0.40 J/cm^2 when the pulse duration varies from 60 to 600 fs. The single pulse ablation rate increases with increasing laser fluence and decreasing pulse duration and scanning speed due to the accumulation of the laser irradiation energy. In addition, the groove width is insignificantly affected by pulse duration. The groove width decreases with increasing pulse duration. Also, we need to control the scanning speed to fully remove ITO without damaging the glass. We can tune the processing parameters to fabricate the required structure. For example, grooves without damaging the substrate can be made at the optimized parametric regime: the laser fluence is 2.2 J/cm^2~ 5 J/cm^2 and the scanning speed is 0.4~1.2

mm/s for a 1 kHz laser. With the selective laser energy and laser scanning speed, the high quality groove about 2 mm wide, 150 nm deep and 10 nm in ridge height is achieved, which shows the potential of fs laser for producing high density interconnects in thin film solar cells and thus significantly increasing the solar cell conversion efficiency.

4.6 Acknowledgements

Financial support of this work by the DoD Army Research Office under the Agreement Number W911NF-07-1-0475 is gratefully acknowledged.

4.7 Reference

[1] K.L. Chopra, P.D. Paulson, V. Dutta, Progress in Photovoltaics 12 (2004) 69-92.

[2] M.W. Rowell, M.D. McGehee, Energy & Environmental Science 4 (2010) 131-134.

[3] F. Kessler, D. Herrmann, M. Powalla, Thin Solid Films 480 (2005) 491-498.

[4] S. Wiedeman, R.G. Wendt, J.S. Britt, Module interconnects on flexible substrates, in: AIP, USA, 1999, pp. 17-22.

[5] A.G. Aberle, Thin Solid Films 517 (2009) 4706-4710.

[6] M. Hoheisel, A. Mitwalsky, C. Mrotzek, physica status solidi (a) 123 (1991) 461-472.

[7] S. Lee, D.F. Yang, S. Nikumb, Applied Surface Science 253 (2007) 4740-4747.

[8] M. Henry, P.M. Harrison, J. Wendland, Journal of Laser Micro Nanoengineering 2 (2007) 49-56.

[9] J. Kim, S. Na, Optics and Laser Technology 39 (2007) 1443-1448.

[10] J.J. Yang, R. Wang, W. Liu, Y. Sun, X.N. Zhu, Journal of Physics D-Applied Physics 42 (2009).

[11] G. Raciukaitis, Laser structuring of conducting films on transparent substrates for electronics devices, in: vol 7142, SPIE, Riga, Latvia, 2008, p. Optical Society of America (OSA); European Optical Society (EOS); University of Latvia; Latvian Council of Science.

[12] J. Bovatsek, A. Tamhankar, R.S. Patel, N.M. Bulgakova, J. Bonse, Thin Solid Films 518 (2009) 2897-2904.

[13] A.K. Dubey, V. Yadava, International Journal of Machine Tools & Manufacture 48 (2008) 609-628.

[14] G. Raciukaitis, P. Gecys, R. Trusovas, R. Kondrotas, Picosecond laser scribing for thin-film solar cell manufacturing, in: Laser Institute of America, Wuhan, China, 2010.

[15] C. Molpeceres, S. Lauzurica, J. Ocana, J. Gandia, L. Urbina, J. Carabe, Journal of Micromechanics and Microengineering 15 (2005) 1271-1278.

[16] H.W. Choi, D.F. Farson, J. Bovatsek, A. Arai, D. Ashkenasi, Applied Optics 46 (2007) 5792-5799.

[17] M. Park, B.H. Chon, H.S. Kim, S.C. Jeoung, D. Kim, J.I. Lee, H.Y. Chu, H.R. Kim, Optics and Lasers in Engineering 44 (2006) 138-146.

[18] D. Ashkenasi, M. G, R. A, S. R, H. I.V, B. N.M, C. E.E.B, Applied Physics A: Materials Science and Processing 77 (2003) 223-228.

[19] S. Chen, M. Chini, H. Wang, C. Yun, H. Mashiko, Y. Wu, Z. Chang, Appl. Opt. 48 (2009) 5692-5695.

[20] E.G. Gamaly, A.V. Rode, B. Luther-Davies, V.T. Tikhonchuk, Physics of Plasmas 9 (2002) 949-957.

[21] J.M. Liu, Optics Letters 7 (1982) 196-198.

[22] R. Le Harzic, D. Breitling, M. Weikert, S. Sommer, C. Fohl, S. Valette, C. Donnet, E. Audouard, F. Dausinger, Applied Surface Science 249 (2005) 322-331.

[23] M.D. Perry, B.C. Stuart, P.S. Banks, M.D. Feit, V. Yanovsky, A.M. Rubenchik, Journal of Applied Physics 85 (1999) 6803-6810.

[24] H.R. Le, N. Huot, E. Audouard, C. Jonin, P. Laporte, S. Valette, A. Fraczkiewicz, R. Fortunier, Applied Physics Letters 80 (2002) 3886-3886.

[25] Z.B. Wang, M.H. Hong, Y.F. Lu, D.J. Wu, B. Lan, T.C. Chong, Journal of Applied Physics 93 (2003) 6375-6380.

Chapter 5 - Femtosecond laser patterning of solar cells Mo thin film on flexible substrate for CIGS

Published in: 30th International Congress on Applications of Lasers and Electro-Optics, ICALEO 2011, p 869-874, 2011

Authors's Names: Qiumei Bian[1];Yu, Xiaoming[1]; Zhao, Baozhen[2]; Chang, Zenghu[3]; Lei, Shuting[1]

Author's Affiliation:

1 Department of Industrial and Manufacturing Systems Engineering, Kansas State University, KS 665062

2. Department of Physics, Kansas State University, 66502

3. The College of Optics & Photonics, University of Central Florida Orlando, FL 32816

5.1 Abstract

Finding ways to scribe Mo back conductor plays an important role in the fabrication and assembly of CIGS thin film solar cells. Using a femtosecond (fs) laser, we selectively removed the Mo thin films of 800 ~850 nm thick on flexible Polyamide (PI) substrates. In particular, we studied the effect of laser fluence and laser scanning speed on the ablation quality. The single pulse damage thresholds at various pulse durations were determined. Clean removal of the Mo layer was observed when laser fluence was above the threshold of 0.08-0.1 J/cm^2. Furthermore, the morphologies and structure of the grooves were characterized using scanning electron microscope (SEM) and KLA Tencor P-16 Profiler. The femtosecond laser provides a unique scheme to ablate the metal layer on flexible substrates for the fabrication of thin film solar cells.

5.2. Introduction

The multilayer $CuIn_xGa_xSe_2yS_y$ (CIGS) thin film solar cell has drawn people's attention due to its unique advantages of low production cost and high photovoltaic energy conversion efficiency. CIGS has been recognized as the most efficient thin-film solar cell with conversion efficiency of 19.96 % in the research lab [1]. The material cost of CIGS thin-film cells can be very inexpensive since it requires few raw materials. The manufacturing cost can be reduced with an efficient, scalable roll-to-roll process.

The all laser-scribing approach can offer certain all-in-line advantages in terms of module manufacturing. The conventional scribing process for monolithically integrated CIGS modules in production lines typically involves three steps: laser patterning of the Mo back conductor (P1), followed by mechanical patterning of the absorption layer (P2) and finally laser patterning of the front conductor layer (P3) [2].

During its in-line production the Mo-film has to be line structured and separated for the monolithic serial interconnection. Structuring the molybdenum film with ns-lasers has been investigated, the residues of Mo that were projected onto the walls of the ablation grooves and the metallization of the absorber close to the grooves were found [3, 4], which all affect the efficiency of the solar cells.

Femtosecond (fs) laser has shown advantages in thin film structuring such as cracks free and little thermal heat affect zone (HAZ). Hermann *et al.* [5] demonstrated that femtosecond laser was an effective tool to do the P1 scribe for CIS-based solar cells without relevant change in their photo-electrical properties. Zimmer *et al.* [6] demonstrated that femtosecond laser can produce high quality scribing for photovoltaic applications. Although both ps and fs laser P1 scribes for CIS and CIGS have produced higher quality scribing patterns on the glass substrate

compared to the nanosecond laser scribes, there are very few researches on the selective removal of metal thin films on flexible substrates using fs laser.

In this paper, fs laser scribing of the Mo thin film on the flexible PI substrate is conducted. The main objective of this study is to investigate how the operating parameters affect the scribe quality and how high precision grooves can be fabricated using fs laser.

5.3. Experimental setup

The fs laser system used in this study has a center wavelength of 800 nm, repetition rate of 1 kHz, and maximum energy of 5.1 mJ. The pulse duration is ~60 fs. The pulse duration can be adjusted by varying the gratings distance of the compressor measured by an autocorrelator. A neutral density filter is applied to adjust the pulse energy. The pulse energy is measured with a power meter. The laser beam is focused on the sample surface by a 100 mm focal length lens. The sample was fixed on a micro-positioning stage controlled by a computer to move in the x, y and z directions.

The thin-film sample used in this study consists of a back contact layer (molybdenum, Mo) and a PI substrate. The thicknesses of the Mo layer and the PI layer are 800~850 nm and 25 micrometer, respectively. The Mo thin film was deposited on the PI substrate using electron beam evaporation.

In this study, laser ablation experiments were first conducted to find the material breakdown threshold at different pulse durations in order to optimize the pulse energy for scribing the thin film later. Then laser scribing experiments were performed to investigate how the operating parameters such as pulse fluence and laser scanning speed affect the groove geometry morphology. Sets of grooves were cut in the Mo samples under various conditions, namely variable laser fluence and laser scanning speed. The beam overlap along a line was

controlled by the laser scanning speed and pulse reperition rate. Each scribing was completed in a single pass. The laser fluence varied in a range from 0.1 J/cm^2 to 1.2 J/cm^2. The laser scanning speed ranges from 0.1 mm/s to 10 mm/s.

To analyze the morphologies of the grooves, a KLA Tencor P-16 Profiler and scanning electron microscopy (SEM) were used to allow visual comparison in terms of quality and structure in both 2D and 3D. The groove electrical isolation was examined using a multimeter. The groove width affects the dead area and electrical resistance and thus affects the module efficiency. The groove depth is a key factor to assess whether the thin film is completely removed.

5.4 Experiments and results

5.4.1 Single pulse material damage threshold

Damage threshold is a characteristic dependent on the wavelength, pulse width and type of material. It is ideally defined as the laser fluence at which irreversible damage occurs in the material by removing a monolayer of material. It is actually determined by visual examination, ablation depth measurement, plasma radiation monitoring etc. In this work the damage threshold is estimated by recording the diameter (D) and the depth of single-shot ablated craters using SEM and KLA Tencor P-16 Profiler and then using the following linear relationship between the square of the crater diameter and the logarithm of the laser pulse energy[7]:

$$D^2 = 2\omega_0^{\,2} \ln\left(\frac{E_0}{E_{th}}\right) \tag{1}$$

where E_{th} = damage threshold and $2w_o$ = spot size. A plot of the square of damage diameter, D^2, against the logarithm of pulse energy is made to obtain both the spot size (slope of line) and

damage threshold (the extrapolation of D^2 to zero value) (Figure 5-1). The damage threshold was shown in Figure 5-1. The Mo and PI damage threshold at 60 fs were found to be 0.18 J/cm^2 and 0.75 J/cm^2, respectively. The Mo damage threshold slightly increases with increased pulse width, which is consistent with the previous research of fs laser ablation of Cu and Al film and fs laser ablation of fused silica [8, 9]. Based on the Mo and PI damage threshold, the operation parameters can be determined to carry out scribbling Mo film on PI substrates.

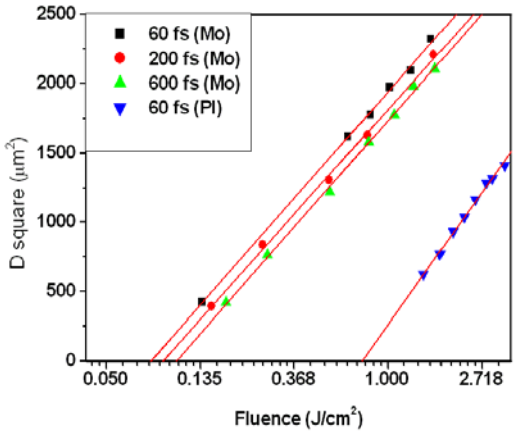

Figure 5-1 Single pulse damage threshold of Mo and PI with tuning fluence at various pulse duration.

5.4.2 The evaluation of the groove morphology and quality

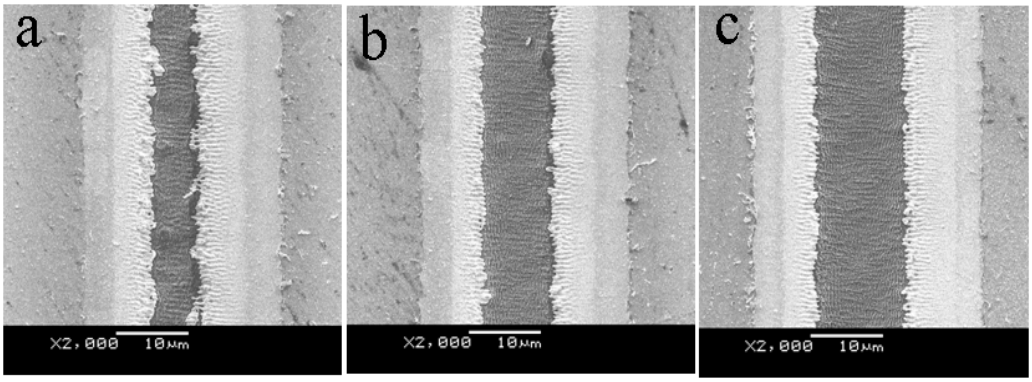

Figure 5-2 SEM images of the grooves with the fixed scanning speed of 1mm/s at the fluence of (a) 0.5 J/cm^2, (b) 0.7 J/cm^2, (c) 0.9J/cm^2.

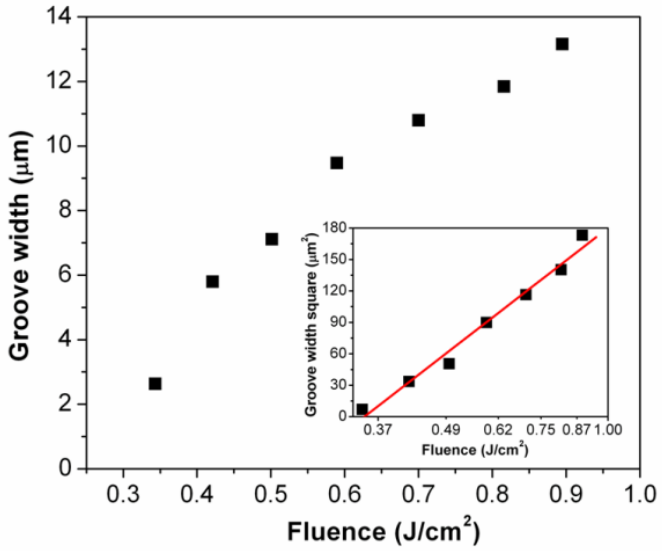

Figure 5-3 Variations of groove width with laser fluecnce at the fixed scanning speed of 1mm/s.

The groove morphologies of the Mo film were investigated with SEM and 3D profiler. The laser beam conditions such as pulse fluence and scanning speed play a critical role in the fabrication of the grooves with required dimension in the Mo back conductor layer. As shown in Figures 5-2 and 3, the groove width increases from 3 to 13 mm for the laser fluence from 0.34 to 0.90 J/cm^2. The straight lines of curve fitting experimental data, as shown in the inset of Figure 5-3, confirms the logarithmic relationship between the groove width and laser energy. Figure 5-4 shows the 3D structures of the grooves with scanning speed of 1 mm/s and different laser fluences. When the laser scanning speed is fixed at 1 mm/s, the substrate is damaged at the fluence of 0.9J/cm^2, as shown in Figure 5-4(c). While the incomplete removal of Mo is observed when the fluence is too low as shown in Figure 5-4 (a). The groove depth and the groove width increase with increasing laser fluence. The total amount of energy absorbed by the material increases with increasing pulse energy. The higher laser fluence intensified the material removal process.

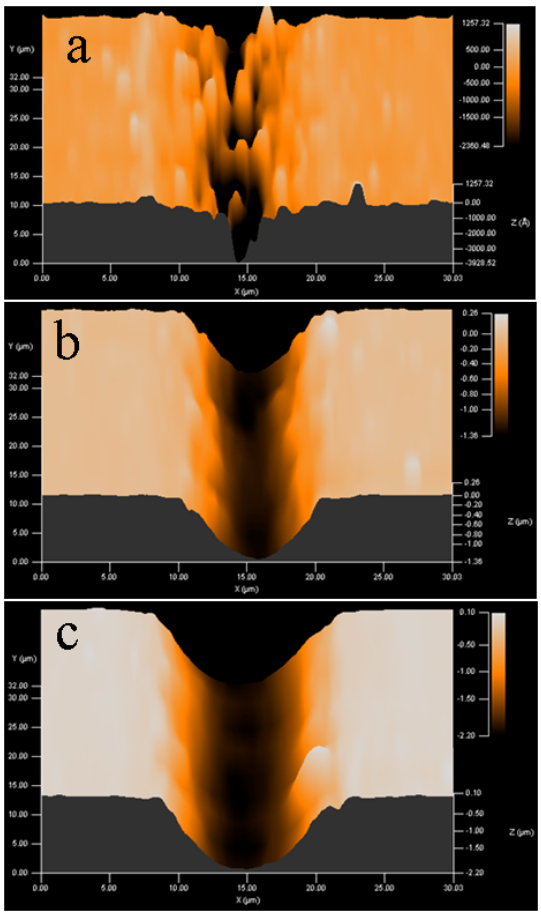

Figure 5-4 3D profiles of the grooves with scanning speed of 1 mm/s, at fluence of a, 0.34 J/cm^2, b, 0.6 J/cm^2, and c, 0.9J/cm^2.

There are ridges on both sides of the grooves. Although heat affected zones have been found to be very small for fs laser ablation in comparison with nanosecond laser ablation in the low fluence regime[10], at high fluences (more than five times of the damage threshold), thermal effects even occur in the fs range. The groove ridges are the results of the thermal effect and it is believed to be formed by extruding the melted material by vapor pressure.

On the other hand, the laser scanning speed affects the morphologies and structure of the grooves at a fixed fluence. The scanning speed is related to the number of pulses absorbed by the material based on the equation N=RS/V, where N is the pulse number, R the pulse repetition rate, S the beam spot size and V the sample scanning speed.[11]

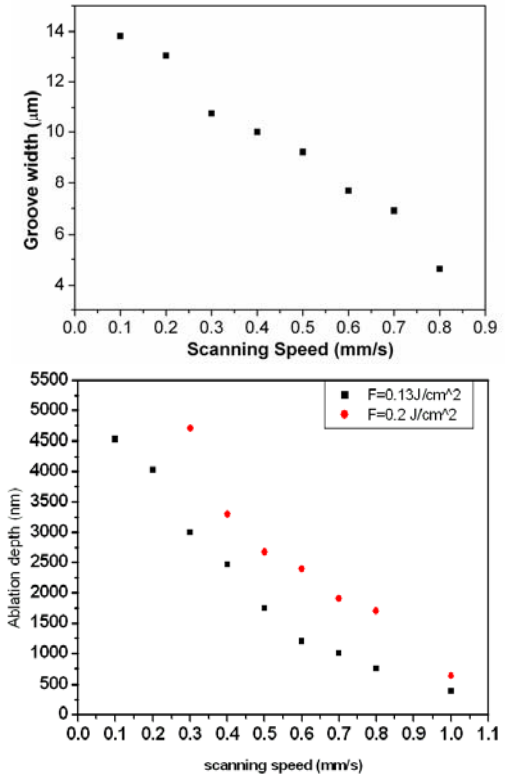

Figure 5-5 Variations of groove width (top) and groove depth (bottom) with scanning speed.

Ablation depth and width at fixed fluences decrease with increasing scanning speed as shown in Figure 5-5. At low scanning speed (0.1 mm/s), we can observe the groove with the width of 13 micrometer. With the higher feed rate (0.8 mm/s), the width decreases to 3 micometer. In particular, at the feed rate of 1 mm/s or beyond, the Mo along the groove is partially removed and the groove could not totally electronically separate the two sides of the Mo

film. Furthermore, the ablation depth decreases with increasing scanning speed at laser fluences well above the damage threshold, as shown in Figure 5-5. In comparison with the grooves at high scanning speeds, the grooves at lower speeds show wider and deeper shapes due to the accumulation of the irradiation energy. This could be explained by the increase of beam overlap at low speeds, resulting in increased laser energy accumulation and deposition at the same spot in the Mo thin film.[12, 13] Therefore, we can tune the laser scanning speed to control the groove with required morphologies such as designed groove depth and width.

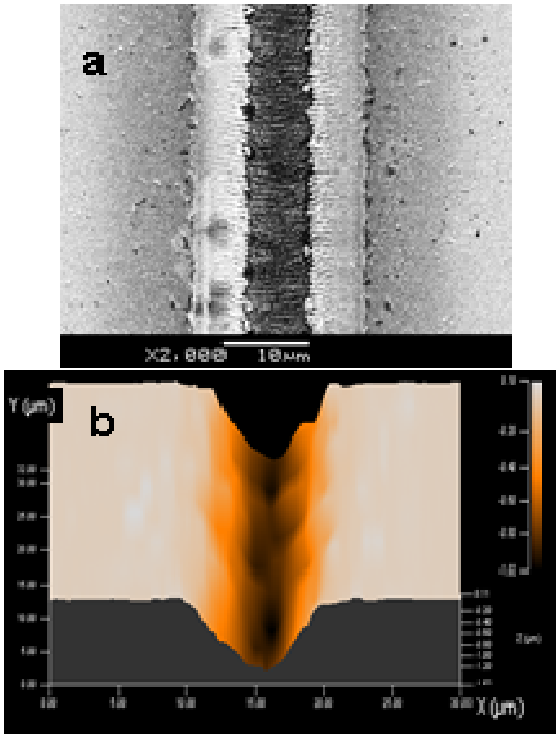

Figure 5-6 Morphologies of a high quality groove ablated in the Mo thin film at the condition of laser fluence of 0.24 J/cm^2, the scanning speed of 0.6 mm/s, and pulse duration of 60 fs; (a) SEM image and (b) 3D profiler image.

By tuning the laser fluence to 0.24 J/cm^2 and scanning speed at 1 mm/s, a high quality scribe groove is achieved, as shown in Figure 5-6. The groove width is 7 mm and the Mo layer is totally removed with limited damage to the PI substrate, as shown in Figure 5-6b. The electrical

resistance was examined using the multimeter, which confirmed that the groove was electrically isolated.

5.5. Conclusions

In summary, fs laser has been utilized to scribe Mo thin film on PI flexible substrate for CIGS thin film solar cells. The damage threshold of Mo thin film was found to be 0.08~0.1 J/cm^2 when the pulse duration varies from 60 to 600 fs. An important focus of this study is to determine the optimum regime of laser ablation to produce high quality grooves by investigating the key factors including laser fluence and scanning speed. The following parametric regime produces a groove with high quality: the suitable beam fluence is 0.24 J/cm^2 and the scanning speed is 0.6 mm/s. The ongoing work is focused on applying fs laser for the ablation of P2 and P3 layers for CIGS solar cells on the flexible substrate for roll to roll production. Overall, it appears that fs laser is a promising tool for selective removal of metal thin film conductor layers on flexible polymer substrates, which could result in an improved performance of CIGS and other thin film solar cells due to the high quality of interconnection grooves.

5.6 Acknowledgments

Financial support of this work by the National Science Foundation (under Grant No. CMMI-0826184 and CMMI-0826015) and the DoD Army Research Office (under the Agreement Number W911NF-07-1-0475) is gratefully acknowledged.

5.7 References

[1] M.A. Green, K. Emery, Y. Hishikawa, W. Warta, Progress in Photovoltaics: Research and Applications 19 84-92.

[2] M. Powalla, M. Cemernjak, J. Eberhardt, F. Kessler, R. Kniese, H.D. Mohring, B. Dimmler, Solar Energy Materials and Solar Cells 90 (2006) 3158-3164.

[3] J. Hermann, M. Benfarah, S. Bruneau, E. Axente, G. Coustillier, T. Itina, J.F. Guillemoles, P. Alloncle, Journal of Physics D: Applied Physics 39 (2006) 453-460.

[4] J. Hermann, M. Benfarah, G. Coustillier, S. Bruneau, E. Axente, J.F. Guillemoles, M. Sentis, P. Alloncle, T. Itina, Applied Surface Science 252 (2006) 4814-4818.

[5] J. Hermann, M. Benfarah, S. Bruneau, E. Axente, G. Coustillier, T. Itina, J.F. Guillemoles, P. Alloncle, Journal of Physics D-Applied Physics 39 (2006) 453-460.

[6] D. Ruthe, K. Zimmer, T. Hoche, Applied Surface Science 247 (2005) 447-452.

[7] J.M. Liu, Optics Letters 7 (1982) 196-198.

[8] R. Le Harzic, D. Breitling, M. Weikert, S. Sommer, C. Fohl, S. Valette, C. Donnet, E. Audouard, F. Dausinger, Applied Surface Science 249 (2005) 322-331.

[9] M.D. Perry, B.C. Stuart, P.S. Banks, M.D. Feit, V. Yanovsky, A.M. Rubenchik, Journal of Applied Physics 85 (1999) 6803-6810.

[10] H.R. Le, N. Huot, E. Audouard, C. Jonin, P. Laporte, S. Valette, A. Fraczkiewicz, R. Fortunier, Applied Physics Letters 80 (2002) 3886-3886.

[11] Z.B. Wang, M.H. Hong, Y.F. Lu, D.J. Wu, B. Lan, T.C. Chong, Journal of Applied Physics 93 (2003) 6375-6380.

[12] M. Park, B.H. Chon, H.S. Kim, S.C. Jeoung, D. Kim, J.I. Lee, H.Y. Chu, H.R. Kim, Optics and Lasers in Engineering 44 (2006) 138-146.

[13] A.G. Aberle, Thin Solid Films 517 (2009) 4706-4710.

Chapter 6 - Predictive 3D model for femtosecond laser ablation of Mo thin film

6.1 Abstract

Mo ablation by a single femtosecond laser pulse is simulated through a two temperature model. Temperature evolutions in spatial and time domain for both electrons and lattice are obtained, which can give us insights of the energy transformation process during femtosecond ablation. Simulated 3D ablation craters excited by a single pulse with different fluences are acquired, from which we can predict crater depth and radius varying with the fluence before actual ablation takes place, which can help optimize the process regime for femtosecond laser thin film patterning for thin film solar cells. Comparisons made between the experimental results and simulation predictions show the reliability of the proposed ablation model.

6.2 Introduction

Femtosecond (fs) laser ablation is of significant interest both to basic research and industrial applications [1-3]. Fs laser pulses offer great potential for materials processing such as minimal damage and high precision [2, 4, 5]. The ability of fs pulsed lasers to produce microstructures of high quality and with good efficiency has led to an increasing interest for scientific investigations and practical applications. Additionally, fs laser discloses a new dimension of micro and nano fabrication with decreasing structure size combined with a high performance [6, 7]. Practical applications include hole drilling and structuring of different components which can be applied successfully in various fields, from microelectronics to photovoltaic[8, 9].

In order to utilize the advantages of fs lasers in thin film solar cell manufacturing, the fabrication process has to be optimized for thin film patterning and structuring applications concerning both efficiency and quality. In last decade, the availability of fs pulsed laser systems have allowed a considerable enhancement of ablation quality [10]. However, a further improvement of the processing regime is desired. The latter can be facilitated by a fundamental understanding of the physical mechanisms during the ablation process which are often difficult to identify by diagnostic experiments alone due to the short timescales and small interaction zones. The understanding of the physical processes involved in metal thin film ablation by fs laser pulses and the calculation of the associated fluence thresholds, ablation rate and crater geometry information are of great importance. Simulations can help to understand the important influences of energy coupling, material heating and evaporation as well as ejection dynamics involved in laser ablation processes with fs laser pulses and predict the optimal process regime such as process fluence, process speed and applied optics.

Fs laser ablation involves many complicated physical processes, including electron energy absorption and accumulation from photons [2, 11], electron and lattice energy transportation coupling, damage formation and corresponding energy loss. During the process of fs laser ablation, the electron lattice relaxation time is typically on the order of several tens of picoseconds[12], while the actual laser pulse has tens to hundreds of femtoseconds, hence the electron and lattice exposed to fs laser pulses gets excited into a high non-equilibrium state, and the classical Fourier heat conduction equation is unavailable in such a highly non-equilibrium state. In order to characterize the non-equilibrium behaviors of the electron and lattice temperatures in metals, Kaganov *et al.* first theoretically investigated the thermal coupling between electrons and phonons [13]. Later, a parabolic two-temperature heat transportation

model was proposed by Anisimov *et al.* [14]. The parabolic two-temperature model (TTM) cannot accurately capture the lattice temperature response, especially for the late time since the heat conduction in lattices and electrons was not taken into account. On a quantum mechanical and statistical basis, Qiu and Tien derived a more rigorous hyperbolic two-step radiation heating model which accounts for the ballistic heat transport through electron [15]. It describes better results than Anisimov *et al.* for laser pulse durations comparable to the electron relaxation time, which is from sub-femtoseconds to a few femtoseconds for metals and depends on the electron and phonon temperatures. Chen and Beraun proposed a dual-hyperbolic two-temperature model, which extended the Qiu and Tien's model by adding the relaxation behavior of and the heat conduction in lattice[16]. Basically all two temperature models assumed that the incident laser pulse excites the electrons that are located within the skin depth of the metal. Then, a portion of the thermal electron energy transfers to the neighboring lattice, whereas another part of the energy diffuses, through electrons, into the deeper region of the material. Once the laser pulse turns off, the thermal coupling between the electrons and lattice as well as the heat conductions in the electrons and lattice continues until equilibrium and steady state is established. For pure metals, heat conduction in the lattice is small compared to that in the electrons. Therefore, the heat transport in the lattices is often neglected. Since the electron relaxation time is shorter than several tens of fs for metals, the difference between the parabolic and hyperbolic models would be insignificant [17].

The parabolic two temperature model is widely applied in ultra-short laser interaction with metal and metal thin films. Among these, Qiu and Tien studied the heat transfer mechanism during ultra-short laser heating of metals using both numerical and experimental methods [15, 18-20]. Heat-affected zone and ablation rate of copper ablated by fs laser pulse was investigated

using parabolic TTM [21, 22]. An analytical solution of the TTM describing ablation of metals with Gaussian laser source was obtained with the assumptions that the lattice heat capacity and the thermal conductivity of the electron and lattice subsystems remain approximately constant during the process [23]. A very good agreement between experimental data and simulation results was found by using the parabolic one dimensional TTM for copper, silver and tungsten metal [4, 24]. An enthalpy form of TTM is proposed to calculate the superheating process and material removal from metallic materials based on the concept of phase explosion for gold thin film [25]. Stein *et al.* investigated the ultra-short pulse ablation of aluminum and silver thin films using TTM method. However, based on our knowledge, there is no ultra-short laser ablation modeling of molybdenum in the literature. Laser patterning of Mo is a very important process for CIGS thin film solar cells fabrication. It is necessary to model fs ablation of Molybdenum (Mo) thin film to understand the ablation mechanisms and optimize Mo thin film patterning process. The TTM has been proved to be an effective means to model and simulate laser ablation of metals. The main goal of this study is to gain a fundamental understanding of the mechanisms in fs laser ablation of Mo thin film using a combination of experiments and TTM numerical modeling.

In this paper, we introduce a 3D parabolic TTM to simulate fs ablation of Mo thin film. By using a finite-difference method to solve the temperature equations, we obtain the 3D temperature field evolution for both electrons and lattice, which presents us a vivid view of the energy transformation process during fs ablation. Meanwhile, the ablation threshold, ablation rate and single pulse ablated crater geometry are calculated. In order to verify our calculations, the single-pulse ablation experiment is carried out. Craters radii and the single-pulse threshold

fluence are obtained. Comparisons between theoretical analysis and the corresponding experimental results show the feasibility of our two temperature model in low fluence regime.

6.3 Numerical model

The well-known parabolic TTM originally proposed by Anisimov *et al.* is presented as follows [14]:

$$Ce\frac{\partial Te}{\partial t} = \nabla(k_e \nabla T_e) - G(T_e - T_i) + I \quad \textbf{(1)}$$

$$C_i\frac{\partial T_i}{\partial t} = G(T_e - T_i) \quad \textbf{(2)}$$

Here $C_e = kT_e$ and k_e are the heat capacity and thermal conductivity of electrons, respectively; k is electron heat capacity linear temperature dependence coefficient at room temperature; $k_e=k_{e0}$ (T_e/T_i) and k_{e0} is electronic heat conductivity at room temperature; C_i is the lattice heat capacity, which we take as a constant; *G* is the electron lattice coupling coefficient, and *I* (r, z, t) is the laser heating source term which can be described by

$$I = I_0 a(1-R)e^{-4\ln\left(\frac{2(t)^2}{\tau^2}\right)}e^{-\alpha z - 2r^2/{\omega_0}^2} \quad \textbf{(3)}$$

where, R is the reflectance of the target; *I* is laser intensity, in the present paper, given by a Gaussian distribution in both time and spatial domain; r and z are the radius and depth respectively in cylindrical coordinates; w_0 is the $1/e^2$ radius of the laser spot and τ is the FWHM pulse duration; α is the light absorption coefficient, I_0 is the peak intensity of the laser pulse.

As the ablation process takes place on a timescale of several tens of picoseconds, it is reasonable to ignore the heat losses from the metal film to the surrounding and to the front surface during the ablation process, so the initial and boundary conditions can be given by:

$$T_e(r,z,0) = T_i(r,z,0) = T_0 \tag{4}$$

$$\frac{\partial T_e}{\partial z}\Big|_{z=0} = \frac{\partial Te}{\partial z}\Big|_{z=2\mu m} = \frac{\partial T_e}{\partial r}\Big|_{r=0} = \frac{\partial T_e}{\partial r}\Big|_{r=50\mu m} = 0 \tag{5}$$

$$\frac{\partial T_i}{\partial z}\Big|_{z=0} = \frac{\partial T_i}{\partial z}\Big|_{z=2\mu m} = \frac{\partial T_i}{\partial r}\Big|_{r=0} = \frac{\partial T_i}{\partial r}\Big|_{r=50\mu m} = 0 \tag{6}$$

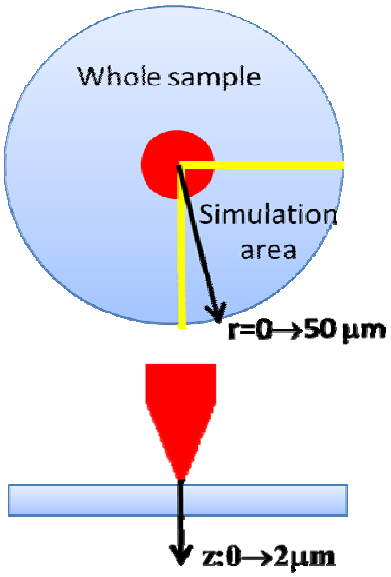

Figure 6-1 Schematic of diagram of the simulation boundary

Where T_0=300 K is the initial temperature of the Mo film; Z is the thickness of the Mo film (2 μm) as shown in Fig.6-1. We assume no heat losses from the sample surfaces in the short time response and there is no heat loss at the center of the sample due to the cylindrical symmetry of the model. We use the finite-difference method to solve Eqs. (1) and (2). Based on Eqs. (1) and (2), the energy equations describing the continuous energy flow in metals from hot electrons to lattices during non-equilibrium heating in cylindrical polar coordinates can be written as follows:

$$C_e \frac{\partial T_e}{\partial t} = \frac{\partial^2 T_e k_e}{\partial r^2} + \frac{1}{r}\frac{\partial T_e k_e}{\partial r} + \frac{\partial^2 T_e k_e}{\partial z^2} - G(T_e - T_i) + I_0(1-R)\alpha exp^{-\alpha z - \frac{2r^2}{\omega_0{}^2}} exp^{-4ln2\left(\frac{(t)^2}{\tau^2}\right)} \tag{7}$$

$$T_{e(r,z)}^{p+1} = \frac{\Delta t}{c_e}\left\{\left[\frac{T_{e(r+1,z)}^{p}-2T_{e(r,z)}^{p}+T_{e(r-1,z)}^{p}}{\Delta r^2}+\frac{1}{r}\frac{T_{e(r+1,z)}^{p}-T_{e(r-1,z)}^{p}}{2\Delta r}+\frac{T_{e(r,z+1)}^{p}-2T_{e(r,z)}^{p}+T_{e(r,z-1)}^{p}}{\Delta z^2}\right]+ G\left[T_{e(r,z)}^{p}-T_{i(r,z)}^{p}\right]+I_0(1-R)\alpha exp^{-\alpha z-\frac{2r^2}{\omega_0^2}} exp^{-4\ln\left(2\frac{t^2}{\tau^2}\right)}\right\} \quad (8)$$

$$T_{i(r,z)}^{p+1} = \Delta t * G\,(T_e^{p} - T_i^{p})/C_i \quad (7)$$

Where *r, z* are in the cylindrical coordinates.

A time step of 2.5 fs, an r step of 0.5 μm and a z direction step of 5 nm and z axis parallel to the laser direction are used in the simulation as shown in Fig.6-1. The physical parameters of Mo and the laser beam parameters used in the numerical simulations are given as follows [26]**:**

k_{e0} = 138 J/ (mK s), k= 242 J/ (m^3 K^2), G = 1×10^{17} J/ (m^3Ks), Ci = $2.65X10^6$ J/ (m^3 K),

R = 0.55, α= 0.825×10^7 /m, T_0 = 300 K, τ = 60 fs ,w_0 = 8.2μm

Solving the TTM equations yields the electron and lattice temperatures as a function of time and special coordinates (r, z) in the sample. A typical result of such a calculation, for pulse duration of 60 fs, is shown in Fig.6- 2.The material in the areas with a lattice temperature higher than 9300 K is considered ablated.

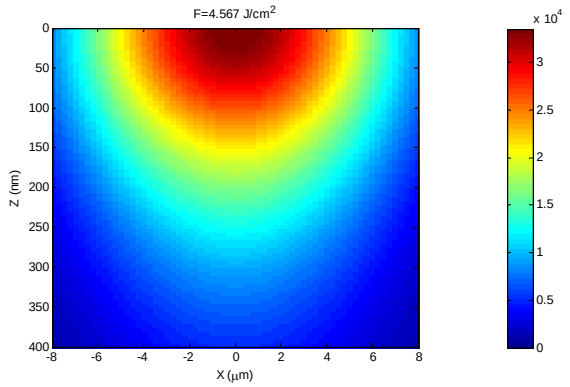

Figure 6-2 lattice temperature field at t = 50 ps for laser fluence=4.567 J/cm^2

6.4 Results and discussion

The TTM equations are solved numerically in MATLAB. Solving the TTM equations yields the electron and lattice temperatures as a function of time and space in the sample. A typical result of such a calculation, for pulse duration of 60 fs, is shown in Fig. 6-3. In Fig. 6-3(a), it can be seen how the electron system is heated on the fs time scale and that a maximum electron temperature of more than 20,000 K is reached on the surface after approximately 60 fs. In contrast, the lattice remains cold for the first few picoseconds and is then heated via electron–phonon collisions over a timescale of a few picoseconds. This clearly shows us that laser energy is first absorbed by the electrons. As time goes on, the electrons' temperature drops while the lattice temperature increases. So during this period laser energy is transferred from the high temperature electrons to the lattice. At the time of about 50 ps the two temperatures are approximately the same and the target remains at thermal equilibrium from that time on.

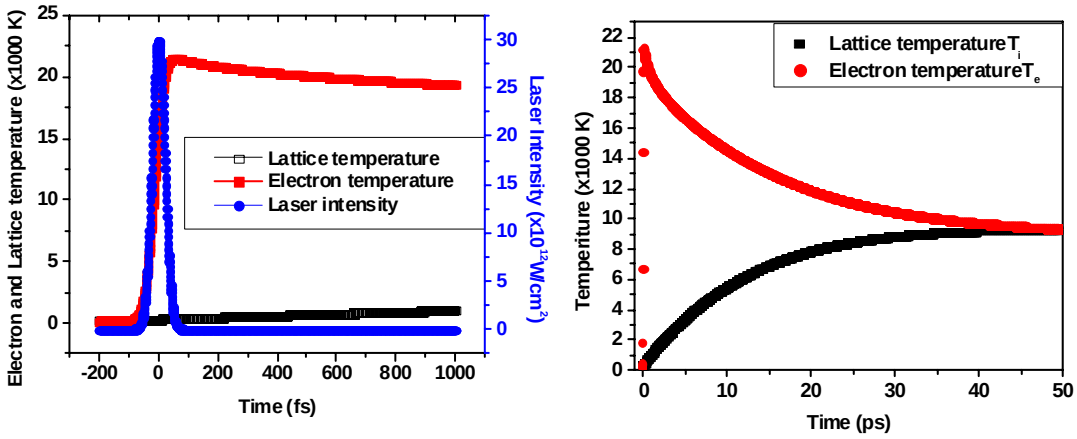

(a) 1000 fs after the fs laser pulse (b) 50 ps after the fs laser pulse

Figure 6-3 Electron (upper curve, red) and lattice (black) temperature evolution on Mo thin film surface, heated by a 60 fs-pulse with a fluence of 0.75 J/cm^2

In the present paper, we assume that ablation takes place when the lattice temperature reaches the thermodynamic critical temperature Tc. It is well known that during the ablation process, when the temperature of the lattice reaches the thermodynamic critical temperature Tc (for Mo it is 10333 K), such a high temperature would inevitably lead to an extremely high pressure in the ablated region, and such a great pressure will be released through adiabatic expansion, which would finally lead to obvious material ablation and ejection by phase explosion and phase separation [27, 28]. In the actual calculation 0.9 Tc is always set as the critical temperature for material removal during fs ablation since when the calculated lattice temperature is equal to or greater than 0.9 Tc , phase explosion is assumed to take place [29].

By means of the temperature evolution of the sample in z and r directions we can predict the shape of ablated holes. Fig. 6-4 presents simulated craters by single pulse ablation with different fluences. It can be seen from Fig. 6-4 a, b, and c that with the increase of laser fluence, there is an obvious increase in the ablation depth and crater diameter.

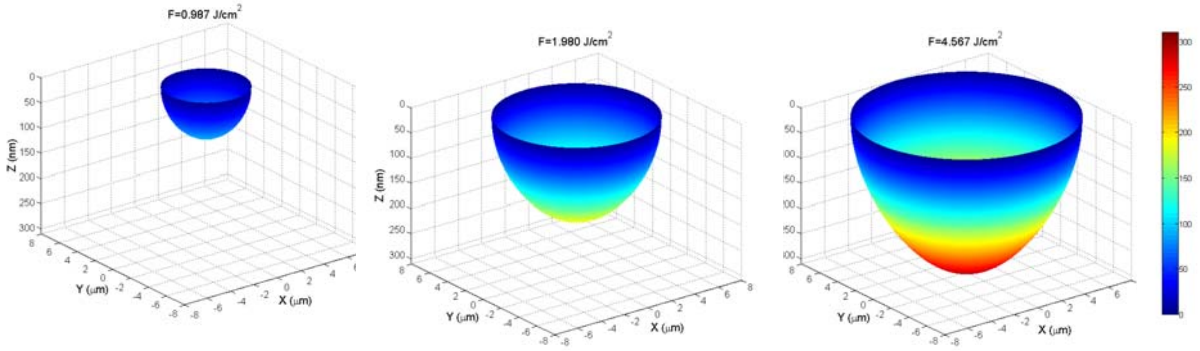

(a) (b) (c)

Figure 6-4 Simulated 3D craters by single pulse ablation with different laser fluences: (a) 0.99 J/cm^2 (b) 1.98 J/cm^2 (c) 4.57 J/cm^2

6.5 Comparison with the experimental results

6.5.1 Experimental conditions

A fs laser system is used in this study, which consists of a commercially available Ti:Sapphire chirped pulse amplifier (CPA) that operates at 1 kHz, seeded by a Rainbow oscillator. The laser beam delivered from this system has center wavelength of 800 nm, repetition rate of 1 kHz, and maximum pulse energy of 5 mJ. The pulse duration is ~60 fs right after the amplifier measured by the autocorrelator and can be adjusted by varying the gratings distance of the compressor. The laser beam is focused by a lens of 75 mm focal length for single shot damage threshold investigation. The laser beam is focused on the sample surface. The sample is fixed on a micro-positioning stage controlled by a computer to move in the x, y and z directions. To analyze the morphology of the grooves, a KLA Tencor P-16 Profiler and scanning electron microscope (SEM) are used to measure the crater diameter and depth .The ablation crater diameter is measured from SEM image and ablation depth is measured on 3D profiler images shown in Fig. 6-5 (a) and (b).

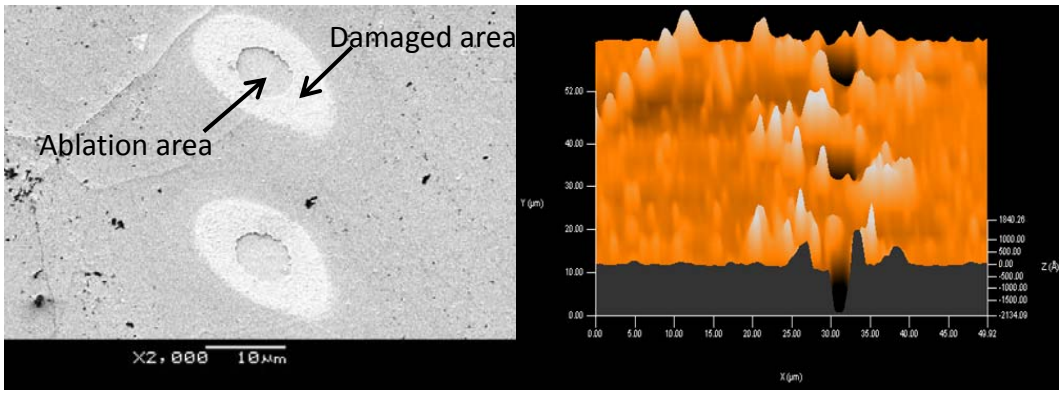

(a) SEM image **(b) 3D profile image**

Figure 6-5 Images of ablation crater at fluence 2.37 J/cm^2

6.5.2 Single pulse ablation rate

A series of simulations have been performed for Mo thin film. Fig. 6-6 (a) shows the ablation depth with respect to the flounce from both simulation and experiments. The results show that when the fluence is low there is a logarithmic dependence. Consequently, the simulation data are logarithmic like fitting and agree well with the experimental results. As in the high-fluence regime, the increase in the laser fluence results in a sharp increase in the ablation depth in the experimental results, while the simulation results do not agree well with it. For the TTM we applied, $k_e=k_{e0}(T_e/T_i)$ is limited to temperatures that are lower than the Fermi temperature T_F and the electron relaxing process will be dominated by electron and phonon collisions($10^{14}s^{-1}$) [30-33]. In high temperatures, the electron relaxing process will be dominated by electron and electron collision ($10^{16}s^{-1}$) and electron heat diffusion have to be taking into account [31-33]. In our TTM model, when laser fluence is greater than 3 J/cm^2, the electron temperature already reaches 4.28 x10^{4}K, which is greater than the Femi temperature (3.2x10^{4}K) of Mo. Therefore, our model in the high fluence regime needs to be adjusted. At high fluence levels, Nedialkov and Nolte claimed that the overheating of the metal above the critical temperature leads to a sharp rise in pressure in the volume, which causes the increase of the ablation rate. An analytical model of the ablation depth with the laser fluence was proposed, the relation is as below [32, 33]:

$$D=l * ln\ (F/F_{th})$$

The penetration depth is logarithmically dependent on the laser fluence. Here $l$is electron heat diffusion depth in the high fluence regime. It can be calculated as $l = 2\sqrt{k\tau_{ep}}$.=181 nm for Mo.κ

is the heat diffusivity of the material, and τ_{ep} is the electron–phonon coupling time, which can be calculated by C/G.[34]. After applying the electron heat diffusion depth of 181 nm as an effective penetration depth in our model, the experimental and simulation results agree very well as shown in Fig. 6-6 (b).

At higher fluences the average ablation rate is determined by the effective heat penetration depth, which is independent of the pulse duration. The greater effective penetration depth is a signature of significant heat diffusion in the material, and one will thus to a less degree observe the same benefits of a small heat-affected zone (HAZ), as in the low fluence regime.

Therefore, we should avoid applying the high fluence ablation when the large HAZ can induce the micro-crack in the Mo thin film, which would affect the thin film solar cell efficiency. Considering both the process productivity and the process quality, the medium fluence such as 2~3 J /cm^2 should be applied in the Mo thin film patterning in the future experiments in order to reach the minimal HAZ and high ablation rate such as 200~250 nm.

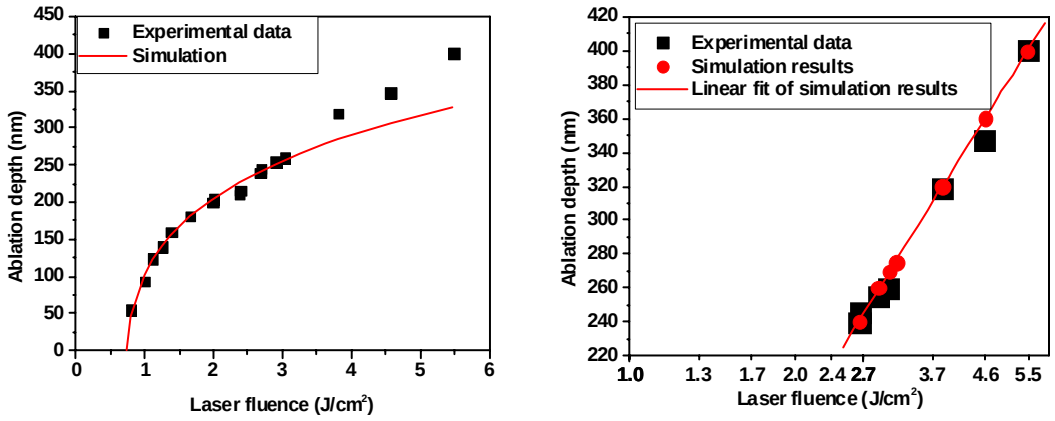

(a) **(b)**

Figure 6-6 Depth of ablation craters versus laser fluence: experimental (Black Square), simulation data (red line)

6.5.3 Ablated crater diameter and ablation threshold

At the low fluence regime, the ablation crater diameter increases with laser fluence in both the experimental and simulation results as shown in Fig.6-7. The simulation results agree very well with the experimental data and we can use this model to predict the crater diameter in this regime. For the high fluence regime, the model we proposed needs a correction, which is our next step for this research.

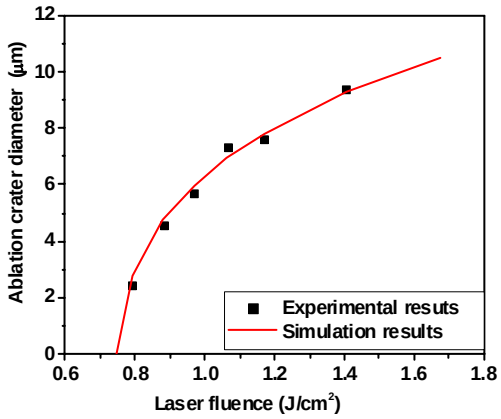

Figure 6-7 Ablation crater diameter with laser fluence

By simulating a series of single pulse ablation with varying fluences we determined the ablation threshold for Mo at a wavelength of λ = 800 nm and a constant pulse duration of τ = 60 fs. For comparison we also determined the ablation threshold experimentally using the same laser parameters. The results can be seen in Fig 6-8 showing the squared ablation diameters plotted against laser fluence in logarithmic scale. With the relation $D^2=2\omega_0 \ln F/F_{th}$, we obtained an ablation threshold fluence of F_{ths} = 0.748 J/cm^2 from the simulation and F_{the} = 0.76 J/cm^2 from the experiment. Taking into account that the simulation is assumed in the vacuum and experiment is in air and metal ablation in air is less efficient than in vacuum due to re-deposition of ablated material, it is quite reasonable to say that our experimental result fits very well with

the simulation at the lower fluence levels. Therefore, the model can be applied to predict the ablation threshold for metal thin film ablation in future experiments.

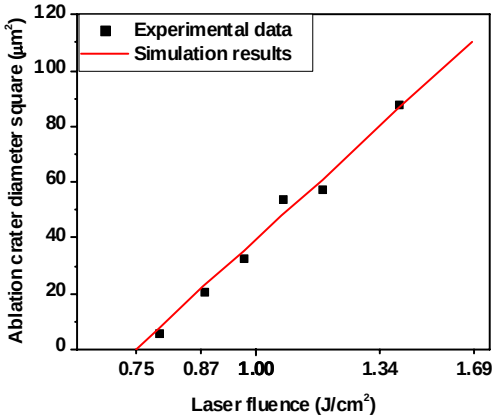

Figure 6-8 fs laser ablation thresholds for both experiment and simulation

6.6 Conclusions

A 3D TTM is usedto investigate fs laser ablation of Mo thin film. The energy transportation process between electron and lattice is clearly demonstrated. 3D craters ablated by single laser pulses with different laser fluences are simulated, from which the radii and depths of the ablation crater can be predicted before doing any experiments. A good agreement between simulation and experimental results is presented. Single pulse ablation rate for the fs laser ablation of Mo were calculated through the numerical model. The result of the simulation fits quite well with our experimental results. At lower fluences the material is removed through phase explosion and critical phase separation while at higher fluences thermal ablation is the dominant ablation mechanism for the case of Mo. The simulation model provides insights to the physical processes occurring during fs laser ablation of metals. Desired processing fluence and process speed regime can be predicted for Mo thin film by calculating ablation rate and ablation crater geometry using the developed simulation model at the low fluence regime. It also can be

applied to fs laser ablation of other metals and semiconductors with minor revision. However, the model needs further correction in order to be applied to high fluence ablation regime.

6.7 Acknowledgements

Financial support of this work by the DoD Army Research Office (under the Agreement Number W911NF-07-1-0475) and the National Science Foundation (under Grant No. CMMI-1131627)is gratefully acknowledged.

6.8 References

1 Rizvi, N.H.: 'Femtosecond laser micromachining: Current status and applications', Riken review, 2003, pp. 107-112

2 Anisimov, S.I., and Luk'yanchuk, B.: 'Selected problems of laser ablation theory', Physics-Uspekhi, 2002, 45, (3), pp. 293-324

3 Kim, J., and Na, S.: 'Metal thin film ablation with femtosecond pulsed laser', Optics and Laser Technology, 2007, 39, (7), pp. 1443-1448

4 Byskov-Nielsen, J., Savolainen, J.M., Christensen, M.S., and Balling, P.: 'Ultra-short pulse laser ablation of copper, silver and tungsten: experimental data and two-temperature model simulations', Applied Physics A: Materials Science & Processing, 2011, 103, (2), pp. 447-453

5 Chang, C.W., Chang, T.L., Tsai, T.K., Ting, C.J., Wang, C.P., and Chou, C.P.: 'Study of Metals by Femtosecond Laser Processing for Electro-Optics Applications', Key Engineering Materials, 2012, 516, pp. 263-268

6 White, Y.V., Li, X., Sikorski, Z., Davis, L.M., and Hofmeister, W.: 'Single-pulse ultrafast-laser machining of high aspect nano-holes at the surface of SiO< sub> 2</sub>', Optics Express, 2008, 16, (19), pp. 14411-14420

7 Kim, J., and Na, S.: ‘Metal thin film ablation with femtosecond pulsed laser’, Optics & Laser Technology, 2007, 39, (7), pp. 1443-1448

8 Zoppel, S., Huber, H., and Reider, G.: ‘Selective ablation of thin Mo and TCO films with femtosecond laser pulses for structuring thin film solar cells’, Applied Physics A: Materials Science & Processing, 2007, 89, (1), pp. 161-163

9 Bian, Q., Yu, X., Zhao, B., Chang, Z., and Lei, S.: ‘Femtosecond laser ablation of indium tin-oxide narrow grooves for thin film solar cells’, Optics & Laser Technology, 2012

10 Sibbett, W., Lagatsky, A., and Brown, C.: ‘The development and application of femtosecond laser systems’, Optics Express, 2012, 20, (7), pp. 6989-7001

11 Jiang, L., Li, X., Zhang, X.P., Chen, Q.H., Tsai, H.L., and Lu, Y.F.: ‘Short pulse laser micro/nano manufacturing: fundamentals and applications’, International Journal of Nanomanufacturing, 2011, 7, (2), pp. 126-142

12 Singh, N., and Singh: ‘TWO-TEMPERATURE MODEL OF NONEQUILIBRIUM ELECTRON RELAXATION: A REVIEW’, International journal of modern physics b, 2010, 24, (09), pp. 1141-1158

13 Kaganov, M., Lifshitz, I., and Tanatarov, L.: ‘Relaxation between electrons and the crystalline lattice’, Sov. Phys. JETP, 1957, 4, (2), pp. 173

14 Anisimov, S., Kapeliovich, B., and PERELMAN, T.L.: ‘Electron emission from metal surfaces under the action of ultrashort laser pulses’, Zhurnal Eksperimental'noi i Teoreticheskoi Fiziki, 1974, 66, pp. 776-781

15 Qiu, T., and Tien, C.: ‘Heat transfer mechanisms during short-pulse laser heating of metals’, Journal of Heat Transfer (Transactions of the ASME (American Society of Mechanical Engineers), Series C);(United States), 1993, 115, (4)

16 Chen, J., and Beraun, J.: 'Numerical study of ultrashort laser pulse interactions with metal films', Numerical Heat Transfer: Part A: Applications, 2001, 40, (1), pp. 1-20

17 Chen, J., Tzou, D., and Beraun, J.: 'A semiclassical two-temperature model for ultrafast laser heating', International Journal of Heat and Mass Transfer, 2006, 49, (1), pp. 307-316

18 Qiu, T., and Tien, C.: 'Femtosecond laser heating of multi-layer metals—I. Analysis', International Journal of Heat and Mass Transfer, 1994, 37, (17), pp. 2789-2797

19 Qiu, T., and Tien, C.: 'Short-pulse laser heating on metals', International Journal of Heat and Mass Transfer, 1992, 35, (3), pp. 719-726

20 Qiu, T., Juhasz, T., Suarez, C., Bron, W., and Tien, C.: 'Femtosecond laser heating of multi-layer metals—II. Experiments', International Journal of Heat and Mass Transfer, 1994, 37, (17), pp. 2799-2808

21 Hirayama, Y., and Obara, M.: 'Heat-affected zone and ablation rate of copper ablated with femtosecond laser', Journal of applied physics, 2005, 97, (6), pp. 064903-064903-064906

22 Christensen, B.H., Vestentoft, K., and Balling, P.: 'Short-pulse ablation rates and the two-temperature model', Applied Surface Science, 2007, 253, (15), pp. 6347-6352

23 Vatsya, S., and Virk, K.S.: 'Solution of two-temperature thermal diffusion model of laser–metal interactions', Journal of Laser Applications, 2003, 15, pp. 273

24 Byskov-Nielsen, J., Savolainen, J.M., Christensen, M.S., and Balling, P.: 'Ultra-short pulse laser ablation of metals: threshold fluence, incubation coefficient and ablation rates', Applied Physics A: Materials Science & Processing, 2010, 101, (1), pp. 97-101

25 Chen, J.K., and Beraun, J.E.: 'Modelling of ultrashort laser ablation of gold films in vacuum', Journal of Optics a-Pure and Applied Optics, 2003, 5, (3), pp. 168-173

26 Emelyanov, A., Pyalling, A., and Ternovoi, V.Y.: 'Investigation of near-critical states of molybdenum by method of isentropic expansion', International journal of thermophysics, 2005, 26, (6), pp. 1985-1995

27 Zhang, N., Zhu, X., Yang, J., Wang, X., and Wang, M.: 'Time-resolved shadowgraphs of material ejection in intense femtosecond laser ablation of aluminum', Physical review letters, 2007, 99, (16), pp. 167602

28 Cheng, C., and Xu, X.: 'Mechanisms of decomposition of metal during femtosecond laser ablation', Physical Review B, 2005, 72, (16), pp. 165415

29 Chen, J., and Beraun, J.: 'Modelling of ultrashort laser ablation of gold films in vacuum', Journal of Optics A: Pure and Applied Optics, 2003, 5, (3), pp. 168

30 Jiang, L., and Tsai, H.L.: 'Improved two-temperature model and its application in ultrashort laser heating of metal films', Journal of heat transfer, 2005, 127, (10), pp. 1167-1173

31 Kanavin, A., Smetanin, I., Isakov, V., Afanasiev, Y.V., Chichkov, B., Wellegehausen, B., Nolte, S., Momma, C., and Tünnermann, A.: 'Heat transport in metals irradiated by ultrashort laser pulses', Physical Review B, 1998, 57, (23), pp. 14698

32 Nedialkov, N.N., Imamova, S., and Atanasov, P.: 'Ablation of metals by ultrashort laser pulses', Journal of Physics D: Applied Physics, 2004, 37, (4), pp. 638

33 Nolte, S., Momma, C., Jacobs, H., Tünnermann, A., Chichkov, B., Wellegehausen, B., and Welling, H.: 'Ablation of metals by ultrashort laser pulses', JOSA B, 1997, 14, (10), pp. 2716-2722

34 Cheng, J., Perrie, W., Sharp, M., Edwardson, S.P., Semaltianos, N.G., Dearden, G., and Watkins, K.G.: 'Single-pulse drilling study on Au, Al and Ti alloy by using a picosecond laser', Applied Physics a-Materials Science & Processing, 2009, 95, (3), pp. 739-746

Chapter 7 - Summary and conclusions

7.1 Summary of this dissertation

In this dissertation, fs laser micromachining is applied to stainless steel, polyurea aerogel, and Mo and ITO thin film for CIGS and CdTe thin film solar cell manufacturing. Femtosecond laser micromachining experiments are conducted and the effects of different laser and system parameters are studied. A predictive single pulse ablation TTM model is conducted to predict the single pulse ablation rate, ablation threshold and ablation crater geometry. The studies presented in this dissertation are shown in Figure 7.1.

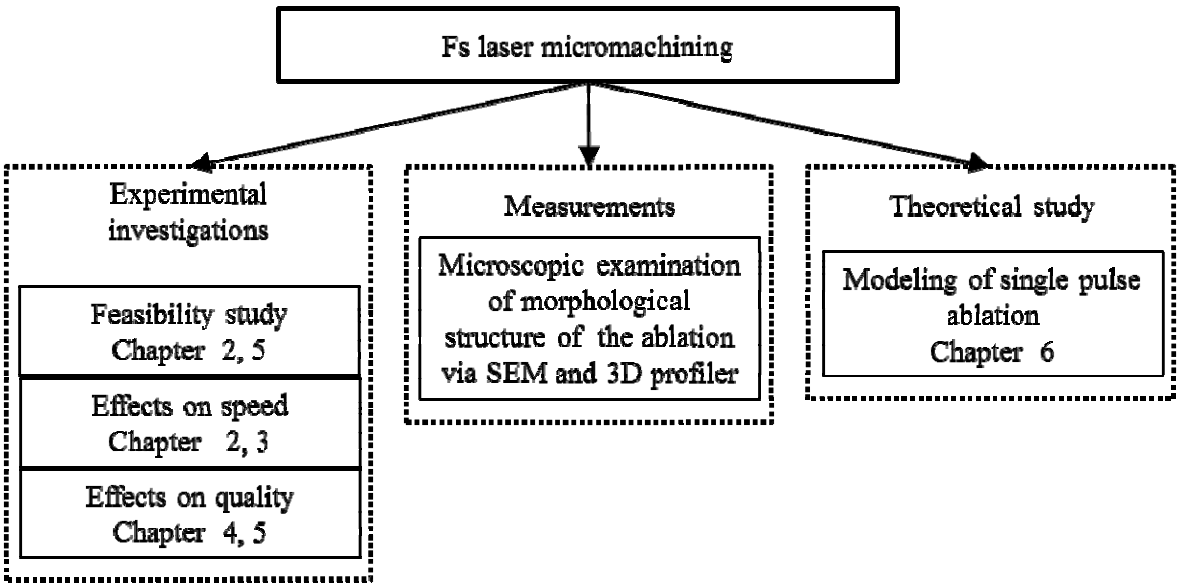

Figure7-1 Achievements of this dissertation

7.2 Conclusions

The conclusions drawn from this dissertation are listed as follows:

- The feasibility of machining polyurea aerogel with fs laser pulse along with the effects of laser parameters on the ablation surface quality was investigated. Experimental results show that the laser scanning speed and laser fluence play an important role in the surface roughness.

- It is feasible to drill high aspect ratio micro-holes using fs laser pulses delivered through a hollow core fiber. The fiber acts as a spatial filter to improve the laser beam profile. The parametric study on the ablation rate indicates that with a given micro-hole size and the sample thickness, a high ablation rate can be obtained with high pulse energy, short pulse duration, and long focal length.
- The feasibility of fs laser scribing of ITO thin film on glass substrate demonstrated that fs laser is an effective tool for producing high quality and high density interconnects in thin film solar cells and thus could significantly increase the solar cell conversion efficiency.
- Scribing Mo thin film on PI was investigated and an optimal feasible region for high speed and high quality interconnect grooves was explored.
- The energy transportation process between electron and lattice is clearly demonstrated. 3D craters ablated by single laser pulses with different laser fluence are simulated, from which the radii and depths of ablation crater can be predicted to guide and design the experiment.
- A good agreement between simulation data with experimental results at low fluence ablation regime was presented. Single pulse ablation threshold and ablation rate for the fs laser ablation of Mo were calculated through the numerical model. The result of the simulation fits quite well with our experimental results at low fluence regime.

7.3 Contributions

The contributions of this research are listed as follows:

1. For the first time fs laser is used to scribe Mo on PI flexible substrate, which is potentially a key process for roll to roll fabrication of GIGS thin film solar cells.

2. Fs laser micro-drilling through a hollow core fiber is studied for the first time, and it offers more flexibility for laser micro hole drilling.

3. The fs laser ablation model provides insights to the physical processes occurring during fs laser excitation of metals. Desired processing fluence and process speed regime can be predicted for Mo thin film by calculating the ablation threshold, ablation rate and ablation crater geometry using the developed model. It also can be applied to fs laser ablation of other metals and semiconductors with minor revision.

4. The research achievements will have positive impacts on future machining processes since fs laser is a comparatively new micromachining technology in thin film solar module fabrication process and aerogel material, and provides a new finishing technology to improve the groove surface roughness without micro cracks and less thermal melting for thin film scribing.

5. Since it is proved in this dissertation that it is feasible to micro-machine and scribe the three types of materials with fs laser, a thorough future research focused on improving the quality will be helpful for its successful implementation in the leading industry segments such as solar energy. This fundamental technology will lead to the development of higher technology-added next generation thin film scribing systems used for photovoltaic devices.

7.4 Future works

Future experimental research should investigate fs laser scribing of P2 and P3 for CdTe and CIGS thin film solar cells. One laser for all three scribes can provide further simplification and flexibility to thin film solar cell production and hence, contributes to cheaper thin film solar cells.

The P2 scribing step requires the removal of double or triple layer of thin films, at a total thickness of a few micrometers from the Mo or ITO surface. An important requirement for the P2 scribe is that the absorber layer should not be melted and the back conductor layer should not be damaged. If the absorbing layer is melted, the melted material forms either a conducting or resistant layer on the conductor layer, which may affect the thin film solar cell efficiency.

The laser spot overlap along a scribe groove needs to be controlled by the translation speed at a constant pulse repetition rate of 1 kHz. Various combinations of laser fluence, beam overlap and pass number should be used for selective ablation of the films. Optimal regimes for laser processing of absorbing layer should be estimated. The beam overlap plays an important role in the processing selectivity because the CIGS and CdTe ablation threshold is sensitive to accumulation of the irradiation dose.

Further improvements should be made in fs laser ablation modeling in the high fluence regime. Future simulation efforts should also investigate the effects of pulse duration and pulse number on ablation threshold, ablation rate and ablation crater shape. Extensive simulations are needed to establish reference process parameters for industrial applications of femtosecond laser patterning for thin film solar cells.

Appendix A - Publications during Ph.D. study

Journal and conference publications

1. **Qiumei Bian**, Shouyuan Chen, Byung-Tai Kim, Nicholas Leventis, Hongbing Lu, Zenghu Chang, Shuting Lei, Micromachining of polyurea aerogel using femtosecond laser pulses, Volume 357, Issue 1, 1 January 2011, Pages 186–193

2. Xinwei Shen, **Qiumei Bian**, Zenghu Chang, Shuting Lei, Benxin Wu, Study on Laser-Fiber Coupling Efficiency and Ablation Rate in Femtosecond Laser Deep Micro-drilling, Accepted by: Int. Journal of Mechatronics and Manufacturing Systems, Vol. 5, No. 3/4, 2012

3. **Qiumei Bian**, Xiaoming Yu, Baozhen Zhao, Zenghu Chang, Shuting Lei, Femtosecond laser ablation of indium tin-oxide narrow grooves for thin film solar cells, Optics & Laser Technology, Available online 10 July 2012

4. **Qiumei Bian**, Xiaoming Yu, Baozhen Zhao, Zenghu Chang, Shuting Lei, Femtosecond Laser Ablation of Al and Mo Thin Film on Flexible Substrate for Fabrication of Thin Film Solar Cells , Published in: 30th International Congress on Applications of Lasers and Electro-Optics, ICALEO 2011, p 869-874, 2011

5. **Qiumei Bian**, Xinwei Shen, Baozhen Zhao, Zenghu Chang, Shuting Lei, Micromachining of Transparent Conductive Oxide (TCO) Film on Glass Substrate Using Femtosecond Laser, Published in: 29th International Congress on Applications of Lasers and Electro-Optics, ICALEO 2010, 1190-1198, 2010

6. **Qiumei Bian**, Shouyuan Chen, Zenghu Chang, Shuting Lei, Femtosecond Laser Pulse Ablation of Polyurea Areogel, Published in: 28th International Congress on Applications of Lasers and Electro-Optics, ICALEO 2009, p 924-930, 2009

7. **Q. Bian**, B.T. Kim, S. Chen, S. Lei, Z. Chang, Deep Microdrilling by Femtosecond Laser Pulses Delivered Through Hollow Core Fiber, Published in: 27th International Congress on Applications of Lasers and Electro-Optics, ICALEO 2009, M406, 2008

Conference presentations

1. **ORAL PRESENTATION "**Femtosecond Laser Pulse Ablation of Polyurea Areogel", 28TH ICALEO ,Nov 2-5, 2009,Orlando,FL USA

2. **ORAL PRESENTATION "**Micromachining of Transparent Conductive Oxide (TCO) Film on Glass Substrate Using Femtosecond Laser**",** 29TH ICALEO ,Sep.26-30,2010,Anaheim,CA, USA

3. **ORAL PRESENTATION** "Femtosecond Laser Ablation of Al and Mo Thin Film on Flexible Substrate for Fabrication of Thin Film Solar Cells", 30TH ICALEO ,October 23-27 2011,Orlando,FL USA

Working papers

1. X. Yu, **Q. Bian**, B. Zhao, Z. Chang, P.B. Corkum, S. Lei, Control of multiphoton and avalanche ionization using a UV-IR pulse train in femtosecond laser machining of fused silica, submitted to Applied Physics Letters

2. **Qiumei Bian**, Xiaoming Yu, Zenghu Chang, Shuting Lei, Predictive 3D model for femtosecond laser ablation of Mo thin film, to be submitted to Journal of Laser Applications